# Bose-Einstein Condensate Experiments in Optical Lattices

by

Rachel Elizabeth Sapiro

A dissertation submitted in partial fulfillment
of the requirements for the degree of
Doctor of Philosophy
(Physics)
in The University of Michigan
2010

Doctoral Committee:

- Professor Georg A. Raithel, Chair
- Professor Paul R. Berman
- Professor Duncan G. Steel
- Assistant Professor Aaron E. Leanhardt
- Assistant Professor Jennifer P. Ogilvie

© RachelElizabethSapiro 2010
All Rights Reserved

This thesis is dedicated to my sister Deborah, because she asked for it to be.

# ACKNOWLEDGEMENTS

I would, first and foremost, like to acknowledge the help and support of my advisor, Professor Georg Raithel. Just about everything I know about atomic physics–and a lot of what I know about machinery, electronics, optics, and many other topics–I learned in his lab, either from Georg or from his students (and a great deal of it directly from him). Georg has always been very willing to teach, answer questions, and generally lend a hand in the lab. I can't even begin to guess how much time he has saved me over the years with his ability to quickly and accurately diagnose nearly any problem with any piece of equipment. This thesis would not have been possible without his guidance.

I would also like to acknowledge my fellow members of the Raithel lab: Sarah Anderson, Jae-Hoon Choi, Cornelius Hempel, Brenton Knuffman, Tara Cubel Liebisch, Rahul Mhaskar, Melinda Morang, Spencer Olson, Eric Paradis, Erik Power, Aaron Reinhard, Andrew Schwarzkopf, Mudessar Shah, Betty Slama, Mallory Traxler, Varun Vaidya, and Kelly Younge for their help, discussions (scientific and otherwise), and for the loan of various pieces of equipment over the years that they may or may not realize that I took. I would especially like to thank those grad students who worked with me directly. Natalya Morrow got me started in the lab with my first construction projects, and designed much of the original BEC apparatus. She made me feel welcome when I was new, and was always willing to talk and laugh with me. David Anderson worked with me for my last year, diligently helping with the day-to-day tasks, and taking on an increasing share of the work of running the experiment as I started to write my thesis. The BEC-ion work undoubtedly went faster because of Dave's help, and I wish him luck in running the project in the future. Most of all, I would like to thank Rui Zhang for his endless patience in teaching me lab skills and running experiments with me. The first few chapters of this thesis were entirely a joint endeavor between me and Rui; we built the original BEC project together, and we ran the optical lattice experiments together.

I would like to acknowledge the staff at the Lurie Nanofabrication Facility for helping me make the electrode chip with the ion-extraction tip. In particular, I would like to thank Katsuo Kurabayashi and Katharine Beach for their help in designing the structure and fabrication process for the chip, and Pilar Herrera-Fierro for guiding me through the process.

I would like to thank my grandmother, Gertrude Schmeidler, for reading and editing my papers, and for all the effort and enthusiasm she put into understanding my work and discussing it with me, even though physics in not even close to her field. I wish she had lived to see me graduate. I would also like to thank my parents for also reading and editing my work, for never giving up on trying to understand it even when I got annoyed when they asked me the same questions every month for several years, and for at least making a show of appreciating all the shiny souvenirs I smuggled out of the lab and took home to them. I know these are all things parents are supposed to do, but I still appreciate it.

I gratefully acknowledge FOCUS (an NSF Frontiers Center) and the AFOSR for funding my work.

# TABLE OF CONTENTS

**CHAPTER**

# LIST OF FIGURES

**Figure**

# LIST OF APPENDICES

**Appendix**

# ABSTRACT

A Bose-Einstein condensate (BEC) is a macroscopic ensemble of atoms that collectively behaves as a single quantum-mechanical object. In this thesis I describe an apparatus built to create and study a BEC, as well as initial experiments carried out using a one-dimensional optical standing wave (optical lattice) to manipulate the BEC. In the first experiment, a weak optical lattice Bragg-reflects a BEC moving in a nearly harmonic trap. The Bragg reflection combined with the harmonic trapping potential cause the BEC to oscillate, much as light oscillates in an optical cavity. In the second experiment, a deep optical lattice applied to an atom cloud for a short duration is used to split and recombine the atomic wavefunction. By doing this we can create two different types of atom interferometer: a small-separation atom interferometer which works with either a BEC or a thermal gas, and a large-separation atom interferometer which works only with a BEC and whose interferometric arms are, in principle, separately addressable. In the third experiment, an optical lattice potential is slowly turned on. Under the influence of this lattice potential, the BEC loses its superfluid properties, but fully regains them when the lattice is turned back off. This behavior is consistent both with a reversible transition to a 1-D Mott insulator state and with mean-field effects in a deep lattice; both interpretations are discussed.

In the latter part of this thesis I describe an apparatus designed to accommodate experiments involving both a BEC and an ion. The interactions between an ion and a BEC have never before been experimentally investigated. Our apparatus includes both the means to localize an ion by actively shielding against stray electric fields and to spatially image ions. This should allow future experiments in which a single ion is embedded in a BEC. In addition to imaging ions, the apparatus provides the capability to create high-resolution images of distributions of neutral atoms by photoionizing them and then quickly imaging them. I conclude the thesis with a discussion of future experiments exploring ion-BEC interactions.

## CHAPTER I

# Introduction

The world of quantum mechanics is nothing like the world we see around us every day. In the quantum regime, the outcome of an event is probabilistic, rather than deterministic. Matter, which behaves like particles in our macroscopic world, and light which behaves like a wave, can both take on properties of both particles and waves in quantum mechanics. However, the quantum regime is far out of reach of our everyday experience. In order to see quantum mechanical behavior, we must typically look at objects which are very small or have very low energy. The first observations of the wave-like properties of matter were made using electrons. Even with the advent of laser cooling, which allowed atoms thousands of times more massive than electrons to be cooled to the point where they were observably in the quantum mechanical regime, observations of quantum mechanics were limited to a single atom at a time; doing an experiment on an ensemble of atoms resulted in a statistical average over many atoms rather than the observation of an ensemble wavefunction. The quantum mechanical objects themselves were still tiny and difficult to isolate, or, when isolated, difficult to observe.

## 1.1 Bose-Einstein Condensation

The creation of an atomic Bose-Einstein condensate (BEC) changed all of this. A BEC is a phase of matter in which a macroscopic ensemble of atoms occupies a single wavefunction. That is, all of the BEC atoms' wavefunctions are in phase with each other, so the atoms behave in perfect synchronization. An atomic BEC can contain anywhere from thousands to millions of atoms. It can span a distance of ten or even a hundred microns, comparable to the width of a human hair, making it visible with conventional optics. If not for the fact that a BEC is incredibly delicate, destroyed by on-resonant light within a few microseconds and invisible to off-resonant light, the largest BECs would be visible to the naked eye. It is truly a macroscopic object, but it still retains the quantum mechanical properties of a single atom.

Bose-Einstein condensation was first predicted by Satyendra Nath Bose and Albert Einstein in 1924. For many decades, however, scientists were only able to make BECs from $^4$He. Helium-4 Bose-Einstein condenses from a liquid rather than a gas, and the atoms interact strongly with each other. Consequently a $^4$He BEC does not behave in accordance with the theory set forth by Bose and Einstein. It was not until 1995 that the first atomic BECs were made from a gas [3, 4]. These atomic BECs are nearly ideal; this is the type of BEC that will be referring to throughout this thesis.

Although BECs present huge advantages for the study of quantum mechanical phenomena, they have one major downfall: BECs are extremely delicate and difficult to produce. In order to create a BEC, atoms must be cooled to the BEC transition. A BEC occurs when atoms of the same species are sufficiently close together that their

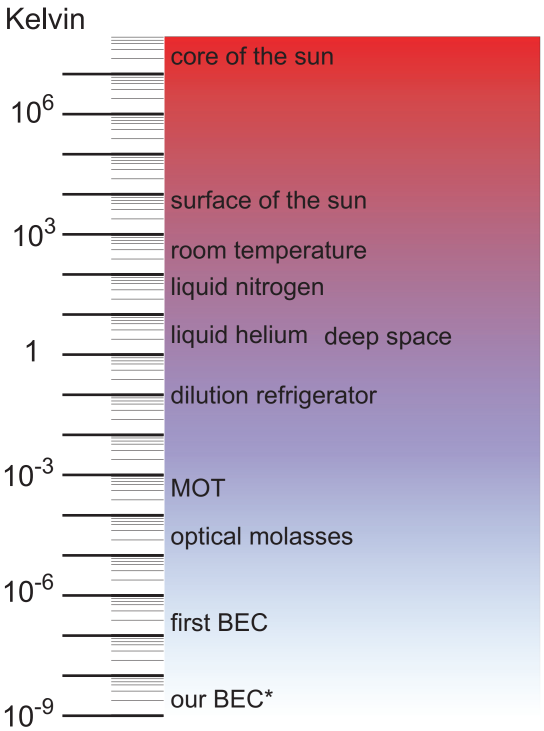

Figure 1.1: A scale of temperatures. *This is our BEC working temperature, not our transition temperature; our BEC is adiabatically expanded after its creation.

freespace wavefunctions overlap with each other. This occurs when the condition

$$n\lambda_{\mathrm{dB}}^3 \geq 2.612 \tag{1.1}$$

is met, where $n$ is the density of the atomic distribution, and $\lambda_{\mathrm{dB}}$ is the de Broglie wavelength of the atoms [5, 6]. The de Broglie wavelength is, in turn, given by

$$\lambda_{\mathrm{dB}} = 2\pi\hbar/(mk_{\mathrm{B}}T)^{1/2} \tag{1.2}$$

where $\hbar = h/2\pi$ ($h$ is Planck's constant), $m$ is the mass of the atom, $k_{\mathrm{B}}$ is the Boltzmann constant, and $T$ is the temperature [7]. Combining these two equations, the transition temperature is then given by

$$T_{\mathrm{c}} = \frac{2\pi\hbar^2 n^{2/3}}{2.612^{2/3} m k_{\mathrm{B}}} \; . \tag{1.3}$$

These equations are exact for a system in free space for an atomic distribution with uniform density. In practice, a BEC is created in a trap and the density is not uniform, so the equations are slightly modified; however, these equations still provide a reasonable order-of-magnitude approximation for the transition temperature. Since $T_c$ is dependent on both density and temperature, one might expect that a BEC could be created either by increasing the density of an ensemble of atoms or by decreasing the temperature. However, most of the atomic species typically used to make a BEC solidify at high pressures well before reaching temperatures necessary to become a BEC [6]; rubidium, which is the element used throughout this thesis, is already a solid at room temperature and atmospheric pressure. A system can only Bose-Einstein condense from a gaseous state (with the exception of $^4$He), so the atoms solidifying prevents Bose-Einstein condensation from occurring. Instead of using gases at atmospheric pressure, then, we use gases too dilute to solidify. A typical BEC has a density of $n = 10^{12}$-$10^{15}$ atoms/cm$^3$ (for comparison, a gas at atmospheric pressure has a density of $10^{19}$ atoms/cm$^3$). This leads to transition temperatures in the 10's-100's of nanoKelvin range. A logarithmic temperature scale is presented in Fig. 1.1 to give a sense of just how cold this is. The coldest known temperature naturally occurring in the universe is $\sim$1 K, and most of deep space is $\sim$3 K. A BEC is typically 10-100,000,000 times colder than that, a similar factor to the difference between the temperature of the core of the sun and that of the coldest places in the natural universe. Reaching, and maintaining, these extreme temperatures requires specialized techniques and equipment. We spent more than 18 months building and improving our apparatus before we were able to realize our first BEC; thus I devote all of Chapter II of this thesis to explaining the methods and equipment we use to create a BEC.

Although all of the atoms in a BEC occupy the same wavefunction, a BEC does not quite behave like a single-atom wavefunction occupied by many atoms. A BEC is a superfluid, so atoms within the BEC move past each other with zero viscosity, suppressing collisions. However, collisions do occur within a BEC. At high densities these collisions can destroy the BEC due to three-body recombination [3]; at low densities these collisions are rare [8], and usually only become relevant when two components of BEC, spatially overlapped but moving in different directions, collide with each other. Although it is possible for two components of the wavefunction of a single atom to be spatially overlapped and moving in different directions, a single atom cannot collide with itself. Another difference between a BEC and a single atom is that a BEC is subject to mean-field effects. While a single atom's wavefunction follows the Schrödinger equation, which is linear, a BEC's wavefunction follows the Gross-Pitaevskii equation, where an extra non-linear mean-field term is added to the Schrödinger equation:

$$i\hbar\frac{\partial\Psi(\mathbf{r},t)}{\partial t} = \left(-\frac{\hbar^2}{2m}\nabla^2 + V(\mathbf{r}) + \frac{4\pi\hbar^2 Na}{m}|\Psi(\mathbf{r},t)|^2\right)\Psi(\mathbf{r},t) \tag{1.4}$$

where $\Psi$ is the wavefunction (also known as the order parameter of the many-body system), $V$ is any external potential (in our case typically a harmonic trapping potential), $N$ is the number of atoms in the BEC, and $a$ is the s-wave scattering length of an atom [9, 10]. This mean-field term is an additional density-dependent potential that a BEC experiences; it typically manifests as an outward pressure on the BEC, and is due to collisions between BEC atoms.

## 1.2 Optical Lattices

The realization of Bose-Einstein condensation has opened many new frontiers in physics research. Among them, one of the most varied and intriguing involves the application of an optical lattice to a BEC. An optical lattice is a periodic light-shift potential composed of a standing wave of light. It is in many ways analogous to a solid-state crystal, and thus can provide some insight into solid-state systems. Because of this, considerable theoretical attention has been given to BECs in optical lattices (for a review, see Ref. [11]). BECs can Bragg-scatter off an optical lattice in much the same way that light can Bragg-scatter off a solid-state crystal [12], and can even undergo Bloch oscillations analogous to the oscillations of electrons in a crystal [13, 14]. An optical lattice can act as a diffraction grating for cold atoms, separating them into multiple orders [15]. These properties allow optical lattices to be used as an effective tool for atom optics.

A consequence of the wave-nature of a BEC is two overlapping BECs will interfere with each other, in much the same way that two laser beams will interfere with each other. A natural application of this, and a promising new technology, is atom interferometry. Light interferometers have existed for over a hundred years, and have been used for numerous purposes, ranging from probing materials (for an early example, see Ref. [16]), to navigation (for reviews see Refs. [17, 18]), to searching for gravitational waves (see Ref. [19] for theory, and Ref. [20] and other LIGO publications for experimental status). Despite their many uses, however, light interferometers are mostly insensitive to electromagnetic and gravitational fields. Atoms, meanwhile, are sensitive to all of these fields; thus, an atom interferometer can provide a far more sensitive probe of force fields [19], in addition to being able to measure nearly anything a light interferometer can measure. Additionally, if the two arms of an atom interferometer are separately addressable, one can measure atom-surface interactions [21], electric polarizability [22, 23], and atom neutrality [24], as well as realize novel nanolithography schemes [25].

In order to build an atom interferometer, however, we must first be able to coherently split, deflect, and recombine atoms' wavefunctions. The easiest way to do this is to apply an optical lattice to a BEC. In Chapter III of this thesis I discuss experiments on deflecting and splitting a BEC, as well as the realizations of two different types of atom interferometer.

### 1.2.1 Mott Insulator

Optical lattices can also be used to mimic solid state systems in a completely different way: through the localization of atoms. In this case the atoms localized in the optical lattice's periodic potential, rather than the optical lattice itself, form a system resembling a solid-state crystal. Unlike a condensed matter system, however, an optical lattice potential contains no defects in its periodicity, and a BEC usually contains no impurities. A particularly interesting localization phenomenon is the phase transition from superfluid to Mott insulator [26]. In the 3-D case, this phase transition occurs when a 3-D optical lattice is adiabatically applied to a BEC. With no lattice applied, the BEC is a superfluid; the atoms can move freely against each other, and have perfect phase coherence. As the lattice depth is increased, at first the BEC is modulated by the lattice potential, but remains a superfluid. At a critical lattice depth, the BEC undergoes a phase transition to a Mott insulator state. In the Mott insulator state, the atoms are number-squeezed, meaning that each lattice well contains a definite, identical number of atoms. This is the ground state of the quantum many-body system in a deep lattice. In the Mott insulator state, tunneling between lattice wells is strongly suppressed. Once the atoms can no longer tunnel between wells, they cannot interact with each other and all phase coherence is lost. Rather than being described by the Gross-Pitaevskii equation, the system follows the Bose-Hubbard model:

$$H = -J \sum_{i,j} \hat{a}_i^\dagger \hat{a}_j + \sum_i V_i \hat{n}_i + \frac{1}{2} U \sum_i \hat{n}_i (\hat{n}_i - 1)\,. \tag{1.5}$$

The first term is the interaction between lattice wells, with tunneling constant $J$ and creation and annihilation operators $\hat{a}_i^\dagger$ and $\hat{a}_i$. The middle term is the effect of the external trapping potential; $\hat{n}_i$ is the number operator corresponding to the number of atoms in the $i$th lattice well. The final term describes on-site interaction between atoms occupying the same well, with on-site interaction constant $U$. The constants $J$ and $U$ are calculated based on the Wannier functions of the system. In the case of a large BEC, which might be denser toward the center and more dilute toward the edges, the Mott insulator state has regions with distinct boundaries; for example, there might be a center region with two atoms per lattice well, surrounded by a shell with one atoms per well [27]. Since the transition from a superfluid to a Mott insulator is a quantum phase transition, it is fully reversible: if the lattice depth is adiabatically decreased, the system returns to a superfluid state.

The Mott insulator transition has drawn the interest of both atomic and condensed matter physicists, due to the possibilities it creates for simulating ideal, controlled condensed matter systems. Under the correct circumstances the transition could be used to create supersolids or other novel phases of matter [28]. Doping the Mott insulator with fermions can be used to simulate a semiconductor [29]. One can use Feshbach resonances to create molecules in a Mott insulator with two atoms per site [30], which could eventually lead to a molecular BEC [31, 32]. The Mott insulator state could also provide a means to entangle neutral atoms and form a quantum register for a quantum computer (for a review, see Ref. [33]). Several laboratories have succeeded in producing the transition from a BEC to a 3-D Mott insulator [26, 29, 30, 34]. Many groups have also tried to explore the Mott-insulator transition in lower dimensions. The Mott insulator transition has been achieved using 2-D [35, 36] and 1-D [37] Bose gases. Some initial work was done by Orzel *et al.* on looking for number squeezing of a 3-D BEC in a 1-D optical lattice [73]. Chapter IV of this thesis deals with our own experiment along these lines, in which we apply a 1-D optical lattice to a 3-D BEC, and observe behavior consistent with a transition to a 1-D Mott insulator.

## 1.3 Ions in a BEC

A mostly unexplored branch of BEC physics is the interaction between a BEC and a small number of impurities. In particular, no controlled experiments have been done with an ion in a BEC. This is especially surprising considering the number of papers addressing the theory of ion-BEC interactions, and the fascinating predictions they make. The presence of ions in a BEC might create a blockade against further ionizations due to Coulombic fields, or due to Fermi statistics [38]. The density of the BEC might be observably increased or reduced in the vicinity of an ion [39]. The electric field due to an ion creates a polarization potential. This potential could attract BEC atoms, forming a molecular bubble of loosely bound neutral atoms around the ion [40]. Another possibility is that the polarization potential might cause the ion to self-trap within the BEC [41–44]. Additionally, there are many predictions about how an impurity affects a BEC in an optical lattice [45, 46]. While Ospelkaus *et al.* have done some preliminary investigations using neutral, fermionic impurities [29], there remain many parameters to explore, and there could be interesting differences between a system with neutral impurities and one with charged impurities.

The major difficulty in ion-BEC experiments is localizing an ion within a BEC. A typical BEC chamber is not built to accommodate an ion; it contains neither the apparatus necessary to trap the ion nor to shield it from stray electric fields. An experiment by Ciampini *et al.*, in which they photoionized a portion of a BEC, yielded no interpretable results because their observations were dominated by the effects of stray fields on the ions [47]. Building a chamber to accommodate both an ion and a BEC is a technical challenge; I spent more than a year and a half redesigning and rebuilding our vacuum chamber for this purpose. Chapter V details our unique new apparatus. The final chapter of this thesis, Chapter VI, describes our current progress toward and future plans for ion-BEC experiments.

# CHAPTER II

# The BEC Apparatus

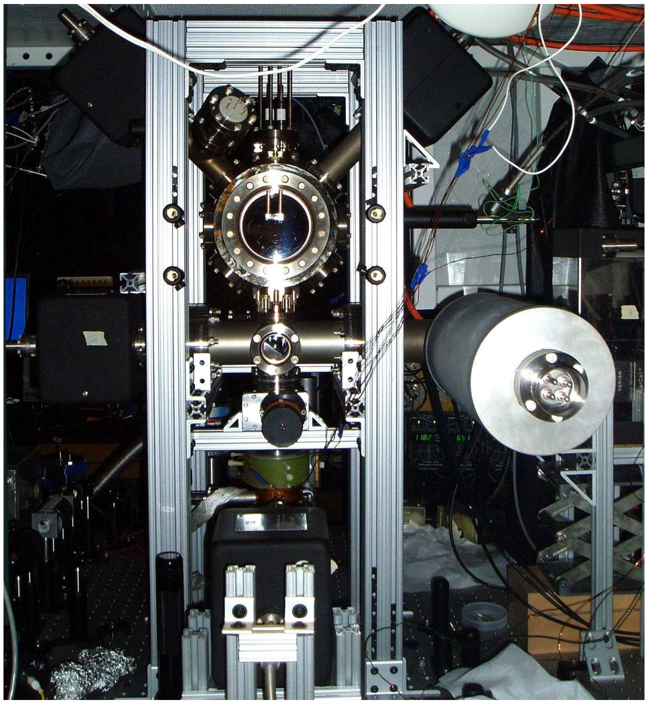

Figure 2.1: The BEC vacuum chamber.

A Bose-Einstein condensate is almost unimaginably cold. A typical temperature for $^{87}$Rb to transition from a gas to a BEC is $\sim$100 nK; for comparison, deep space, the coldest place in nature, is $\sim$3 K, more than ten million times hotter. Achieving the BEC transition temperature is far from trivial (it took us 18 months to build and fine-tune the apparatus before we were able to achieve our first BEC), and requires a long, complicated procedure (in our case lasting at least 15 s), with several cooling steps and multiple types of traps to hold the atoms as we cool them. Furthermore, a BEC is incredibly delicate. This close to absolute zero, any contact a BEC makes with resonant light or with room temperature background gases will quickly heat it to the point of destroying it. In this chapter, I will discuss the BEC apparatus: the equipment and methodology that we use to make a BEC.

## 2.1 Lasers

Lasers are the backbone of any BEC experiment. They're used for everything: cooling the atoms, affecting their internal states, creating potentials to trap or move them, and imaging them.

In our experiments, we primarily use external-cavity diode lasers (ECDLs). These are inexpensive, and allow the level of frequency control necessary for laser cooling. Laser diodes are available in a variety of infrared wavelengths, making them convenient for use in rubidium experiments, since the rubidium transition $5S_{1/2} \rightarrow 5P_{3/2}$ occurs at 780 nm. Although laser diodes have reflective surfaces, creating the internal cavities that allow them to lase, these cavities are small and not easily tuneable. An ECDL cavity is made using the back reflective surface of a laser diode and an external diffraction grating. The grating is angled in such a way that the 1st order reflection couples back into the laser, while the 0th order reflection is coupled out, forming the laser beam. An ECDL with an instantaneous bandwidth of 1-2 MHz can easily be built in-house using standard, inexpensive parts; prefabricated ECDLs from laser manufacturers may have bandwidths of 100 kHz or less. Our experiments use a mix of home-built and purchased lasers. Since the linewidth of $^{87}$Rb is $\Gamma = 2\pi \times 6$ MHz, a laser bandwidth of 2 MHz is sufficiently narrow for a laser to couple efficiently between atomic energy levels. Additionally, the frequency of an ECDL can be scanned, typically over a range of a few gigahertz, by changing the angle of the diffraction grating.

We determine the exact frequency to which to set the laser using saturation spectroscopy. Saturation spectroscopy is performed by shining two weak laser beams through a glass cell filled with room temperature rubidium, with a third (saturation) beam counter-propagating with one of the two beams. All of these beams are split off from the main laser beam. Each of the two weak beams is measured by a photodiode. If the laser frequency is scanned, the absorption spectrum observed from either of the weak beams is Doppler broadened to the point where many of the hyperfine transitions are washed out. The saturation beam, meanwhile, causes atoms to transition from the lower state to the upper state in much the same way as the two weak beams; however, it is strong enough to significantly deplete the lower state. Due to the Doppler shift, the beam counter-propagating with the saturation beam is only on-resonant at the same point in the frequency sweep as the saturation beam for atoms with zero velocity. Since the saturation beam depletes the lower state, however, the beam counter-propagating with it is not absorbed by zero-velocity atoms. The result is that the absorption spectrum observed for this beam is a Doppler-broadened spectrum with a zero-velocity spectrum subtracted from it. This spectrum can be electronically subtracted from the normal Doppler-broadened spectrum of the other weak beam, resulting in a signal corresponding to only the zero-velocity spectrum of the rubidium, with a linewidth not significantly wider than the natural linewidth of the rubidium transitions [48]. Once we have a signal corresponding to a zero-velocity spectrum, we can "lock" the laser frequency to a given point on that signal using an electronic lock (such as a PID or a fast integrator).

Such a lock can keep a laser consistently on-resonance with an atomic transition (or near-resonance, or wherever we want it), limited only by the laser bandwidth, for anywhere from minutes to hours depending on how well constructed the laser and the electronics are.

To reach parts of the spectrum lacking features that can easily be locked to, we lock the laser to a convenient feature, and then send the rest of the beam through an acousto-optic modulator (AOM) that can shift the beam's frequency by 40-100 MHz. The features of the $^{87}$Rb spectrum are sufficiently far apart that we typically send a beam through an AOM twice. An AOM has an added effect in that it deflects light by an angle; this angle increases for larger frequency shifts. Every laser in this experiment is coupled into an optical fiber (occasionally two lasers are coupled into one fiber), both to clean up its spatial mode and to allow the beam to travel across the optics table without getting in the way of other optics. Since the light passing through the AOM is deflected when the AOM is turned on, the undeflected light when the AOM is off follows a different path and is not coupled into the fiber. Thus, an AOM can act as a fast switch. However, in some cases the minuscule amount of light that makes it through the fiber when the laser is undeflected can still be enough to affect our system; thus, we must also have a mechanical shutter before each fiber to ensure that all light is blocked in those cases where any light leakage can be a problem.

Most ECDLs output 10-50 mW. There are some applications, however, that can benefit considerably from having more power. While some companies offer lasers with outputs of up to 1 W, these tend to be prohibitively expensive. A considerably less expensive solution is to build an amplifier; I built two amplifiers for this experiment. We use a tapered amplifier (TA) chip, which is a long trapezoidal diode consisting of just an antireflection-coated gain medium that does not form a cavity. When a current is applied to the TA, light is emitted from both ends, with more light coming from the wider side. The currents used tend to be large, at least 1 A, so it is necessary to actively cool the TA by attaching it to a water-cooled heat sink. When light from a "master" laser (a laser whose frequency is directly controlled) is coupled through the TA, such that it enters the diode on the narrow side and propagates through, it is amplified without any significant change to or broadening of the frequency of the light. It is possible for the TA to amplify two wavelengths at once [49]; in our experiment we routinely use a TA to simultaneously amplify two different master lasers locked to frequencies 6.8 GHz apart. With sufficient seed light from a master laser and sufficient current applied to the TA, up to 1 W can be emitted from the TA. This is enough power that if the laser is focused it can burn through a piece of paper (to the delight of children touring the lab). Thus, safety precautions must be observed: one must be careful not to put one's head at the level of the laser table or shine a beam upwards without something to block it, and no equipment may be placed at the focus of the beam (particularly not optics with delicate coatings, or dark objects, such as neutral density filters or anything painted black).

## 2.2 Vacuum Considerations

A BEC is incredibly delicate, and requires ultra-high vacuum (UHV), with pressures of $10^{-10}$ Torr or lower. Reaching this level of vacuum requires a carefully designed vacuum chamber and arduous processes to clean and pump it. In our system, the vacuum in the BEC chamber is $< 2 \times 10^{-11}$ Torr. We use a Bayard-Alpert gauge that does not read lower than $2 \times 10^{-11}$ Torr; when we run the experiment, the gauge has typically bottomed out, so we assume that we are somewhere in the

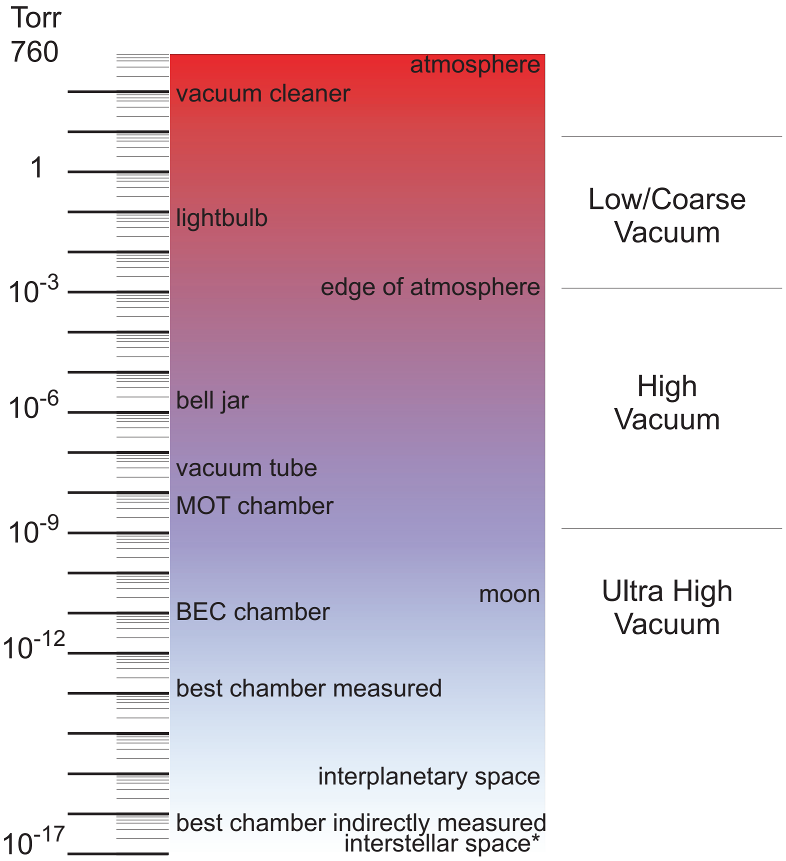

Figure 2.2: A scale of vacuum levels, with manmade vacuum systems on the left and natural vacuum on the right [1]. *Intergalactic space is well beyond the range of the scale.

upper $10^{-12}$ Torr range.

In order to achieve this level of vacuum, several pumps, of several different types, are needed, as can be seen by the complexity of Fig. 2.3. Starting from atmospheric pressure, a roughing pump (temporarily attached, and outside the scope of Fig. 2.3) pumps the chamber down to rough vacuum, around $10^{-2}$ Torr. The roughing pump is set up so that is attached to and pumps through a turbopump (Fig. 2.3 (a)). Once the system is under rough vacuum, it is safe to turn the turbopump on. If it were to be turned on under atmosphere it would not spin up to normal operating speed due to excessive friction; if it were operating at speed and exposed to air the huge number of air molecules rushing through the turbine would wear down the

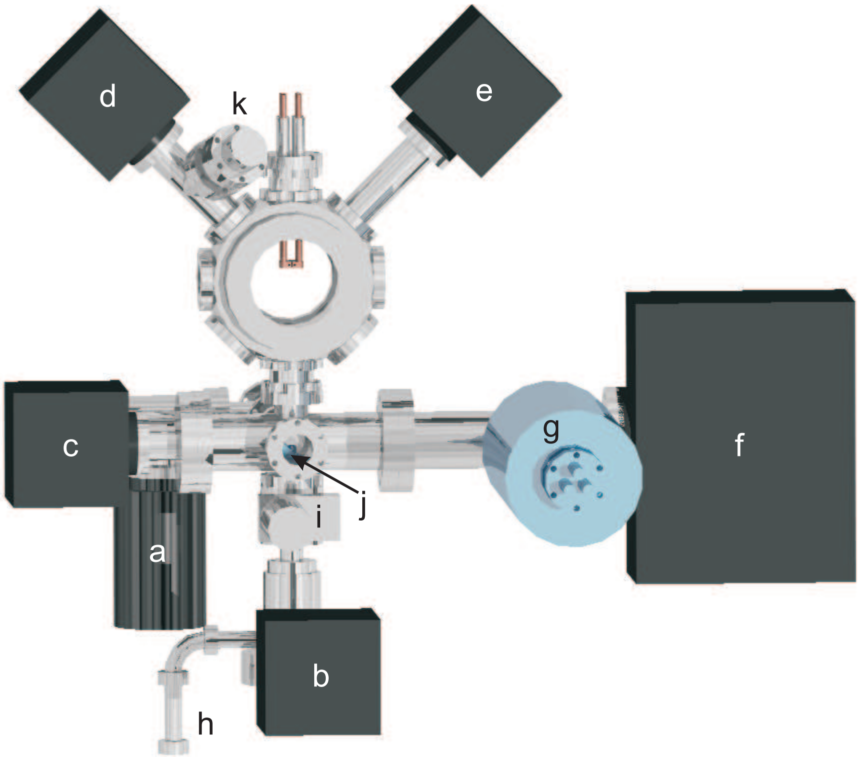

Figure 2.3: BEC chamber with vacuum pumps. (a) Turbopump, connected to a roughing pump on the bottom, and to the chamber on the top via a UHV valve; (b)-(e) ion pumps, 20 L/s; (f) ion pump, 55 L/s; (g) titanium sublimation pump inside a special vacuum nipple corrugated for extra surface area; (h) rubidium source; (i) gate valve; (j) dividing tube to separate the intermediate chamber pumped by (c) from the top chamber pumped by (d)-(g), with a hole to allow the atomic beam to pass from the bottom chamber to the top chamber; (k) vacuum gauge.

blades, breaking the pump. In theory, the turbopump should be capable of pumping down to well into the $10^{-9}$ Torr range, or even slightly lower, but on our system we use a small turbopump which can only barely handle the volume of our chamber. Furthermore, since the turbopump has moving parts, the vibrations from running the pump could disrupt the lasers, so it must be turned off (and typically detached) when the experiment is running. Thus, it is necessary to have other pumps for the UHV range.

We use two types of pumps to achieve and maintain UHV. The first is the ion pump (Fig. 2.3 (b)-(f)), and the second is the titanium sublimation pump (Fig. 2.3 (g)). Both types of pumps are passive, and so create no vibrations. An ion pump can be turned on when the vacuum reaches $10^{-4}$ Torr without risking damage to the pump and can pump down to $10^{-11}$ Torr or better. A titanium pump does not become effective until the vacuum has already reached about $10^{-9}$ Torr, but its pumping speed is an order magnitude of larger than that of an ion pump. It is necessary to use both types of pumps because they are each most effective on different types of gases.

In addition to a wide array of pumps, careful preparations must be made to reach UHV. All materials in the vacuum chamber must be carefully chosen based on their outgassing properties. Hydrocarbons are strictly forbidden unless they have been extensively tested, and even some metals, such as lead or brass, cannot be used. Furthermore, since rubidium is very reactive, we must consider whether any of the materials will react with rubidium to create byproducts that will outgas and ruin the vacuum. After the chamber is assembled and pumped down for a couple of days, it is necessary to bake the whole chamber to temperatures above 200° C for about a week to speed the pumping out of any residual water, hydrocarbons, and adsorbed gases.

One final consideration must be made in the design of the chamber. Near the rubidium source (Fig. 2.3 (h)), the pressure may be higher than $10^{-8}$ Torr due solely to rubidium vapor. In fact, we want it to be this high for a vapor-cell MOT (explained below), which is the first step toward making a BEC. However, where the BEC itself is made, we need pressures three orders of magnitude lower. Thus, we divide the chamber into a lower section and an upper section, with a gate valve (Fig. 2.3 (i)) between them so that we can open and close them separately if we need to break vacuum for any reason. Even with the gate valve open, as it must be for normal operation, the lower and upper chambers are only connected by small apertures.

At the top of the lower chamber, there is one such aperture, a few millimeters in diameter; the lower chamber has only one pump attached to it so that high rubidium pressures can be maintained. There is a second aperture, with a diameter of 1 cm, a few inches above the gate valve, with a dividing tube (Fig. 2.3 (j)) to direct any residual gas to the side rather than up; the "intermediate" chamber between these two apertures, formed by the dividing tube, has its own ion pump (Fig. 2.3 (c)) in order to help maintain differential pressure between the lower and upper chambers. It is not clear that having this intermediate chamber is necessary, but we originally had so much difficulty reaching $10^{-11}$ Torr in the upper chamber that we tried many modifications of the chamber to try to achieve this level of vacuum. Since these modifications all helped in the aggregate, and the dividing tube cannot be easily added or removed without ruining the vacuum, we cannot test its effect individually.

## 2.3 The choice of $^{87}$Rb

So far I have taken for granted that the atomic species used throughout this thesis is $^{87}$Rb. In fact, very few atoms can be Bose-Einstein condensed, so the atomic species must be carefully chosen. There are three requirements. The first requirement is that the atom must be a boson; otherwise it will not follow the Bose statistics that allow a group of atoms to all occupy the same energy level. This rules out all atoms with half-integer total spin. The second requirement is that the atomic species can be easily laser cooled. Alkali and alkaline earth elements are the easiest to laser cool; rubidium is a particularly good choice because of the availability of inexpensive lasers at the rubidium laser cooling transition. The third requirement is that the atom must have a positive s-wave scattering length, such that collisions between atoms tend to be elastic. This is necessary for evaporative cooling, which will be described later in this chapter, as well as to maintain the stability of a BEC once it is formed. This last requirement rules out the more abundant rubidium isotope, $^{85}$Rb, leaving $^{87}$Rb as the atomic species of choice.

## 2.4 How the BEC is Made

There currently exists no single technology to cool a sample of alkali atoms all the way from room temperature to the BEC transition temperature. Instead, it must be done in stages: our sample of $^{87}$Rb can be laser-cooled from room temperature to below 1 mK and then evaporatively cooled the rest of the way to the transition temperature. The initial laser cooling is done using a magneto-optical trap (MOT). A MOT consists of three pairs of counter-propagating laser beams, one pair for each spatial dimension, and a quadrupole magnetic field centered where the six beams meet, as shown in Fig. 2.4 (a).

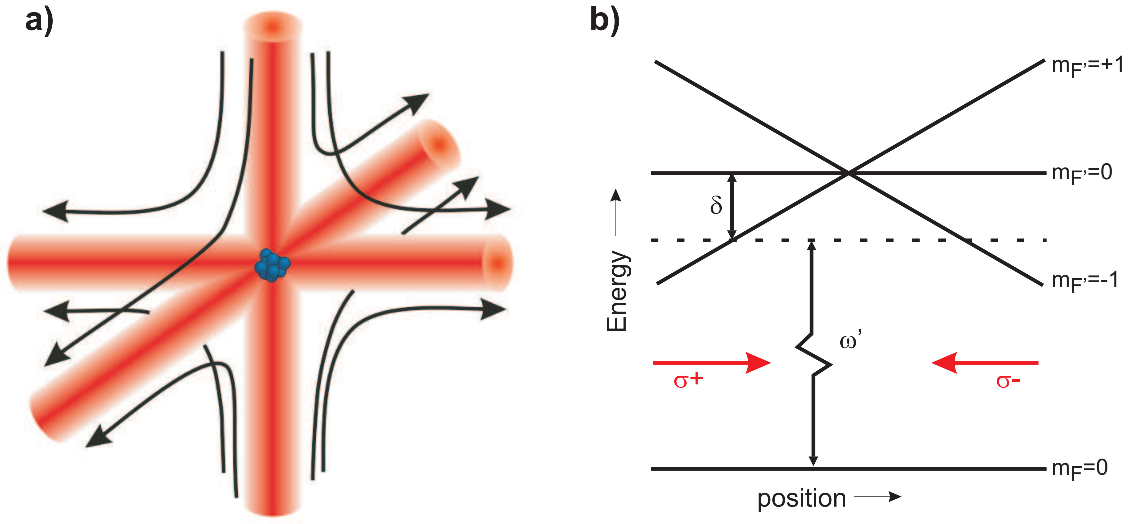

Figure 2.4: (a) MOT laser beams and magnetic fields. (b) A schematic of a two-level MOT transition: a lower level with one magnetic sublevel, and an upper level with three magnetic sublevels, with a background magnetic field with a constant (non-zero) gradient. The lower and upper levels are coupled by a laser with frequency $\omega'$, with a detuning $\delta$ from resonance.

The cooling works through radiation pressure. Consider a two-level system, with an energy between the levels $E = \hbar\omega$ (for the rest of this thesis, when talking about the energy of an atomic transition, I will switch freely between referring to actual energies, $E$, angular frequencies, $\omega$, and regular frequencies, $\nu$, where $\nu = 2\pi\omega$). An atom moving in a direction, say the $+x$ direction, absorbs light from the on-resonant laser beam (that is, a laser beam with wavelength $\lambda = 2\pi c/\omega$) pointing in the $-x$ direction. The atom thus gains a recoil momentum, $p_{\mathrm{r}} = h/\lambda$, in the $-x$ direction, slowing it down. It then re-emits the light in a random direction. In general, then, the atom is pushed in the $-x$ direction. With a second, counter-propagating beam in the $+x$ direction, the atom is pushed to nearly a halt in $x$: to the Doppler limit, corresponding to a temperature of 140 $\mu$K for $^{87}$Rb atoms. To prevent an atom moving in the $-x$ direction from absorbing too much light from the beam propagating in the $-x$ direction, and so being accidentally accelerated, the laser beams must be tuned to a frequency $\omega'$ that is slightly lower than resonance (red-detuned). This way, an atom moving toward the beam sees it blue-shifted closer to resonance and is more likely to absorb light from it and decelerate, while an atom moving away from the beam sees it red-shifted away from resonance and is less likely to absorb light from it and accelerate. This cooling process can be generalized to all three spatial dimensions, and is called an optical molasses. However, there is nothing to keep the atoms from (slowly) diffusing out of range of the laser beams, which are themselves typically only about 2 cm in diameter. Therefore, a magnetic quadrupole field is added, with field lines as shown in Fig. 2.4 (a).

The effect of the magnetic quadrupole field is shown in Fig. 2.4 (b). Again, we simplify by just looking at the x-direction and looking at the center of the magnetic field, where the gradient is approximately linear. We also, for the sake of argument, simplify our level diagram to one consisting of a lower level with a single state,

$m_F = 0$, and an upper level with three magnetic sublevels, $m_{F'} = 0, \pm 1$. (Our real-life system, with $^{87}$Rb, uses a transition from $|5S_{1/2}, F = 2 > \rightarrow |5P_{3/2}, F' = 3 >$, with five and seven magnetic sublevels respectively; see the level diagram in Fig. 2.5.) Due to the Zeeman shift, the $m_{F'} = \pm 1$ magnetic sublevels see potentials that slope in proportion to the magnitude of the magnetic field. In this case the laser beams, in addition to being slightly red-detuned (by a frequency $\delta$), are also circularly polarized. The two counter-propagating beams are polarized the same way with respect to their respective propagation directions, either both right-handed or both left-handed, but in the reference frame of an atom this corresponds to opposite polarizations. An atom moving in the $-x$ direction will encounter a $\sigma+$ -polarized beam and, when it absorbs the light, will undergo the transition $|F, m_F > \rightarrow \ |F', m_{F'} = m_F + 1 >$. This beam gives the atom a momentum kick back toward the center of the trap. Likewise, when the atom is moving in the $+x$ direction, it will absorb from the $\sigma-$ -polarized beam. These magnetic potentials are small enough to have little effect as a magnetic trap; a MOT traps through radiation pressure [5]. As stated above, a quadrupole field is used to create this sort of linear gradient in three dimensions. As can be seen in Fig. 2.4 (a), on one axis, the "strong" axis, the magnetic field points toward the center, and on the other two axes, the "weak" axes, the magnetic field points away from the center. This means that the laser beams pointing along the strong axis must be polarized oppositely from those pointing along the weak axes. (The magnetic field can just as easily have the strong axis pointing away from the center and the weak axes pointing toward the center; in this case, the polarizations of all of the laser beams would be set opposite to the case where the strong axis points toward the center.)

In the real world, $^{87}$Rb is not quite a two-level system, although it comes closer

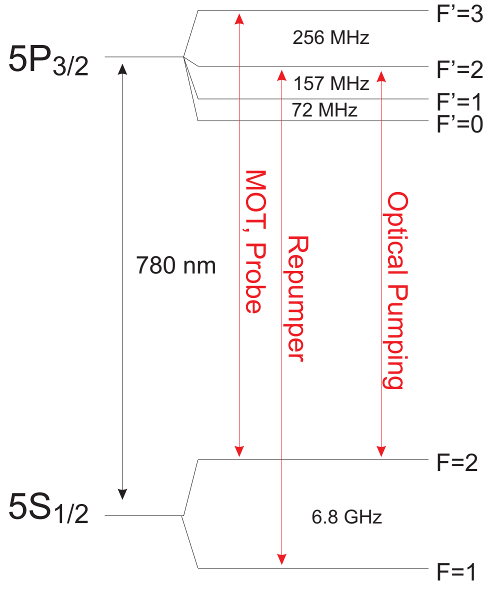

Figure 2.5: Level diagram of the fine and hyperfine splitting of the ground state of $^{87}$Rb [2]. Transitions used in the experiment are marked with arrows and labels in red.

than most atoms do. As can be seen in Fig. 2.5, the transition from $|5S_{1/2}, F = 2 > \rightarrow |5P_{3/2}, F' = 3 >$ is a closed transition: according to selection rules, an atom in the state $|5P_{3/2}, F' = 3 >$ can only spontaneously decay to $|5S_{1/2}, F = 2 >$. This makes it a good choice to use as the laser-cooling transition. However, the $|5P_{3/2}, F' = 3 >$ and $|5P_{3/2}, F' = 2 >$ states are only 256 MHz apart [2]. This means that there is some probability that an atom exposed to the light-field from a MOT laser beam tuned to $|5S_{1/2}, F = 2 > \rightarrow |5P_{3/2}, F' = 3 >$ will undergo the off-resonance transition $|5S_{1/2}, F = 2 > \rightarrow |5P_{3/2}, F' = 2 >$. From $|5P_{3/2}, F' = 2 >$, it can spontaneously decay back down to $|5S_{1/2}, F = 2 >$, or to $|5S_{1/2}, F = 1 >$. Although the probability of this occurring is very small, it happens at a rate of a few times per millisecond (assuming a reasonable MOT beam intensity); since MOT lasers are typically applied for several seconds, chances are that all the atoms in the MOT will at some point undergo this off-resonance transition. The hyperfine level $|5S_{1/2}, F = 1 >$ is 6.8 GHz from the nearest state, so the probability of an atom exposed to the MOT light transitioning out of that state is practically zero: it is a “dark” state. An atom in the dark state does not interact with the MOT light and cannot be cooled. Thus, it is necessary to have another laser to pump any atoms that fall into the dark state back into a state where they can interact with the MOT light. This laser is called a “repumper” and is tuned to the $|5S_{1/2}, F = 1 > \rightarrow |5P_{3/2}, F' = 2 >$ transition. The propagation direction and polarization of the repumper do not matter; repumper light just has to make it to the atoms somehow. In our experiments, we find it easiest to co-propagate the repumper light with the MOT light.

### 2.4.1 Pyramidal MOT

As discussed in the section on the vacuum system, it is necessary to make the BEC far from the source of room-temperature rubidium. Thus, we use a double-MOT setup: we make a primary MOT near the rubidium source, which pre-cools atoms and then sends them as a cold atomic beam to a secondary MOT in the part of the vacuum chamber where we intend to make the BEC.

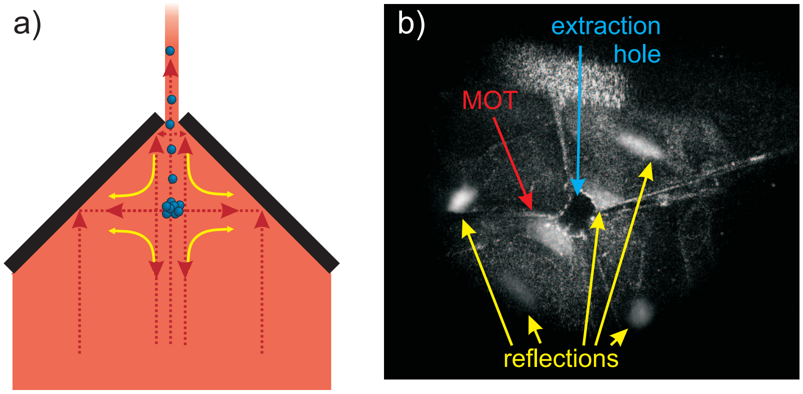

Figure 2.6: a) Schematic of a pyramidal MOT. Red dotted arrows are directions of light beams; yellow arrows represent magnetic field lines. The red background represents the full area illuminated by the laser beam. b) Fluorescence image of the pyramidal MOT and its reflections off the pyramidal mirror.

The primary MOT configuration we use is a type of vapor-cell MOT called a pyramidal MOT [50]. A mirror shaped like the inside of a right pyramid is hung in the primary vacuum chamber, with the apex pointing up. The pyramid is near an ampule of rubidium, which is heated slightly to flood the primary chamber with rubidium vapor. (The ampule contains both the more abundant $^{85}$Rb and the more useful $^{87}$Rb, but the $^{85}$Rb transitions are a few gigahertz from the $^{87}$Rb transitions. The $^{85}$Rb does not interact with the laser light and just adds to the background vacuum pressure.) A large MOT beam, $\sim$2 inches in diameter, with a power upwards of 200 mW, is directed straight up into the pyramid. Light bounces off the 45° internal mirrors in all directions, as shown in Fig. 2.6 (a), creating the six MOT beams. With each bounce off a mirror, the polarization of the beam flips. For example, if the original laser beam, shining upwards, is $\sigma+$ polarized, then when the light has bounced once and is propagating in any horizontal direction, it is $\sigma-$ polarized. When it has bounced twice and so is propagating downwards, it is again $\sigma+$ polarized. Thus, the two horizontal axes are oppositely polarized from the vertical axis, so the vertical axis must be chosen as the strong axis of the MOT. The MOT magnetic fields are created by a pair of coils wrapped around the outside of the chamber in an anti-Helmholtz configuration (that is, current flows through the coils in opposite directions with respect to each other), with their axis centered along the center of the pyramid and the laser beam and the mid-point between the coils at the height where the MOT should be (typically about 1 cm below the apex of the pyramid). A fluorescence image of the pyramidal MOT, showing light scattered off the atoms (as well as any imperfections in the pyramidal mirror), can be seen in Fig. 2.6 (b).

The apex of the pyramid has a $\sim$1.5 mm hole. Since no light is reflected down from the hole, atoms directly under the hole experience radiation pressure upwards but not downwards. This differential radiation pressure pushes these already-cold atoms out of the pyramid and sends them flying up to the top part of the chamber with a velocity of ∼10-15 m/s.

### 2.4.2 Laser Cooling in the Secondary Chamber

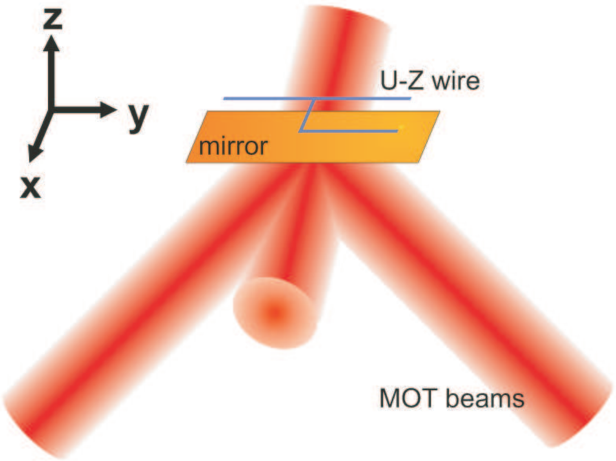

Figure 2.7: The mirror-MOT setup in the secondary chamber.

When the pre-cooled atoms reach the upper, secondary chamber, they are caught in a secondary MOT and re-cooled. The secondary MOT is configured as a mirror-MOT: the MOT light reflects off of a 1-inch square mirror hanging inside the vacuum chamber. The configuration of the secondary MOT is shown in Fig. 2.7. The axis labels in this figure indicate the axes that will be used for the rest of this thesis. As can be seen in the figure, there is a horizontal beam, which is retro-reflected, forming the two MOT beams on the $x$-axis. The other four MOT beams come from two diagonal beams on the $y$-$z$ plane, which bounce off the mirror and counter-propagate into each other. Each beam must be carefully matched in intensity so that radiation pressure does not blow away the MOT. Typically, each beam has a power of ∼20 mW and a diameter of a little less than an inch; however, due to space considerations the horizontal beam is slightly smaller than the diagonal beams. The strong axis of the MOT is along one of the diagonals (the reason the MOT is set up this way will be explained below). In addition, there is a pair of Helmholtz coils wrapped around the chamber on each axis to create bias and compensation magnetic fields in order to move the MOT center and cancel out stray magnetic fields (such as the Earth's magnetic field or magnetized screwdrivers that have been misplaced too close to the vacuum chamber).

There are two ways to generate the magnetic fields for the MOT in the secondary chamber: with a pair of coils wrapped around the outside of the chamber in an anti-Helmholtz configuration or with a combination of current-carrying wires above the in-vacuum mirror and external bias coils, as in Refs. [51, 52]. We call these two configurations the "external MOT" and "U-MOT," respectively.

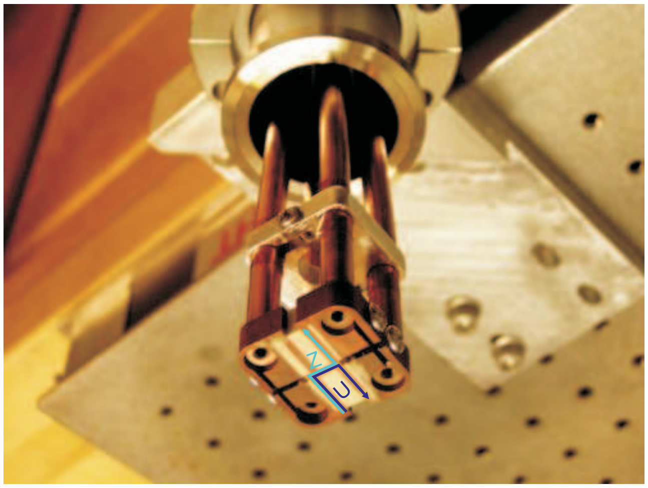

Figure 2.8: U and Z wires for the BEC magnetic traps.

The current-carrying wires used to make the U-MOT consist of a 1 inch copper block machined into an H-shape and attached to four hollow copper feedthroughs; a photograph of the feedthrough and the block, henceforth called the "U-Z wire," can be seen in Fig. 2.8. As indicated in the figure, current can flow in either a U-shaped or a Z-shaped configuration. The feedthroughs have copper caps silver-soldered to their ends. On the inside, they have brass tubes. Chilled water from a heat exchanger flows in through the brass tubes and back out through the space between the brass tubes and the inner wall of the feedthroughs. In this way, the entire feedthrough is water-cooled, and thus the heat load from large currents through the narrow U-Z wire can be dissipated. The current-carrying parts of the U-Z wire itself have a square cross-section and are 1.5 mm on a side. Typical currents are 50-55 A.

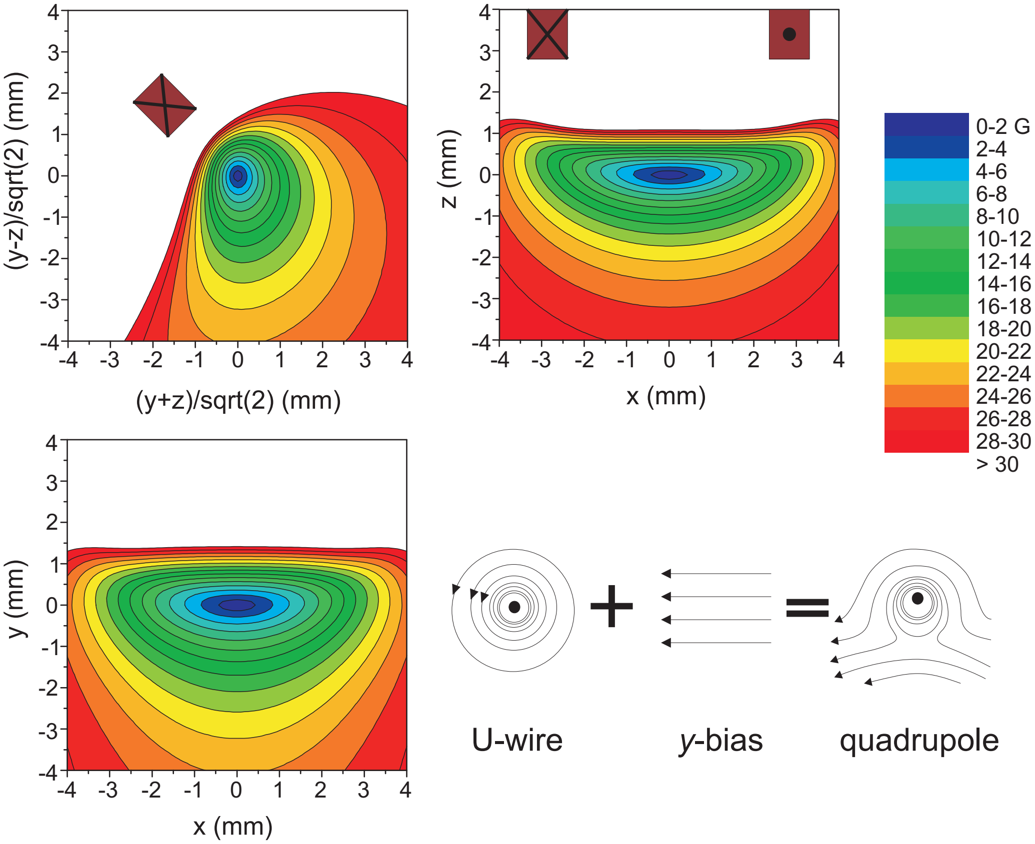

Figure 2.9: Top left and right, bottom left: plots of the magnetic fields of the U-MOT with 50 A of current on the U-wire. The origin is defined to be the center of the MOT. The wires are drawn in brown on the plots for reference, with current direction indicated. Bottom right: schematic of the magnetic field lines of the U-MOT in the $y$-$z$ plane.

As stated above, the superposition of the magnetic field from the U-wire and an external bias field creates a magnetic field with the topology of a quadrupole. The magnitude of this total magnetic field is plotted in Fig. 2.9, for the case of a 50 A current flowing through the U-wire. The wires themselves are drawn in brown on the plots for reference, along with current directions. As can be seen, the magnetic field has a zero below the wire. While the gradient is not ideally linear, it is close enough, since a MOT is fairly robust and does not require perfect conditions. To understand why this setup creates a quadrupole-type field, first we consider only the center bar of the U-wire. According to the Biot-Savart law, when current flows along the center bar, the resultant magnetic field lines form circles in the $y$-$z$ plane. The superposition of this magnetic field and a constant bias magnetic field in the $y$-direction (as from our Helmholtz coils) would have a zero at some point either above or below the wire (depending on the direction of the bias; in our case we choose the bias such that the zero is below the wire), creating a 2-D quadrupole in the $y$-$z$ plane. This is illustrated schematically on the bottom right corner of Fig. 2.9. Note that the axes of the quadrupole are rotated 45° from the axes defined in Fig. 2.7 (although they appear somewhat flattened in the diagram). These rotated axes are why the mirror-MOT, with its diagonal laser beams, is necessary. The magnetic fields in the $x$-direction come from the legs of the U-wire: again, based on the Biot-Savart law, the magnetic field lines form circles, this time in the $x$-$z$ plane. However, directly below the center of the U-wire, the magnetic field is primarily in the $x$-direction, and the $x$ components of the magnetic fields from the two legs cancel each other. A small $z$-bias can be applied to cancel any residual $z$ component of the magnetic fields from the legs. Thus, the total magnetic field from the whole U-wire, plus a constant magnetic field in the $y$- and $z$-directions, results in a 3-D quadrupole trap.

Figure 2.9 shows a very strong magnetic field gradient; near the center of the trap, it is 50 G/cm on the weakest axis. Due to the strength of the trap, the useful capture volume, where atoms wandering in can be picked up by the MOT, is only a few millimeters. Although the capture volume can be improved slightly by decreasing the amount of current in the U-wire (at first glance, 50 A may seem a bit excessive), the U-MOT on its own will never be very large. Therefore, we initially trap the atoms from the cold atomic beam in an external MOT. The MOT coils external to the chamber are very large and in a near-ideal anti-Helmholtz configuration, allowing for a nearly ideal MOT. They are wrapped on the chamber at 45° with respect to the axes of the chamber, to match the U-MOT, so that the same laser beams can be used for both. To maximize the size of the external MOT, we use a relatively small gradient, ∼12 G/cm. The external MOT is quite large: after 10 s of loading it has $> 10^8$ atoms, is at least 4 mm across, and is easily visible to the naked eye (despite the scattered light being at 780 nm, which is technically in the near-infrared and thus difficult for the eye to detect). A picture of the external MOT can be seen in Fig. 2.10. (This picture, along with all other pictures of atom distributions in this thesis not otherwise indicated, was taken using shadow imaging, which will be explained near the end of this chapter.)

In the last cooling step for making a BEC, the atoms are in a "Z-trap" (which will be described below), which is much smaller than the external MOT. However, since the Z-trap magnetic fields come from the U-Z wire, it is easy to match the size and gradient of the Z-trap with the magnetic fields of the U-MOT. The better the match is between the MOT and the Z-trap, the more efficiently atoms can be transferred between them. Thus, although we initially catch the atoms in the external MOT, after 10 s of capture time we compress them into the U-MOT, trying to cram as many atoms into the U-MOT's small volume as possible. The U-MOT cannot hold all of the atoms, though, and after 100 ms shows significant losses, eventually decaying to the same steady-state it would achieve if we loaded directly into the U-MOT in the first place. To prevent this, we hold the atoms in the U-MOT for only 70 ms. A picture of the U-MOT, loaded directly from the external MOT and held for 70 ms, is shown in Fig. 2.10. Although the U-MOT has 80% as many atoms as the external MOT (the transfer between the MOTs is not quite perfect), the U-MOT appears several times smaller than the external MOT in the picture, due to compression.

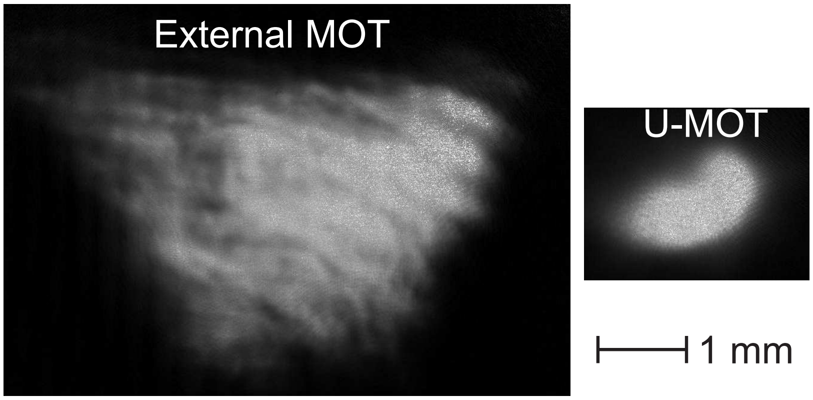

Figure 2.10: The external MOT and the U-MOT. The external MOT is much bigger and less dense than the U-MOT; the U-MOT, despite its diminutive size, contains 80% as many atoms as the external MOT.

The temperature of the MOT is, at best, $\gtrsim 100\mu$K. When the atoms are transferred into the U-MOT, they almost certainly undergo heating due to the compression and may be well above 1 mK. The hotter the atoms are, the less efficiently they can be transferred into the Z-trap; if they are hot enough, they might not even be trapped at all. To ease this last transition, then, we do one last cooling step with the laser light. We turn off all of the MOT magnetic fields, switching our bias coils so that they compensate for all magnetic fields and creating a region of zero magnetic field; we must turn the light off while the coils are switching. We then turn the MOT beams back on, creating a 3-D corkscrew optical molasses, which re-cools the atoms. To improve the cooling, the beams are detuned to several linewidths from resonance (which, because of decreased deflection from the AOM, causes less light to be coupled through the fiber and thus to reach the atoms during the molasses stage).

The molasses cooling lasts for 3.5 ms, so as not to give the atoms enough time to move away from the trapping region. After this, the MOT beams are permanently turned off.

### 2.4.3 Z-trap

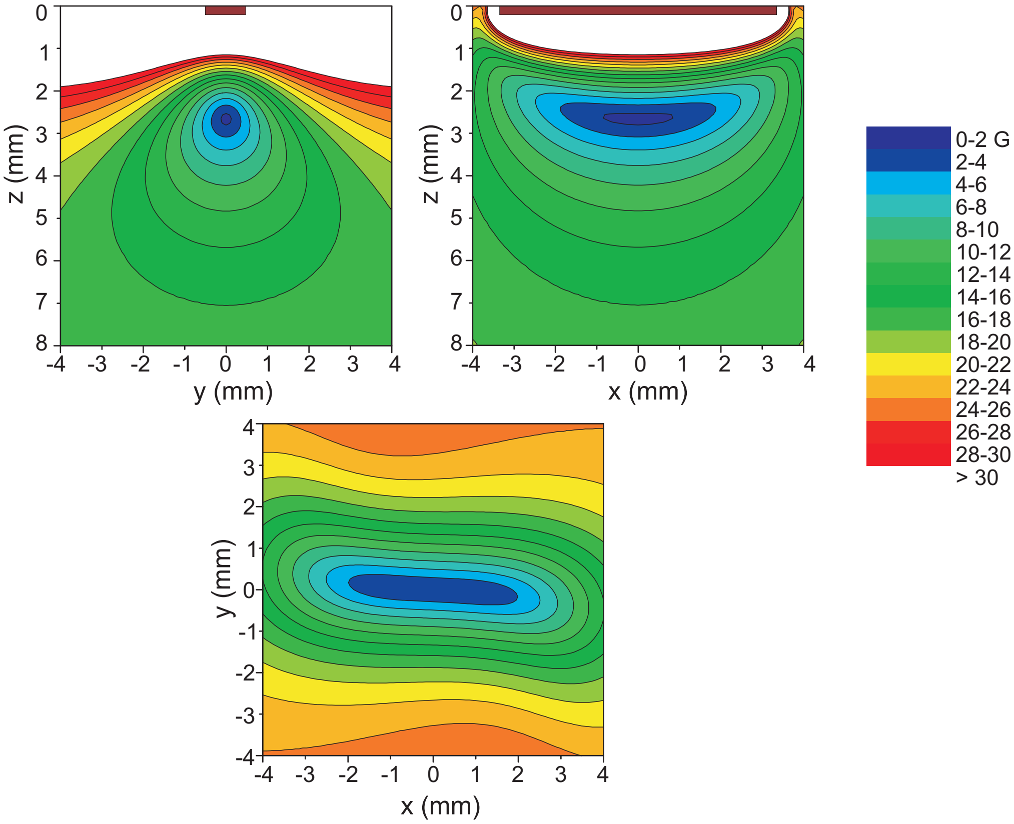

Figure 2.11: Plots of the magnetic fields of the Z-trap with the wire at 50 A, with a $y$-bias of 20 G. The origin is defined to be the center of the wire.

Once the laser beams are turned off, the atoms can be transferred to their final trap: the Z-trap. The Z-trap is a purely magnetic trap with the same topology as an Ioffe-Pritchard trap. It is formed similarly to the magnetic-field components of the U-MOT. A current of 50 A is sent through the U-Z wire in a Z-shaped configuration, as indicated in Fig. 2.8. The center bar plus the $y$-bias form a 2-D quadrupole field, just as in the case of the U-MOT. However, unlike the U-wire, the legs of the Z-wire contribute a non-zero $x$-component to the magnetic field. The result is a magnetic trap with a well-defined minimum in the center but no location where the magnitude of the magnetic field reaches zero. (If the magnetic field were to reach zero, the magnetic sublevels would become degenerate at that location, and the atoms could undergo Majorana spin flips into untrapped states, so the offset from zero at the center of the trap is necessary.) The magnetic field from the Z-wire, plus a $y$-bias, is plotted in Fig. 2.11. Note that the trap is long and shallow along the $x$-axis and approximately circular in the $y$-$z$ plane. Additionally, the long axis of the trap is not exactly along the $x$-axis but rather tilts by a small angle into the $y$-axis; this is due to the legs of the Z-wire pointing in opposite directions from each other. The trap is approximately harmonic on all three axes; due to the anisotropy of the trap, we assume that the trap frequency along the long axis is about 1/3 of the trap frequency on the other two axes. Because of the way our imaging system is set up (as promised earlier, this will be described later in the chapter), we can only directly measure the trap frequency along the $y$- and $z$-axes; this trap frequency will become relevant in the next chapter.

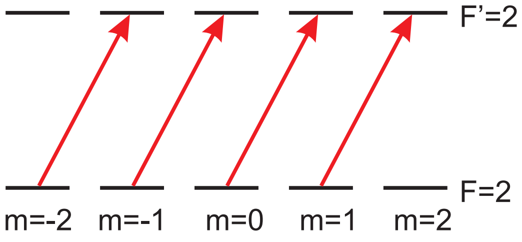

Figure 2.12: Optical pumping transitions. Red lines indicate transitions due to the laser light.

The center of the Z-trap is a local magnetic field minimum, so low magnetic field seeking states are trapped. Since the atoms are in the ground state $|5S_{1/2}, F = 2 >$, this means that the $m_F = +2$ and $m_F = +1$ magnetic sublevels are trapped, while $m_F = 0$ is untrapped, and $m_F = -1$ and $m_F = -2$ are anti-trapped. As can be seen in Fig. 2.11, the Z-trap is steeper closer to the U-Z wire (that being the source of the magnetic field) and shallower farther from it; since gravity acts on this same axis, and the gravitational potential is of the same order as the magnetic potential, under certain conditions the $m_F = +1$ sublevel might not even be trapped at all. Thus, we effectively only trap $m_F = +2$, which sees twice as strong a potential from the magnetic fields as $m_F = +1$ . Coming out of the MOT and optical molasses, the atoms are evenly distributed among all of the sublevels, however, so, if we were to transfer directly into the Z-trap, we would lose 4/5 of our atoms before we even started the first cooling step. To prevent this, we optically pump into the $m_F = +2$ sublevel. We accomplish this by using a 100 $\mu$s $\sigma$-polarized laser pulse along the $x$-axis, tuned to the $|5S_{1/2}, F = 2 > \rightarrow |5P_{3/2}, F' = 2 >$ transition. (The repumper light is also on.) We define a quantization axis along the $x$-axis by applying a slight magnetic field along only the $x$-direction, keeping the other bias coils in the same configuration as for the optical molasses. With the correct $\sigma$ polarization, the optical pumping pulse only couples the transitions $|F = 2, m_F > \rightarrow |F' = 2, m_{F'} = m_F + 1 >$; the allowed transitions are shown in Fig. 2.12. Atoms in the upper state can only decay to $m_F = m_{F'}, m_{F'} \pm 1$. After scattering only a few photons, then, most of the atoms will reach $m_F = +2$. At this point, as can be seen in Fig. 2.12, all transitions due to the laser light are forbidden, and the atoms are in a dark state. Thus, most of the atoms can be transferred to the $m_F = +2$ sublevel with minimal heating. With the help of optical pumping, we can transfer up to $\sim$ 10% of the atoms from the MOT to the Z-trap.

One feature of the Z-trap is that by increasing the $y$-bias we can move the center of the trap closer to the U-Z wire. This is because the magnetic field due to the center bar of the wire is stronger closer to the wire, so, the stronger the $y$-bias, the

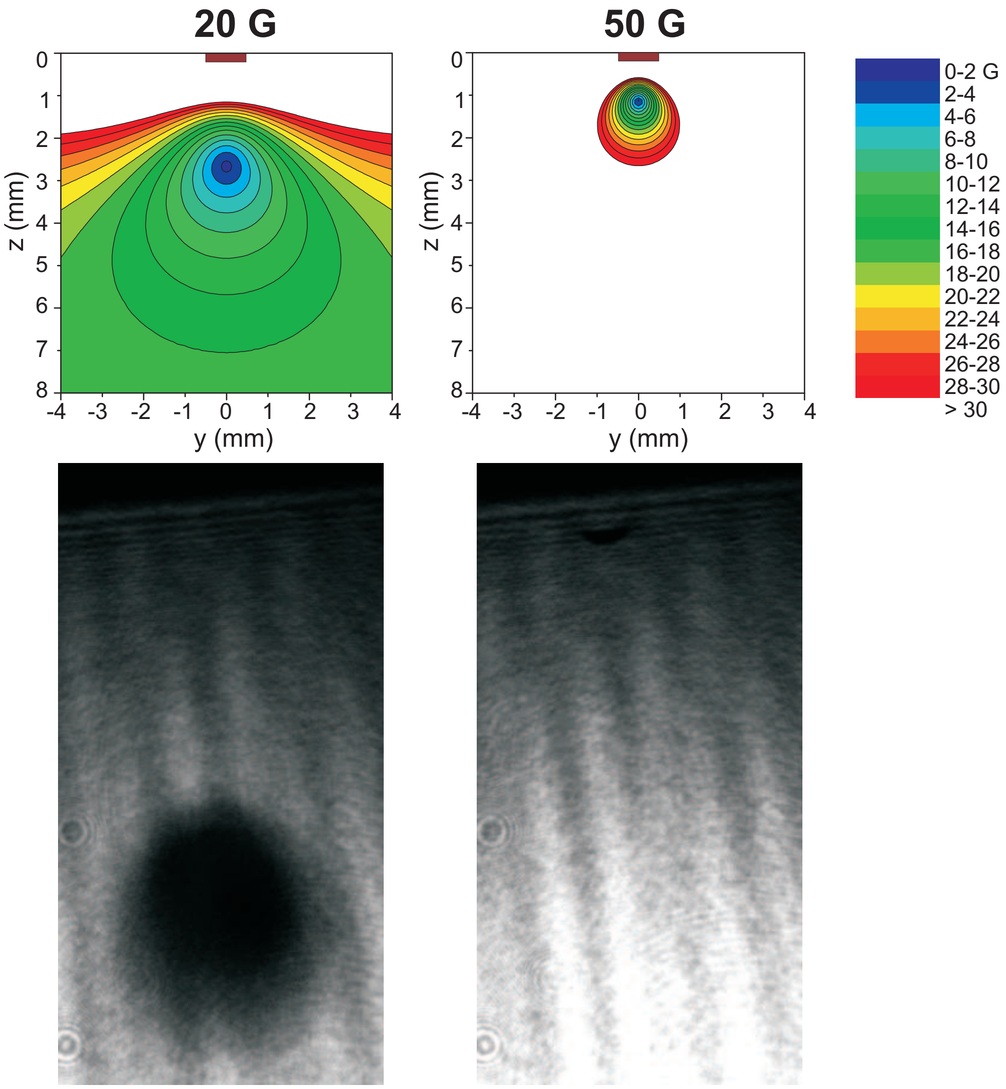

Figure 2.13: Plots of the magnetic fields and shadow images of the Z-trap, with the wire at 50 A. On the left, the y-bias is 20 G; the Z-trap is uncompressed. On the right, the y-bias is 50 G; the Z-trap is compressed. Increasing the y-bias causes the trap to move toward the wire and increases the magnetic-field gradient.

closer to the wire the field is canceled. The Z-trap created by two different $y$-biases is shown in Fig. 2.13, with plots of the magnetic fields on the top and pictures of the atoms in the Z-trap on the bottom. As can be seen in the figure, when the Z-trap is closer to the wire, the trapping potential is steeper, and the atoms are more tightly confined. There is essentially no loss of atoms due to moving the Z-trap, as long as it is moved adiabatically (we have found that adiabaticity for moving the

Z-trap typically requires time scales of ∼200 ms), so the trapped atom cloud becomes considerably denser as it is moved closer to the U-Z wire. The importance of this will be discussed in the next section.

### 2.4.4 Forced Evaporative Cooling

Now that the atoms are in the Z-trap, they can undergo the final cooling stage to reach Bose-Einstein condensation: forced evaporative cooling. Unlike the previous steps involving laser cooling, this step has no mechanism for adding new atoms to the system; there can only be losses, not gains. Thus, it is essential to maximize the efficiency of every step prior to this point so that we start out with as many atoms as possible.

The Z-trap is at most 30 MHz deep. Any atom with a kinetic energy exceeding that will be lost from the trap. There are three potential loss mechanisms. The first, and by far the most damaging, is on-resonant light. To prevent any stray light from reaching the atoms during the Z-trap stage of the experiment, the vacuum chamber is surrounded by heavy black curtains, and the ceiling above the laser table is painted black. As described near the beginning of this chapter, all light is brought to the experiment through optical fibers, with a mechanical shutter before each fiber. The second loss mechanism is background gas in the vacuum; this is the most difficult loss mechanism to prevent. If a room temperature atom or molecule collides with an atom in the Z-trap, the momentum imparted to the atom is more than enough to knock it out of the trap. For forced evaporative cooling to work in our system, the atoms need a lifetime in the Z-trap of >10 s. This necessitates vacuum pressures well below $10^{-10}$ Torr; thus, as described previously, we have taken great efforts to reach as low a vacuum pressure as possible. The third loss mechanism is that sufficiently hot atoms already have kinetic energies >30 MHz and thus quickly leave the trap.

It is this mechanism that we exploit for evaporative cooling.

When the atoms are first transferred into the Z-trap, they form a Boltzmann distribution. When the hottest atoms are selectively lost from the trap, the average temperature of the system decreases, but the Boltzmann distribution is truncated on the high-temperature end; this is a non-equilibrium distribution. After a period of time, the atoms collide with each other and rethermalize into an equilibrium distribution at a lower temperature. Now, there are atoms at the hot end of the new Boltzmann distribution that are hot enough to be lost from the trap again, although fewer than before, because the new average temperature is lower than the starting average temperature. The process repeats, and slowly the average temperature of the system is brought down. This process is referred to as evaporative cooling. It is the same mechanism by which a hot beverage is cooled (the hottest beverage molecules have enough kinetic energy to escape gravity in the form of steam) and by which skin is cooled by evaporating sweat.

Evaporative cooling is slow and inefficient. It takes an average of two collision events per atom for the system to rethermalize. Assuming the atoms start out moving at 10 cm/s on average, with a density of $10^9$ atoms/cm$^3$ (typical for the Z-trap or for a MOT to which the Z-trap must be matched for loading), a given atom undergoes collisions at a rate of $\sim$0.06 Hz, so the system can only rethermalize about twice per minute. Twice per minute is practically never, so we must increase the collision rate to have any hope of there being real cooling due to the evaporation. This is accomplished by moving the trap closer to the U-Z wire, as described above, compressing the Z-trap, and thus increasing the density (and therefore collision rate) of the trapped atoms by a factor of $\sim$100. This brings the rethermalization rate up to about three times per second, which is still slow, but at least allows for several rethermalizations in the lifetime of the atoms in the Z-trap.

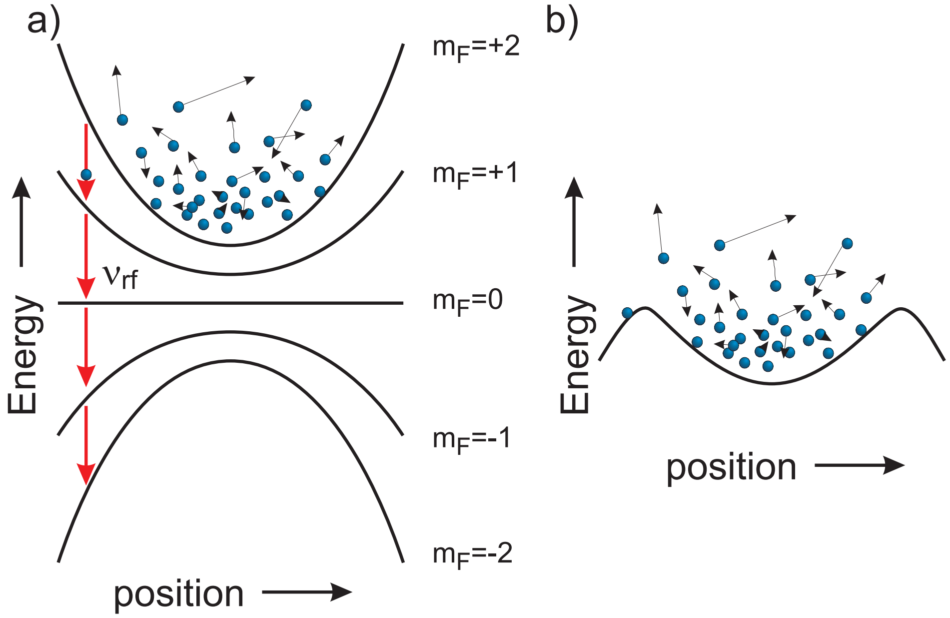

Figure 2.14: Diagram of the potentials involved in evaporative cooling in a) the non-dressed-state picture and b) the dressed-state picture with rf-coupling of frequency $\nu_{\text{rf}}$. Arrows attached to the atoms represent their velocity.

Each time the system rethermalizes, there are fewer hot atoms to be evaporated off, so the temperature drop diminishes with each iteration. To improve these diminishing returns, we can effectively lower the walls of the Z-trap after each rethermalization, allowing cooler atoms to escape. This is done by using an rf field (from a coil attached to a function generator) to couple the magnetic sublevels. The magnetic potential is given by $V(r) = g_F \mu_B B(r) m_F$, where $B(r)$ is the magnetic field, $g_F$ is the Landé g-factor ($g_F = 1/2$ in our $F = 2$ system), and $\mu_B$ is the Bohr magneton; the energy separation between the magnetic sublevels is position dependent, following the curvature of the trap. If an rf field of frequency $\nu_{\text{rf}}$ is applied, the sublevels will be coupled only at the positions where the energy levels are separated by $h\nu_{\text{rf}}$; for our 3-D harmonic trap, for a given $\nu_{\text{rf}}$, the relevant positions form an equipotential ellipsoid. Any atom that passes through this ellipsoid can undergo a transition between adjacent sublevels, eventually reaching $m_F = 0$, where it is no longer trapped, or $m_F = -1, -2$, where it is anti-trapped. It is this intentional expulsion of atoms from the trap that leads to this being called “forced” evaporative cooling. A diagram of the energy levels is shown in Fig. 2.14. Part (a) of the figure shows the potential that each energy level sees, with an arrow to indicate coupling for an arbitrary frequency $\nu_{\mathrm{rf}}$. The atoms with the lowest velocities (and thus the lowest kinetic energies) are shown toward the bottom of the trap and therefore toward the center, while atoms with higher velocities are shown higher in the trap, and therefore can be found both at the center and farther to the sides. An atom that has reached the evaporation position is shown being coupled to a lower $m_F$ sublevel. Part (b) of the figure shows the same system in the dressed state picture. In this picture it is clear that atoms with energies greater than $2h\nu_{\mathrm{rf}}$ are not trapped and can freely move out of the trap if they reach the edge.

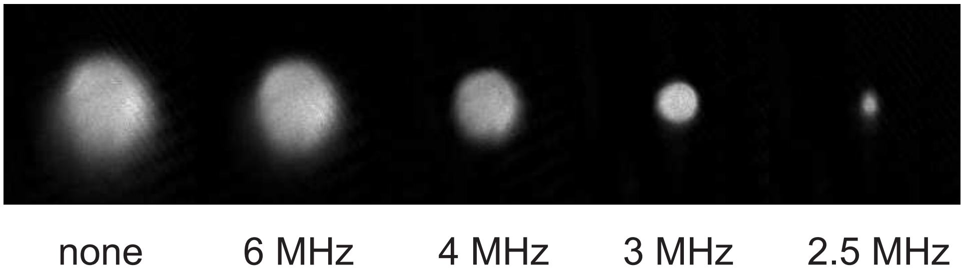

Figure 2.15: Shadow images of the Z-trap. The atoms undergo evaporative cooling; the evaporative cooling ramp is stopped at the frequency indicated for each image.

In the experiment, rather than setting a value for $\nu_{\mathrm{rf}}$, waiting for rethermalization, and then decreasing $\nu_{\mathrm{rf}}$, it is easier to do a continuous ramp. We start the ramp at $\nu_{\mathrm{rf}} = 16$ MHz and end it a few tens of kilohertz above the bottom of the trap, typically around 800 kHz (although the height of the bottom of the trap can be adjusted by changing the $x$-bias). Figure 2.15 shows pictures of the Z-trap with rf ramps to different end frequencies: as the end frequency decreases, the atom cloud gets smaller, with sharp edges defined by the equipotential ellipsoid (for clarity in the picture, the Z-trap is not compressed, so the atom cloud does not undergo true evaporative cooling but rather simply lose the hottest atoms). The faster the rf ramp, the less efficient the evaporative cooling; however, a slower ramp means more time for atoms to be lost due to background collisions. We found the optimal ramp time to be 16 s, with a linear ramp. This creates a total cycle time, including the MOT loading time, of half a minute. Unfortunately, we are not patient enough to wait half a minute between results. Additionally, such a long wait time would exacerbate any problem with slow drifts of any parameters. We find a 5 s logarithmic ramp to be a good compromise between speed and efficiency; at the end of a 5 s ramp there are $\sim 80\%$ as many atoms left as at the end of a 16 s ramp. A 20% loss is not large, particularly compared with the 90% loss due to transferring into the Z-trap and the 99% loss due to the evaporative cooling itself.

If all has gone well, at the end of the evaporative cooling ramp the atom cloud has become a BEC with 50,000-100,000 atoms. In the compressed Z-trap, the BEC density is $\sim 10^{14}$ atoms/cm$^3$, which is dense enough to have significant loss due to three-body recombination (three atoms collide, one is ejected from the trap, and the other two form a molecule). Thus, after creating the BEC, we adiabatically decompress the Z-trap by ramping down the $y$-bias over 200 ms. This has the added effect of expansion-cooling the BEC significantly, down to a few nanoKelvin.

### 2.4.5 Shadow Imaging

All that remains at this point is to try to see the BEC. While a MOT can be seen using fluorescence imaging, as in Fig. 2.6 (b), a BEC has a sufficiently small number of atoms that the fluorescence signal would be difficult to detect. Even more problematically, a BEC (or any atom distribution in the Z-trap) would be destroyed by a very small amount of incident on-resonance light, scattering very little light before dispersing entirely. Instead, we use absorption ("shadow") imaging to observe the BEC. We shine a weak, on-resonant ($|F = 2 > \rightarrow |F' = 3 >$) probe laser pulse through the BEC and onto a CCD camera. After the BEC but before the camera, the probe beam passes through a one-to-one telescope to minimize diffraction of the shadow. Due to lack of availability of window space, our probe beam propagates along the $x$-axis. As the pulse passes through the Z-trap, the light is absorbed by the atoms. We limit the pulse to 50 $\mu$s so that no significant dispersion of the atoms occurs while the beam is passing through (although the atom distribution is still destroyed by the pulse, that destruction is not observable for the first few tens of microseconds). The area density of the atoms along the path of the light, $N_{\mathrm{a}}$, is related to the percent of the light absorbed by

$$N_{\mathrm{a}} = -\frac{2I_{\mathrm{sat}}}{\Gamma h\nu} \ln\left(\frac{I}{I_{\mathrm{o}}}\right) \tag{2.1}$$

where $I_{\mathrm{sat}}$ is the saturation intensity, $\nu$ is the laser frequency, $I$ is the intensity of the light passing through the atoms, and $I_{\mathrm{o}}$ is the intensity of the light before it passes through the atoms. $N_{\mathrm{a}}$ can be calculated separately for each pixel of the CCD camera with this equation and then summed to find a total number of atoms for a given sample. In practice, $I_{\mathrm{o}}$ is measured by taking an image of the beam with no atoms. Throughout this thesis, all images are shadow images unless otherwise noted. If an image appears dark on a light (often striped) background, it is an image of $I$; if it is light on a dark background, it is an image of $N_{\mathrm{a}}$.

The pixel size for our camera is 6.7 $\mu$m on a side, which means that a BEC, which might be fewer than 10 $\mu$m across, only takes up a couple of pixels. This is insufficient to distinguish anything; in particular, we can not tell the difference between a BEC and a small, dense cloud of thermal gas. The situation can be improved by using the

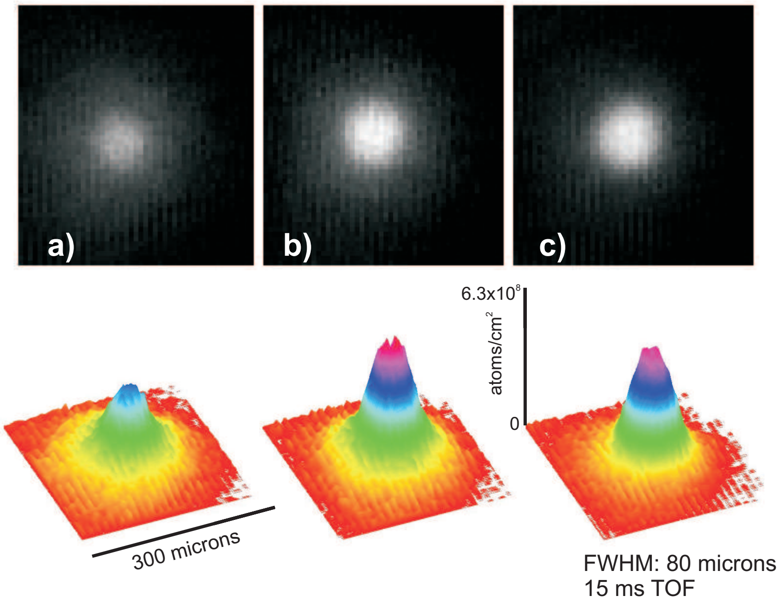

Figure 2.16: Shadow images (above) and density plots (below) of (a) a thermal cloud just above the transition temperature, (b) a small BEC surrounded by a thermal cloud right at the transition temperature, and (c) a (nearly) pure BEC just below the transition temperature.

time-of-flight (TOF) method, in which the Z-trap is turned off and the atoms are allowed to expand freely for a certain amount of time (in our experiment, typically 10-25 ms). This greatly enlarges the atom sample. On the time scale of a typical TOF, a sample expands sufficiently that no remnant of its original position-space distribution can be detected; rather, what is seen is its velocity-space distribution (or momentum-space, since all of the atoms have the same mass). Since temperature is related to momentum variance, the amount of expansion during TOF can be used to measure temperature. Measuring in momentum-space has the added benefit that a thermal gas expands faster than a BEC. The most convincing evidence that the atoms in a shadow image are a BEC is the appearance of thermal atoms in the same image to which to directly compare them. Such images are shown in Fig. 2.16. Each image in the figure is taken at a slightly different temperature by changing the end frequency of the rf ramp, with (a) being the hottest and (c) being the coldest.

Figure 2.16 (a) and (c) show a thermal cloud and a BEC, respectively; although the BEC is denser and colder, it is not obvious from the image that it is inherently different from the thermal cloud. However, Fig. 2.16 (b), taken right at the transition temperature, shows both a thermal cloud and a BEC (in the same way that water right at 0° C contains both liquid and solid components). The two components follow different distributions, as can be seen by the density plot on the bottom of the figure, which shows a broader, shorter peak and a separate narrower, taller peak. Since both components are simultaneously present and are distinguishable from each other, they must be distinct objects, and so we can be confident that the colder distribution is a BEC.

## CHAPTER III

# BEC Experiments in a 1D Optical Lattice

Figure 3.1: Wave interference on the surface of a pond due to ducks (ducks not pictured).

An optical lattice is one of the most useful tools in atom optics. Applied properly, an optical lattice can deflect atoms, much like a mirror can deflect light. It can split or combine atomic wavefunctions, analogous to a beam splitter for light. In this chapter, we vary the depth and duration of optical lattice potentials in order to manipulate atoms, creating an atom cavity and two types of atom interferometer.

## 3.1 Lattice setup

The experiments described in this chapter all use a 1-D optical lattice. This consists of a laser beam with wavelength $\lambda = 852$ nm, focused on the BEC and retro-reflected, as depicted in Fig. 3.2. The beam is brought near the vacuum chamber by a fiber, both for convenience and to clean the spatial mode of the beam. The focal point of the lattice beam has a full-width half-maximum (FWHM) of 80 $\mu$m. The intensity is varied as needed for the different experiments. The lattice beam points along the $y$-axis, as defined in the previous chapter. (Yes, it's a little bit ridiculous that my primary axis throughout this chapter will be $y$, when everyone else always uses $x$ or $z$ for everything. The axes were labeled according to convenience for making the BEC, before we set up the lattice experiments, and once axes are defined it's best to be consistent. It will get even worse in Chapter V, when—again in the name of consistency—$z$ will no longer be the axis of gravity.)

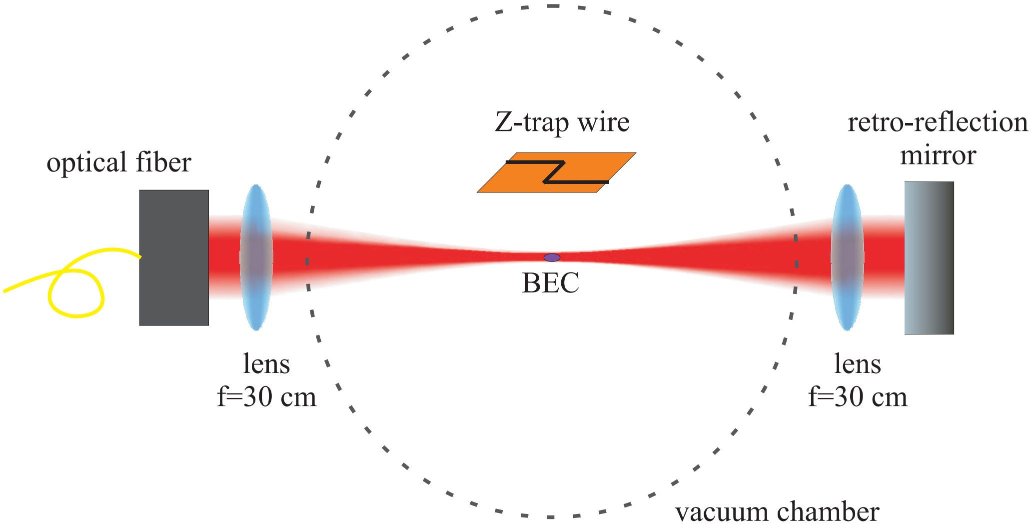

Figure 3.2: Optical lattice setup.

Since the lattice beam is far-detuned and focused, it can weakly trap atoms (it is basically a weak dipole trap). This is useful for alignment purposes, as it provides an indication that the beam is hitting the atoms. The alignment procedure is simple. First we shine the focused beam toward the BEC. When it hits it will start to trap the atoms, as can be seen in a TOF image (middle image in Fig. 3.3). Then, we move the beam and adjust the focus to optimize the trapping. Next, we set up the retro-reflection optics. When the retro-reflected beam hits the BEC, it has a drastic effect (right image in Fig. 3.3); however, it is difficult to know how to interpret the resulting TOF image, and thus determine where the effect is maximal. Instead, the retro-reflected beam can be aligned such that it couples back into the fiber whence it came. If it is optimally coupled into the fiber, it is guaranteed to be perfectly retro-reflected; thus, assuming the initial beam is perfectly aligned, the retro-reflected beam must be as well.

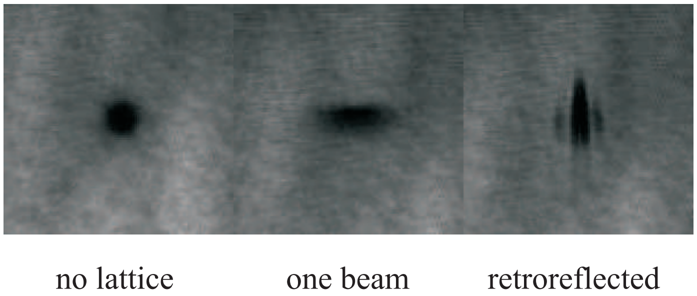

Figure 3.3: Images of a BEC with, from left to right, no lattice, one lattice beam, and the full lattice retro-reflected (but probably not perfectly aligned). The lattice beams are on continuously.

## 3.2 Bragg-Reflecting Atom Cavity

When two light beams with the same frequency counter-propagate, as in the case of an optical lattice, a standing wave is formed. If the two beams have different frequencies, they form a traveling wave moving at the velocity $v = \delta/2k$, where $k = 2\pi/\lambda$ is the wave vector. In the case of an optical lattice, if $v$ is equal to the recoil velocity of an atom when it absorbs a photon from the lattice (that is, $v = p_{\mathrm{r}}/m$, where $m$ is the mass of the atom, and $p_{\mathrm{r}} = h/\lambda$ is the recoil momentum of a photon from the lattice), then there is a resonance, and the atom is much more likely to absorb light, since absorbing a photon (from the lattice beam propagating in the opposite direction of the standing wave) will bring the atom into the lattice rest frame. The atom must then re-emit the photon; re-emission is stimulated by the light from the other lattice beam. Thus, the atom ends up with a velocity of $2v$. This is the typical situation for Bragg scattering of atoms in an optical lattice.

Changing to the lattice reference frame, this effect happens when the atom in the lattice has a momentum of $\pm p_{\mathrm{r}}$. It absorbs and re-emits a photon, and ends up with an equal but opposite momentum of $\mp p_{\mathrm{r}}$. The lattice can be said to be acting as a Bragg mirror for the atom, since, if observed in position space, the atom would appear to suddenly reverse the direction of its motion, just like light hitting a mirror suddenly reverses direction.

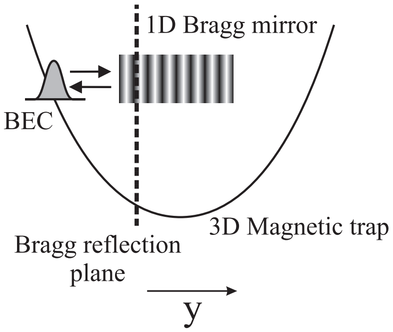

Figure 3.4: Schematic drawing of a Bragg-reflecting atomic cavity (BRAC).

### 3.2.1 Experimental Setup

It is possible to use this Bragg mirror as an atom cavity mirror. If an atom in a harmonic trap is displaced with respect to the center of the trap (along the same axis as the optical lattice), it will accelerate toward the center of the trap. When it reaches a momentum of $p_{\mathrm{r}}$ (presumably long before it reaches the center of the harmonic trap), it will be Bragg-reflected by the optical lattice, and move in the opposite direction with an initial momentum of $-p_{\mathrm{r}}$, against the curvature of the harmonic oscillator potential. As it moves up the harmonic oscillator potential it decelerates, stopping when it reaches its initial starting point. Then it starts over again, accelerating back toward the center of the trap. This "Bragg-reflecting atom cavity" (BRAC) is depicted in Fig. 3.4. An interesting feature of the BRAC is that the reflections are based on the momentum of the atom, as opposed to the position-dependent reflections in a traditional cavity.

In the case of our experiment, the Z-trap provides just such a harmonic oscillator potential to allow us to create the BRAC. Since it is difficult to work with a single atom–both preparing it and imaging it are non-trivial tasks–we prefer to use a BEC. A BEC behaves as a single, macroscopic wavefunction, so for the purpose of this experiment it should be just as good as a single atom (although, as described later in this section, the fact that a BEC is made up of multiple atoms that interact with each other can cause problems). Luckily, we have a BEC, as described in Chapter II. In order to see the BRAC, we want the harmonic trap to be relatively shallow, so that it takes more time for an atom to reach one recoil momentum. Thus, we decompress the Z-trap (as described in Chapter II) until it has a trap frequency of 45 Hz in the $y$ direction.

The optical lattice used for the Bragg reflection is as described in the above section, and is set to a low amplitude (the lattice potential depth in this case is one recoil energy, $E_{\mathrm{r}} = h^2/2\lambda^2 m$), so that it does not affect the BEC other than during Bragg reflection. The lattice beams have a turn-on time of about 1 $\mu$s, negligible compared to all other time scales in the experiment.

To create the initial conditions depicted in Fig. 3.4, rather than moving the BEC away from the center of the Z-trap, we shift the Z-trap out from under the BEC. We do this by ramping up the bias along the $z$-axis by 100 mG over 2 $\mu$s; this translates the center of the Z-trap by 30 $\mu$m in the $y$ direction. This occurs quickly enough that the BEC does not have time to move during the translation.

The position-space oscillation of the BEC would be impossible to observe because it covers a range of only about 5 $\mu$m (remember from Chapter II that the resolution of our imaging system is 6.7 $\mu$m, at best). Therefore, we can only measure the oscillation of the BEC in momentum space, using time-of-flight (TOF, see Chapter II). In this case, in addition to turning off the Z-trap, we must also turn off the lattice beam. For this experiment, the TOF is 15 ms.

After the decompression, the BEC has a small, random momentum, $p_0$, due to 60 Hz noise in the magnetic field. This random momentum leads to a phase shift in the oscillation, which causes a time jitter of up to $\pm0.5$ ms in the observed Bragg reflections. To minimize the effect of this jitter, we take five separate TOF images for each time step, compare the BEC momenta, and choose the median image.

### 3.2.2 Experimental Results

Figure 3.5 (a) shows TOF images of the BEC after different evolution times inside the cavity. The horizontal axis of each image is momentum in $y$-direction. As can be seen in the figure, as the evolution time increases, the momentum of the BEC increases approximately linearly (due to the magnetic force from the trap). The momentum reverses at 3 ms and 7 ms due to Bragg reflection; these reflections occur at times when the BEC reaches a momentum of $+p_{\mathrm{r}}$.

To characterize the BRAC, we apply different Z-trap displacements. In addition to 30 $\mu$m, we initially displace the trap by 44 $\mu$m, 60 $\mu$m and 74 $\mu$m. The corresponding data are shown in Fig. 3.5 (b)-(d), respectively. As can be seen, the oscillation period decreases with increasing displacement, but looks qualitatively similar for

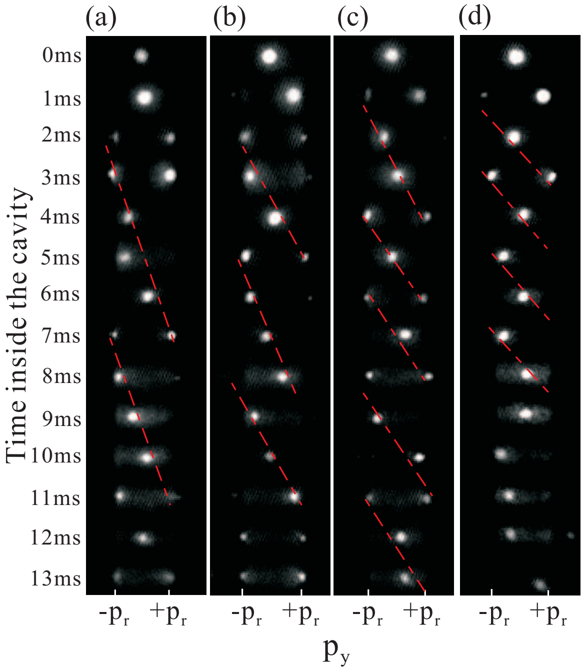

Figure 3.5: Momentum distribution of the BEC inside the atom cavity. The BEC is initially displaced by different amounts from the center of the Z-trap. (a)-(d) correspond to 30 $\mu$m, 44 $\mu$m, 60 $\mu$m and 74 $\mu$m displacements, respectively. Dashed lines are to guide the eye.

all displacements, indicating the BRAC is consistent. Since the BEC experiences a larger force farther away from the trap center, it accelerates faster, taking less time to reach a momentum of $+p_{\mathrm{r}}$. We have observed as many as five oscillations, as in Fig. 3.5 (c). Based on the images, for large initial displacements it may be possible to observe significantly more than five oscillations; however, five is sufficient for a proof-of-concept. During the Bragg reflection process, both momentum components, $+p_{\mathrm{r}}$ and $-p_{\mathrm{r}}$, are present in the BEC, as can be seen in the figure. Considering the regularity with which images containing both momentum components are seen, we estimate that the Bragg-reflection process takes on the order of 1 ms.

We calculate the oscillation period, $T$, based on the assumption that the optical lattice only acts as a Bragg mirror and does not affect the BEC elsewhere. Therefore, $T/2$ is the time it takes for the BEC to accelerate to one recoil momentum in the

Z-trap under the initial conditions, where the BEC is stationary and located at a distance of $y_0$ from the center. For small $y_0$, as in this experiment, the Z-trap can be approximated by a harmonic potential, which leads to the following equation for the period $T$:

$$m\omega y_0 \sin\left(\omega\frac{T}{2}\right) = p_{\mathrm{r}} = \frac{h}{\lambda}, \tag{3.1}$$

where $\omega = 2\pi\times45$ Hz is the frequency of the harmonic trap in the $y$-direction. Since

$$T = \frac{2}{\omega}\sin^{-1}\left(\frac{h}{m\omega y_0\lambda}\right) \simeq \left(\frac{2h}{m\omega^2\lambda}\right)\frac{1}{y_0} = \frac{A}{y_0}\,, \tag{3.2}$$

$T$ is an approximately linear function of $1/y_0$ with a slope $A = 147$ ms $\mu$m.

From Fig. 3.5, we can measure $T$ experimentally for different displacements $y_0$. The resulting period as a function of $1/y_0$ is plotted in Fig. 3.6. Also shown in Fig. 3.6 is a linear fit of the experimental data. The fit yields a slope of 137 ms $\mu$m. Based on the error bars of the data points, the uncertainty of the slope is estimated to be ±15 ms $\mu$m. Within this uncertainty, experimental and theoretical values of the slope agree with each other.

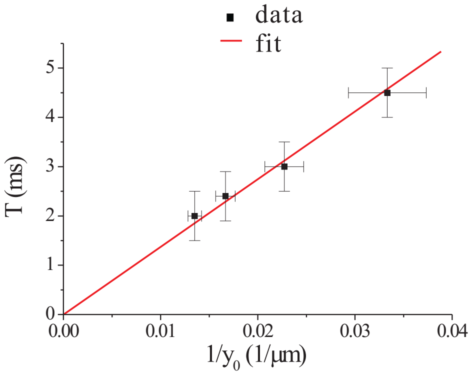

Figure 3.6: Oscillation period T as a function of $1/y_0$. A linear fit of the experimental data yields a slope of 137 ms $\mu$m.

### 3.2.3 Comparison to Bloch Oscillations

Several experiments on Bloch oscillations of thermal atoms or a BEC have have been done by other groups with results resembling our BRAC [13, 14, 53]. In these experiments, atoms were placed in a lattice with a constant acceleration. This results in a situation similar to traditional Bloch oscillations: an atom travels through the first Brillouin zone, and when it reaches the end of the Brillouin zone it reappears at the beginning and travels through again. Thus, the quasi-momentum increases to a $2\pi/\lambda$, hops to $-2\pi/\lambda$, and increases again. In these Bloch oscillation experiments the atoms were subjected to a constant force, while in our BRAC experiments they were subjected to a harmonic force. Qualitatively, however, our experiments are very similar. Several experiments have shown that at high densities typical of a BEC, mean-field cause the BEC to be unstable during Bloch oscillation, and so only a few oscillations are possible; to see several oscillations it is necessary to tune the scattering length of the atoms to zero [14, 54, 55]. However, in our experiments, the BEC does appear to be stable over several oscillations. This is because the mean-field force on the BEC is position dependent, and is equal and opposite to the potential energy of the BEC when it initially sits at the center of the trap, satisfing the condition that the chemical potential, which is the sum of the mean-field potential and the trap potential, is zero at all positions; *i.e.*

$$V_{\mathrm{mf}} = \mu - \frac{1}{2}m(\omega_x^2 x^2 + \omega_y^2 y^2 + \omega_z^2 z^2)\,. \tag{3.3}$$

When the BEC is displaced by a distance $y_0$, the resultant potential is

$$\begin{aligned} V &= \frac{1}{2}m(\omega_x^2 x^2 + \omega_y^2 (y-y_0)^2 + \omega_z^2 z^2) + V_{\mathrm{mf}} \qquad (3.4)\\ &= \frac{1}{2}m\omega_y^2 (y_0^2 - y_0 y)\,. \qquad (3.5) \end{aligned}$$

The force is then

$$F = \frac{1}{2} m \omega_y^2 y_0 \,. \tag{3.6}$$

Thus, the curvature of the trap and the position-dependent mean-field gradient cancel, resulting in the BEC experiencing a constant force. Unlike all of the standard Bloch oscillation experiments, in our particular experiment mean-field effects increase the stability of the BEC as it oscillates [56].

### 3.2.4 A First Attempt at an Interferometer

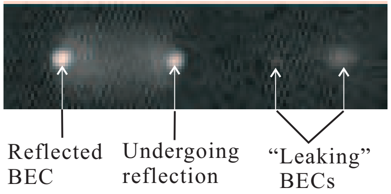

Figure 3.7: TOF image of BECs after 7 ms in trap, with an initial displacement of 74 $\mu$m. Leaking BECs from multiple Bragg reflections are observed.

Looking carefully at Fig. 3.5 (d), one can see that a small portion of the BEC reaches momenta greater than $p_{\mathrm{r}}$; this is especially visible in the 12 ms image. This indicates that the BEC can "leak" through the Bragg mirror. The leaking BEC continues to accelerate due to the magnetic trap and reaches momenta well beyond $p_{\mathrm{r}}$. Occasionally the leaking BEC is quite prominent in the data, as shown in Fig. 3.7.

This suggests the possibility of using the atom cavity to make an atom interferometer. The initial displacement of the magnetic trap would have to be chosen such that the BEC reaches $p_{\mathrm{r}}$ at the center of the trap; this way, the reflected and unreflected BEC components will have equal but opposite momenta through their entire paths. The optical lattice would be pulsed on at times $T/4$ and $3T/4$, so that the BECs become split when they travel through the center of the magnetic trap. A 50/50 wavepacket splitting could be achieved by adjusting the lattice depth and duration so that the atoms are Bragg-reflected into a well-defined order. The two optical-lattice pulses would be analogous to the 50/50 beam splitters in a traditional Mach-Zehnder interferometer. The first pulse would split the BEC into two components, each taking a different path. When the components return to the center of the trap, the second pulse would remix them. The population of atoms in each final component would depend on the relative phase difference between the two paths, which in turn would depend on perturbations; these could be gravitational or inertial effects, differential mean-field shifts, or a variety of other measurable forces.

Unfortunately, we could not perform this experiment. The small, random initial momentum, $p_0$, mentioned above, leads to significant shifts in position compared with the small position shift necessary to have the BEC not reach $p_\mathrm{r}$ until it arrives at the center of the trap. In other words, the apparatus is not stable enough to use for an interferometer based on Bragg scattering. So, in the next section, we try a different approach.

## 3.3 Kapitza-Dirac Scattering

When a standing wave is applied to cold atoms for a duration that is sufficiently short that the atoms are stationary while the lattice is applied, the system is in the Kapitza-Dirac (KD) scattering regime (analogous to the Raman-Nath regime in optics). The 1-D optical lattice adds a potential

$$V(y) = -V_0(1 - \cos(2k_\mathrm{L} y)) \tag{3.7}$$

to the atoms over the time interval $\Delta t$ that the lattice is on. $2V_0$ is the lattice depth, and $k_\mathrm{L}$ is the wavenumber of the lattice beams. Assuming an initial wavefunction $\psi(y, t = 0) = 1$, the wavefunction after the lattice pulse is, neglecting a global phase factor,

$$\psi(y, t > 0) = \exp\left(i\frac{V_0 \Delta t \cos(2k_{\rm L} y)}{\hbar}\right)$$
$$= \sum_{n=-\infty}^{\infty} (i)^n J_{\rm n}\left(\frac{V_0 \Delta t}{\hbar}\right) \exp(i2nk_{\rm L} y) \ . \qquad (3.8)$$

The expression in the sum shows that the BEC breaks up into discrete components with momenta that are integer multiples of $2\hbar k_{\rm L}$ and with amplitudes given by Bessel functions (of the form $J_{\rm n}(x)$) [57, 58].

### 3.3.1 Using KD Scattering for Lattice Depth Calibration

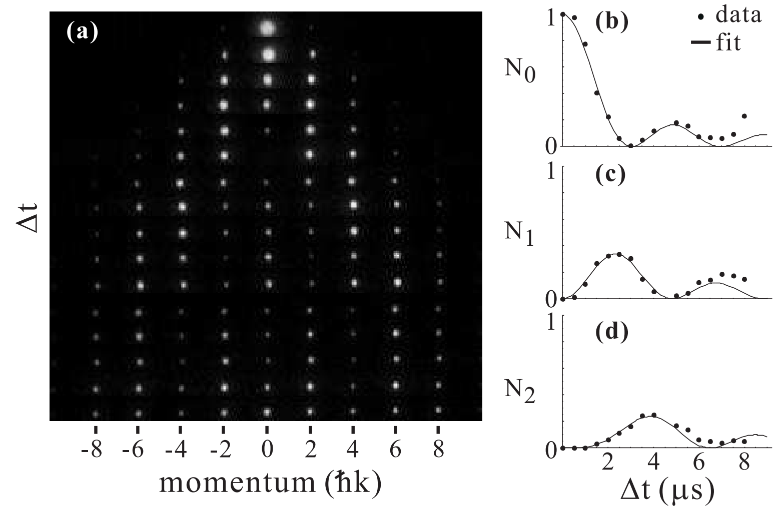

Figure 3.8: (a) TOF images of Kapitza-Dirac scattering as a function of lattice duration $\Delta t$, in steps of 0.5 $\mu$s, starting from 0.5 $\mu$s at the top. (b)-(d) Scattering ratios $N_{\rm n}/N_{\rm T}$, as defined in the text, for the scattering orders $n = 0$, 1, and 2, respectively, as a function of lattice duration. The data in (b) are fit with $J_0^2(a\Delta t)$, with best-fit parameter $a$=0.79 $\mu$s$^{-1}$. The lines in (b)-(d) show $J_{\rm n}^2(0.79\ \mu{\rm s}^{-1}\ \Delta{\rm t})$ with respective values of $n$.

When a BEC undergoes KD scattering, the relative splitting into different momentum components can be measured and compared to Bessel functions in order to find the lattice depth. In particular, the first zero of the zeroth-order Bessel function, $J_0(x) = 0$, occurs at $x = 2.4048$. Thus, the $n = 0$ component of a BEC undergoing KD scattering first vanishes at a time $\Delta t_0$ for which $V_0 = 2.4048\hbar/\Delta t_0$. The lattice depth $2V_0$ can then be found by measuring the time $\Delta t$ at which the $n = 0$ order first vanishes [59]. For an atomic polarizability $\alpha$ and a single-beam lattice intensity $I_1$, the lattice depth is also given by $2V_0 = \alpha I_1/(2c\epsilon_0)$. Using these equations, the lattice depth can be experimentally calibrated against anything directly proportional to $I_1$, such as the measured beam power. This method is considerably more reliable than the simple method of measuring the beam profile and intensity directly, which only provides the ideal lattice depth. In that case, any misalignment of the lattice with respect to the atom cloud (which can be nearly impossible to detect, since the inside of a vacuum chamber tends to lack alignment markers, and the atom cloud may be as small as 10 $\mu$m) decreases the beam intensity, and therefore the lattice depth, by an unknown amount from what was originally measured. By contrast, KD scattering provides an immediate, beam-profile- and alignment-insensitive lattice-depth calibration, because it is based directly on the lattice's effect on the atom cloud.

To induce KD scattering, the optical lattice is applied to the BEC for a few microseconds. The lattice and the trap are then turned off simultaneously. The BEC is allowed to expand freely in TOF for 16 ms. After the expansion, we take absorption images, shown in Fig. 3.8 (a). For each scattering order $n$, we measure the atom number $N_{\mathrm{n}}$ ($N_{\mathrm{T}}$ is the total atom number). In Fig. 3.8 (b) we plot $N_0/N_{\mathrm{T}}$ vs $\Delta t$ and find the lattice duration $\Delta t_0$ where this ratio first approaches zero; the corresponding lattice depth is $4.81\hbar/\Delta t_0$. In this way, we determine the proportionality constant relating the lattice-power reading to the lattice depth. Typically, we find $\Delta t_0 \sim 3\mu$s. For example, in Fig. 3.8, by fitting the $N_T/N_0$ with $J_0^2(a\Delta t)$, we find $\Delta t_0 = 3.02\mu$s, with a fit error of $\sim 1\%$. This is well within the validity range of the short-pulse approximation we made at the beginning of this section, as evidenced by the fits in Fig. 3.8 (b) which match the data well up to 6 $\mu$s. Overall, we estimate our lattice depth uncertainty to be $\sim 5\%$. Most of this uncertainty is not intrinsic to the method, but rather is due to slow drifts in lattice alignment over the course of our measurements, post-calibration. We typically calibrate our lattice depth once, or occasionally twice, per day, either at the beginning or the end of a data run. Furthermore, this procedure is used to initially align the lattice with respect to the BEC: better overlap between the lattice and the BEC leads to a smaller $\Delta t_0$ (this was unnecessary in the previous section, because the BRAC requires a very small lattice depth but the exact depth is not important).

### 3.3.2 Small-Separation Atom Interferometer

In addition to calibration, KD scattering can be used to create an interferometer, similar to the hypothetical one described at the end of the section on the BRAC. We demonstrate two different schemes for making an interferometer based on KD scattering. The first scheme, a small-separation atom interferometer (presented in this section) can be used on thermal or Bose-Einstein condensed (BEC) atoms to produce high-contrast interference patterns with many fringes. The second scheme, a large-separation atom interferometer (presented in the next section) can be used on a BEC to achieve a highly sensitive, large-separation atom interferometer, in which the maximal distance between the BEC components is sufficient that the components can be addressed separately.

A schematic of the first interferometry method is shown in Fig. 3.9. We use two KD scattering pulses: one to initially split the atomic wavefunction into multiple components and the other to recombine some of those components. When we split and recombine the components, we want the resultant interference pattern to arise from the interference of only two components. If more than two components interfere, the pattern becomes more complicated and thus less straightforward to analyze. We

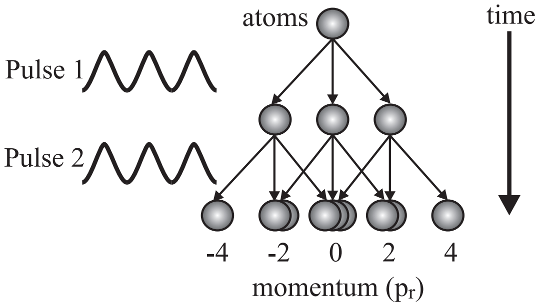

Figure 3.9: Schematic of the small-separation atom interferometry method, represented in momentum space. This method can be used for both a thermal cloud and a BEC.

also want the interfering orders to have approximately equal amplitudes, in order to maximize the visibility of the interference pattern. In this case, the lattice depth is about 80 $E_\mathrm{r}$ (found through the calibration method described above). We choose $\delta t = 2\ \mu$s, corresponding to $V_0 \delta t/\hbar = 1.6$. This causes only a small portion of the wavefunction to be in orders higher than 1 ($\sim 6\%$ of the wavefunction probability is scattered into each of the $\pm 2$ orders), and approximately equal amounts in the -1, 0, and +1 orders. After the application of the first KD scattering pulse, a time interval $\Delta t$, in the range of hundreds of microseconds, is allowed to pass. During this time, the $\pm 1$ orders move slightly in the trap due to the momentum imparted to them by the KD scattering. After $\Delta t$, a second KD scattering pulse is applied. The wavefunctions in each order $n$ are split again into several orders $n'$. After both KD scattering pulses, the momentum of a component of the wavefunction is given by $2(n + n')\, p_\mathrm{r} + p_0$ (neglecting the momentum change due to the magnetic trap). With the second pulse, we again want to coherently split the wavefunction components into the orders $n' = 0$ and $n' = \pm 1$ with approximately equal amplitudes, while avoiding orders $|n'| \geq 2$. Thus, we also pick $\delta t = 2\ \mu$s for the second pulse. Immediately after the second KD scattering pulse, the magnetic trap is turned off and the atoms undergo 20 ms of TOF. During the TOF, the wavefunction components spread into each other and interfere if they have approximately the same momentum, *i.e.* if their values of $n + n'$ are equal. If they have significantly different momenta, *i.e.* their values of $n+n'$ are different, they do not interfere, but rather gain macroscopic separation during TOF.

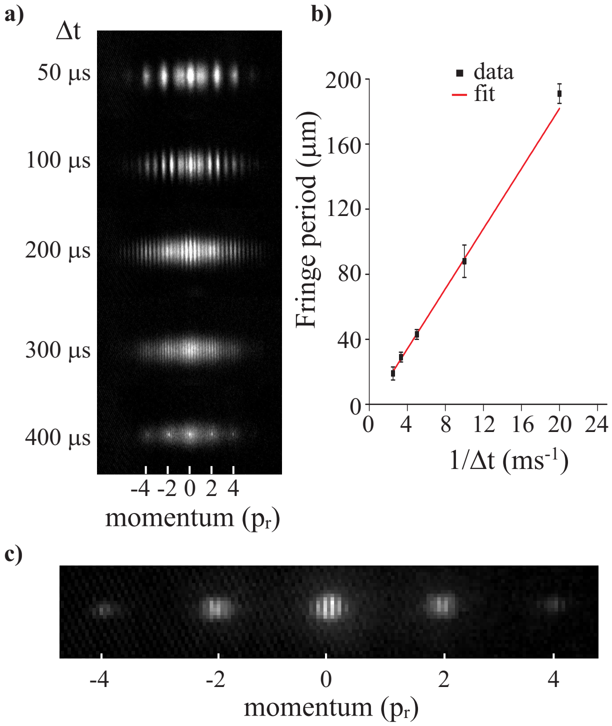

Figure 3.10: (a) Thermal-cloud interference with different time intervals, $\Delta t$, between KD scattering pulses. (b) Fringe period of interference for a thermal cloud vs $1/\Delta t$. (c) BEC interference, for $\Delta t = 420$ $\mu$s between pulses.

The description in the previous paragraph applies to a single atom interfering with itself. However, the experiment can be performed on a thermal cloud cooled to a sufficiently low temperature. At very low temperatures, the atoms in the thermal cloud will have similar enough momenta that even though the resulting measurement is an incoherent sum over all of the atoms, the interference pattern can still be seen [60]. We perform this experiment on a thermal cloud consisting of 2-3.5$\times10^5$ atoms evaporatively cooled to just above the BEC transition. The results for various delay times $\Delta t$ are shown in Fig. 3.10 (a). As can be seen, interference fringes are clearly visible up to $\Delta t = 400\ \mu$s. At image positions corresponding to momenta $\pm 2p_{\mathrm{r}}$ in Fig. 3.10 (a), two wavefunction components interfere with each other, namely the components $(n,n')=(0,\pm 1)$ and $(\pm 1,\ 0)$. As a result, at these image positions the interference patterns exhibit regular, sinusoidal interference fringes. The fringe contrast varies with $\Delta t$; at $\Delta t = 50\ \mu$s a fringe contrast of over 90% is observed, while at $\Delta t = 400\ \mu$s the fringe contrast is only 33%. At the center of the images in Fig. 3.10 (a), three wavefunction components interfere with each other, namely $(n,n')=(0,0)$, $(1,-1)$, and $(-1,1)$, resulting in more complicated interference patterns. The interference patterns near zero momentum are most visibly complex when the fringe period is largest, at small $\Delta t$.

To obtain the fringe period, $\lambda_{\mathrm{f}}$, from our experimental data, we determine the average distance between adjacent peaks for a given $\Delta t$, using multiple images, and ignoring the center region where the fringe pattern is more complex. The resulting plot, $\lambda_{\mathrm{f}}$ vs $1/\Delta t$, is shown in Fig. 3.10 (b). The error bars shown in the figure are based on estimated reading uncertainties due to camera resolution and the number of samples. Applying a linear fit, we find a slope of $9.2\ \mu\mathrm{m}\cdot\mathrm{ms}$, with a fit uncertainty of $\pm 1.1\ \mu\mathrm{m}\cdot\mathrm{ms}$.

The fringe period can also be calculated analytically and using simulations. To find $\lambda_{\mathrm{f}}$ analytically, we assume the wavefunction is initially in the ground state of the harmonic potential (in this case, we have decompressed the trap such that $\omega = 2\pi \times 45$ Hz). The first KD scattering pulse splits the wavefunction into several components with momenta differing by multiples of $2p_r$. Since the harmonic trap is left on between the KD scattering pulses, these components propagate without dispersion and maintain a position uncertainty of $\sigma = \sqrt{\hbar/2m\omega}$. The expectation values of the positions and momenta of the components follow the classical equations of motion of the harmonic oscillator. The second KD scattering pulse, applied at time $\Delta t$, then splits the evolved wavefunction components a second time. After the second KD scattering pulse the harmonic-oscillator potential is turned off, and the wavefunction components propagate according to the equation for a free Gaussian wave packet,

$$\psi_l(y,t) \propto \frac{\exp(ik_l y - iE_l t/\hbar)\exp(\frac{-(y-y_l-\hbar k_l t/m)^2}{4\sigma^2(1+i\hbar t/(2\sigma^2 m))})}{\sqrt{2\pi(1+i\hbar t/(2\sigma^2 m))}} \quad . \tag{3.9}$$

Here, $y_l$ and $k_l$ are the expectation values of the position and momentum of component $l$ immediately after the second KD scattering pulse, and $t$ is the time elapsed after turning off the harmonic potential. The interference pattern after time-of-flight is obtained by setting $t = t_{\mathrm{TOF}}$ and summing over all wave packet components. Specifically, the periodicity $\lambda_{\mathrm{f}}$ of the interference pattern in the overlap region of two components, $l1$ and $l2$, follows

$$2\pi/\lambda_{\mathrm{f}} = |\frac{\partial\psi_{l1}}{\partial y} - \frac{\partial\psi_{l2}}{\partial y}| \tag{3.10}$$

where $\psi_{l1}$ and $\psi_{l2}$ are the phases of wave packet components $l1$ and $l2$. After extracting $\psi_{l1}(y,t)$ and $\psi_{l2}(y,t)$ from Eq. 3.9 and taking the spatial derivatives, Eq. 3.10 leads to

$$\lambda_{\mathrm{f}} = \frac{2\pi}{m}\left(\frac{4m^2\sigma^4 + \hbar^2 t_{\mathrm{TOF}}^2}{-4mk_{\mathrm{rel}}\sigma^4 + \hbar t_{\mathrm{TOF}} y_{\mathrm{rel}}}\right) \tag{3.11}$$

with $k_{\mathrm{rel}} = k_{l2} - k_{l1}$ and $y_{\mathrm{rel}} = y_{l2} - y_{l1}$. Maximum interference contrast occurs when the two wavepackets overlap exactly based on their classical trajectories, $t_{\mathrm{class}} = -my_{\mathrm{rel}}/(\hbar k_{\mathrm{rel}})$. At that point, the fringe period $\lambda_{\mathrm{f}}$ equals $\lambda_{\mathrm{class}} = 2\pi/k_{\mathrm{rel}}$. Since the wave packets spread considerably during time of flight, they do not have to overlap perfectly in order for high-contrast to occur. For times $t_{\mathrm{TOF}}$ different from $t_{\mathrm{class}}$, the resulting fringe periods $\lambda_{\mathrm{f}}$ are different from $\lambda_{\mathrm{class}}$. To find $\lambda_{\mathrm{f}}$ for our experiment, we may consider, for example, the interference of the scattering orders $(n, n') = (0, 1)$ with $(n, n') = (1, 0)$. For these, $k_{\mathrm{rel}} = 2k_{\mathrm{L}}(\cos(\omega\Delta t) - 1)$ and $y_{\mathrm{rel}} = (2p_{\mathrm{r}}/m\omega)\sin(\omega\Delta t)$. Under the conditions of our experiment, the terms in Eq. 3.11 that involve $\sigma$ are much smaller than the terms that involve the TOF, $t_{\mathrm{TOF}}$. Additionally, $\omega\Delta t \ll 1$, and so $y_{\mathrm{rel}} \approx 2p_{_\mathrm{r}}\Delta t/m$. Thus, Eq. 3.11 simplifies to

$$\lambda_{\mathrm{f}} \approx \frac{ht_{\mathrm{TOF}}}{2p_{\mathrm{r}}\Delta t}. \tag{3.12}$$

This is the same equation as given in Ref. [60] for the case of free evolution between pulses and in the absence of mean-field interaction. Therefore we can conclude that in this small-separation interferometry scheme, where $\omega\Delta t \ll 1$, the presence of the harmonic trap between the KD scattering pulses has no significant effect on the fringe period. According to Eq. 3.12, in our system we expect $\lambda_{\mathrm{f}} = \frac{1}{\Delta t} \times 8.5\mu\mathrm{m} \cdot \mathrm{ms}$. This is in reasonable agreement with our experimental observations.

So far, we have only discussed the case where the wavefunction is in the ground state; however the experimental results presented so far used thermal clouds, which, although quite cold, are certainly not in the ground state. In fact, we can see at least some interference for temperatures up to $T \sim 650$ nK. The temperature is determined, as explained in Chapter II, by finding the FWHM of the shadow image of the atom cloud. In this case, we must do this analysis perpendicular to the lattice direction, because in the lattice direction the cloud spreads out considerably. Due to uncertainties in the size of the initial atom cloud before TOF, the uncertainties of the temperature measurements are $\sim 50$ nK (which corresponds to a fairly high relative uncertainty for the lowest temperature thermal clouds). The contrast falls off considerably at higher temperatures, eventually disappearing completely.

We can also implement this interferometry scheme using BECs of 5-8$\times 10^4$ atoms. Since the spatial extent of the BEC components after time of flight is much smaller

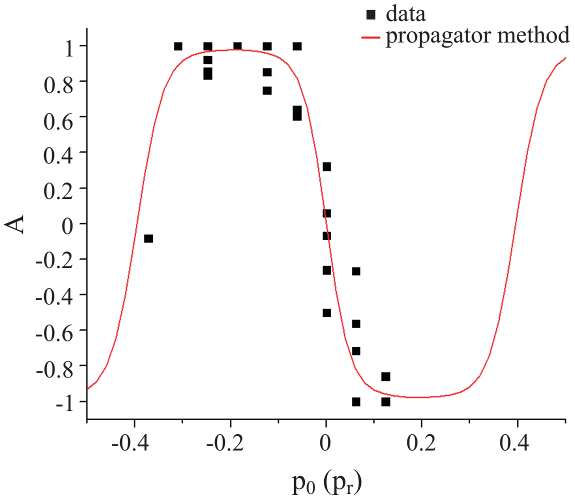

Figure 3.11: Asymmetry between the number of BEC atoms with a final momentum $+2p_{\mathrm{r}}$, $P_+$, and the number of BEC atoms with a final momentum $-2p_{\mathrm{r}}$, $P_-$, defined by $A = \frac{P_+ - P_-}{P_+ + P_-}$, as a function of the initial momentum $p_0$, for $\Delta t = 100$ $\mu$s. Squares are experimental data; solid line is a simulation based on propagators.

than that of cold thermal clouds, it is harder to see interference in BECs than in cold thermal clouds. Fringes in BECs can only be observed if the fringe period, $\lambda_{\mathrm{f}}$, is less than the size of the BEC components after TOF but still larger than the spatial resolution of the imaging system (which, in this case, is 6.7 $\mu$m). These contrasting requirements mean that BEC interference fringes can only be observed over the range 300 $\mu$s $\lesssim \Delta t \lesssim$ 800 $\mu$s. In Fig. 3.10 (a) we see that in the case $\Delta t = 400$ $\mu$s, where there is a mix of thermal cloud and a very small BEC, a single interference fringe is only slightly smaller than a BEC component. In Fig. 3.10 (c), we show BEC inteference for $\Delta t = 420$ $\mu$s; several interference fringes are visible in each BEC component. For $\Delta t \lesssim 300$ $\mu$s, the interference fringes are too wide to be visible, but any asymmetry between the paths of the +1 and -1 components will still cause a phase shift in the interference. These phase shifts manifest as one component having a greater amplitude than its symmetric component in the TOF image. An example leading to asymmetry between the paths of the +1 and -1 components is the initial momentum of the wavefunction, $p_0$. As mentioned several times by now, this apparatus is plagued by 60 Hz noise in the magnetic trap, causing random shot-to-shot fluctuations of $p_0$ over a range $|p_0| \lesssim 0.4\ p_{\rm r}$. In this one special case, we can use the existence of a non-zero $p_0$ to our advantage: we can test the ability of our interferometer to make a measurement (of $p_0$). The asymmetry in the interference pattern caused by the fluctuations in $p_0$ can be quantified by comparing the number of atoms $P_-$ and $P_+$ with momenta $-2p_r$ and $+2p_r$, respectively, in the TOF images. In the presence of a cold thermal cloud, $p_0$ can be measured by using the interference of the thermal cloud as a reference. A thermal cloud has a sufficiently wide range of initial momenta that its interference pattern is independent of small variations in the average momentum. Thus, the center of the thermal cloud interference pattern can be taken as $p = 0$. The initial momentum of the BEC can then be found by comparing the position of the BEC component with $n + n' = 0$ to the $p = 0$ position as indicated by the thermal cloud.

For several experimental images, we plot the asymmetry of $P_-$ and $P_+$, defined as $A = (P_+ - P_-)/(P_+ + P_-)$, as a function of $p_0$, in Fig. 3.11 (squares). By itself, this tells us nothing, except that $p_0$ affects the interference pattern, as expected since the purpose of an interferometer is to measure things like this (although preferably not noise in normal operation). However, it is possible to do a numerical simulation, using propagators, as in Eq. 3.9. We plot the results in Fig. 3.11 (line). The experimental data agree well with the theoretical result based on propagators, showing that the experimental shot-to-shot variations of $p_0$ result in well-characterized changes of the interferometric quantity $A$. Additionally, at this particular time separation $\delta t$ and TOF time, for $-0.3p_{\rm r} < p_0 < 0.3p_{\rm r}$, the values of $A$ are unique to specific values of $p_0$. This means that the analysis could be done in reverse: an experimental value of

$A$ could be matched to a value of $p_0$ from the simulation. In this way, the interference pattern could be used to measure $p_0$, or any other perturbation that can be simulated.

### 3.3.3 Large-Separation Atom Interferometer

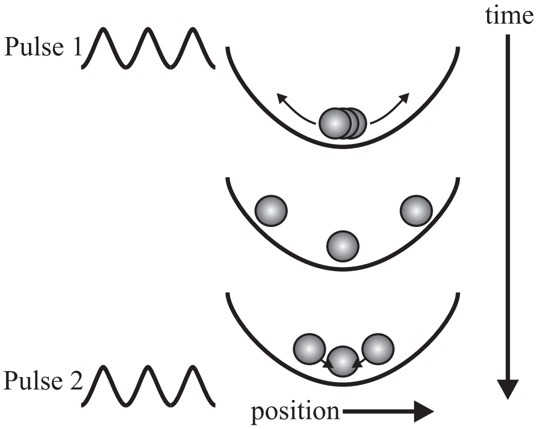

Figure 3.12: Schematic of the large-separation atom interferometry method, represented in position space. This method can be used to realize a large-separation atom interferometer.

The second interferometry scheme demonstrated in this thesis differs from the first in that $\Delta t$ is more than an order of magnitude larger: $\sim$8 ms. This allows the non-zero momentum components produced by the first KD scattering pulse to complete a half-oscillation in the magnetic trap and return approximately to their initial positions near the center of the trap by the time the second KD scattering pulse is applied. This procedure, a schematic of which is shown in Fig. 3.12, is a realization of a Mach-Zehnder interferometer, and is very similar to the interferometer described at the end of the section about the BRAC, except that it uses KD scattering instead of Bragg scattering. We were only able to see clear interference on this timescale using BECs. Under our experimental conditions, the +1 and -1 BEC components (starting with momenta of about $+2p_r$ and $-2p_r$, respectively) are, at the farthest point, 60 $\mu$m apart, which is much larger than the BEC size. This is far enough apart that it would be possible to manipulate the atoms traveling in one arm of the interferometer without affecting the atoms in the other; for example, a distance of 60 $\mu$m can be resolved using laser beams. The sensitivity of an atom interferometer to accelerations and fields is proportional to $\Delta t$. While a few other groups have achieved larger $\Delta t$ (see, for example, Refs. [61] and [62]), 8 ms is still one of the larger time separations [63].

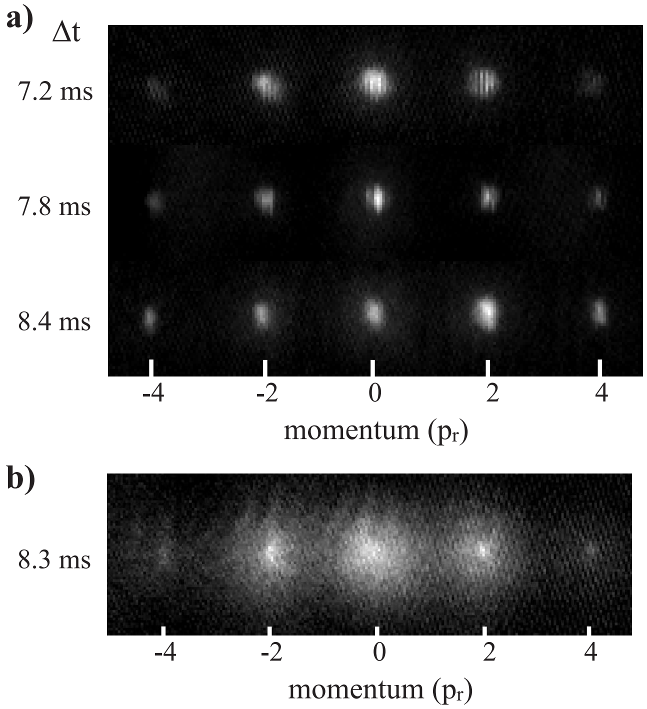

Figure 3.13: Large-separation atom interferometer. After undergoing a half-period oscillation in the magnetic trap: (a) BEC interference can clearly be seen for various $\Delta t$; (b) a thermal cloud shows weak interference ($\Delta t = 8.3$ ms).

The images shown in Fig. 3.13, taken as described above, demonstrate that our large-separation interferometer produces interference fringes after a half round-trip of the atoms in the magnetic potential (for the case depicted in Fig. 3.13, the frequency of the trap along the axis of the lattice is 60 Hz). The contrast of these fringes varies considerably from shot to shot, ranging from 20% to 75%. In the large-separation interferometer, the fringe period is no longer described by Eq. 3.12 because the condition $\omega\Delta t \ll 1$ does not hold. At $\Delta t = 8.4$ ms, very close to a half-oscillation in the magnetic trap, $\lambda_{\mathrm{f}}$ is larger than a BEC component, and interference is observed indirectly as a difference in atom number between the components emerging with $\pm 2p_r$, as described above for the other interferometry scheme. As seen in the figure, the +1 component has a larger population than the -1 component. At 7.2 ms and 7.8 ms, $\lambda_{\mathrm{f}}$ is small enough that multiple fringes can be seen in each BEC component. The presence of multiple fringes theoretically allows for more sensitive measurement, in that small changes in the phase of the fringes can be observed, rather than the less precise measurement of the number of atoms in each component. In order to exploit this potentially higher sensitivity, however, it would be necessary for the imaging system to be able to resolve small phase changes, which is not the case in our present setup.

While our spatial and temporal separations are not as large as those in the experiment of O. Garcia *et al.* (who hold the record for a BEC interferometer with the arms completely spatially separate [61]), our system provides some advantages over theirs. One advantage is that we can make $\lambda_{\mathrm{f}}$ small enough to see individual fringes by making $\Delta t$ not exactly equal to half an oscillation period in the magnetic trap. As mentioned above, this allows for potentially more precise measurements, even if we are not capable of taking advantage of that in our system. Another advantage is that we use the curvature of our magnetic trap as the "mirrors" at the end of each arm of the Mach-Zehnder interferometer. This is both easier to implement and more reproducible than using a Bragg-scattering pulse. A Bragg-scattering pulse can lose its efficiency if the BEC starts with a small unknown momentum, as is the case for both our experiment (and is why the attempt with the BRAC setup failed) and for the experiment described in Ref. [61]. A small momentum has no effect on the efficiency of a KD pulse. Additionally, KD scattering provides advantages over Bragg scattering for interferometers where the arms are separate for only a short period of time. Bragg-scattering pulses are much longer than KD scattering pulses, and in many cases may take up a sizable portion of the separation time (for example, [60]). Past experiments performed on atomic beams used KD scattering pulses to create interferometers; however they used KD scattering to reflect the beams as well as to split and recombine them. Because of this, a significant proportion of their sample was scattered to high orders, and the resulting fringes had only 10% contrast [64].

Based on the periodicity of the propagator of the one-dimensional harmonic oscillator, for given $\Delta t_0$ and integer $n$ one would expect to find the same shadow images for all values $\Delta t = \Delta t_0 + n\pi/\omega$. Thus, based on observations of thermal-cloud interference at some short time delay, $\Delta t_0 \lesssim 500\ \mu$s, as in Fig. 3.10, one might expect to find similar interference patterns of thermal clouds at much longer delay times, $\Delta t = \Delta t_0 + n\pi/\omega$. We do, indeed, observe that cold thermal clouds produce some interference after a half round-trip, as demonstrated in Fig. 3.13 (b). Nonetheless, the thermal-cloud interference observed after a half round-trip is considerably less pronounced than after short time delays, $\Delta t \lesssim 500\ \mu$s. The observed fringe contrast is 35% along the top edge of the shadow image, while it drops to zero near the center line and below. There are multiple causes that can explain the discrepancy between this observation and the high-contrast fringes observed for a BEC after the same time delay. The motion of the atoms in the trap may not be exactly one-dimensional. If the lattice laser is not perfectly aligned with one of the principal axes of the trap, the components gain a small momentum along a transverse axis of the trap. In this case, the interference planes in 3-D space may tilt after a large $\Delta t$ due to differences in trap frequency along the different axes of the trap. This would cause the interference to average out in the shadow images, which are 2-D projections of the atom density.

This is also the probable cause of the noticeable tilting of the fringes in Fig. 3.13 (b). Additionally, any anharmonicity of the trap potential would break the periodicity of the propagator, leading to a reduction of the coherence time of cold thermal samples. (The expected ability to see exactly the same thing after successive periods of oscillation is, after all, unique to the special case of a perfect harmonic oscillator. This is not an issue with a BEC, which has a long intrinsic coherence time.)

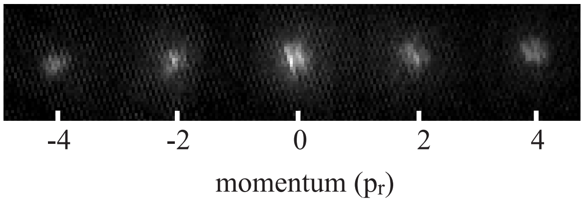

Figure 3.14: Interference after a full-period oscillation. $\Delta t = 16.5$ ms.

Finally, as an extension of the previous scheme, we demonstrate that interference can be seen when the ±1 components are allowed to undergo a full oscillation. This is shown for a BEC in Fig. 3.14, where $\Delta t = 16.5$ ms. In this case, the fringes appear tilted; this is presumably because the lattice laser is not perfectly aligned with the axes of the trap, as explained above. The full-oscillation version of the large-separation interferometer has both advantages and disadvantages over the half-oscillation version presented above. Having both components go through all the same space over the course of their separation negates any phase difference a component might pick up due to asymmetries in the trap. Time-independent, spatially-dependent fields and linear accelerations would affect both components equally, since they each sweep out the same spatial range. Each component is separately addressable only if the duration of the perturbation under investigation is timed such that it affects one component when it reaches one end of the trap but is no longer present by the time the other component reaches that location. This is actually the best potential application for this sort of interferometer: any constant-in-time trap perturbations would be negated by both arms sweeping out the same spatial range, but any perturbations that vary in both time and space (realistically, someone briefly turning on a laser beam to intentionally achieve this affect; more interestingly, a particle flying through the edge of the trap) would affect the two arms differently. Furthermore, when the ±1 components collide at the center of the trap after half an oscillation, atom loss and four-wave mixing can occur due to s-wave scattering.

## 3.4 Conclusion

We have demonstrated a novel atom cavity using Bragg-reflection and the curvature of the magnetic trap as the cavity mirrors. Although it would theoretically be possible to use this cavity as an atom interferometer, experimental noise prevented us from implementing it [65]. We have, however, implemented two atom interferometers using Kaptiza-Dirac scattering: a small-separation interferometer and a large-separation interferometer. We have demonstrated that it is feasible to use the small-separation interferometer for measurements. The large-separation interferometer, meanwhile, allows for separately addressable interferometric arms [66]. We have additionally demonstrated and characterized a lattice-depth calibration method based on Kaptiza-Dirac scattering [67].

# CHAPTER IV

## Loss and Return of Superfluidity: a 1-D Mott Insulator?

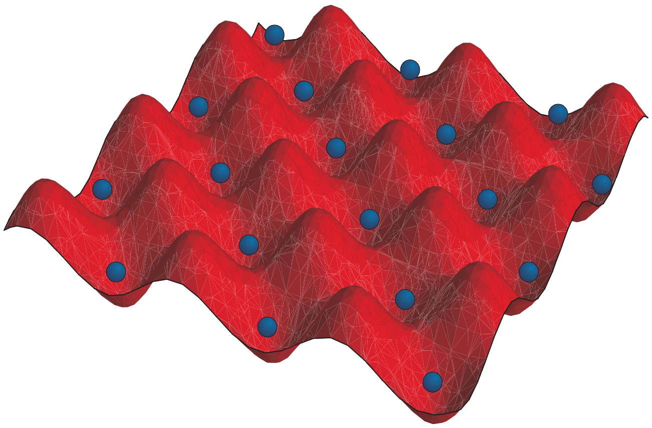

Figure 4.1: A Mott insulator, with one atom per lattice well.

Attaining the Mott insulator transition requires a deep lattice, commonly achieved by high laser power and narrowly focused beams. Demonstrating the transition from a BEC to a 1-D Mott insulator (a 3-D BEC in a 1-D lattice formed by two laser beams) is more difficult because a deeper lattice is needed [68, 69]. Furthermore, characterizing the transition requires an accurate determination of the lattice depth. In this chapter, we investigate the reversible loss of superfluidity of a 3-D BEC in a 1-D lattice. While other experiments have examined the Mott insulator transition using low dimension Bose gases [35–37], we use a 3-D BEC, applying no transverse lattice potential to reduce the dimensionality of our BEC. Our observations are consistent with a transition to a 1-D Mott insulator.

## 4.1 Experimental Observations

In this experiment, far more than the ones described in Chapter III, it is important to know the exact depth of our optical lattice at all times, since the phenomenon we are looking for is dependent on the lattice depth. We carefully calibrate the lattice depth using KD scattering, as described in Chapter III. We also control for the curvature of the trap by repeating the experiment at two different trap frequencies, 80 Hz and 200 Hz (in the direction of the lattice). The BEC is allowed to expand freely for TOFs of 16 ms or 12 ms, for the case of the 80 Hz or 200 Hz traps (after varying amounts of decompression), respectively. Since the BEC temperature depends on the trap frequency, different trap frequencies require different TOFs to produce the best image.

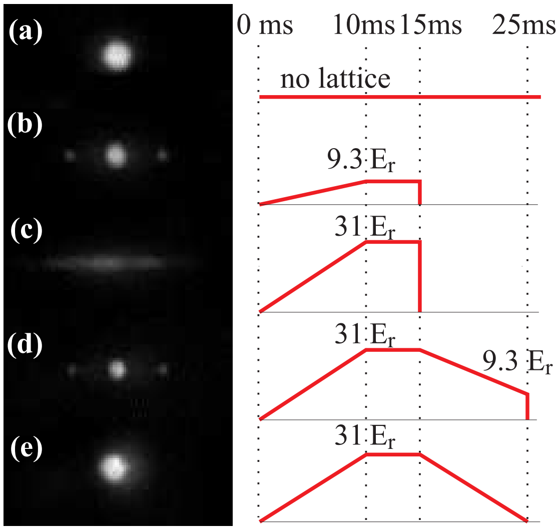

Figure 4.2: Left: TOF images. Right: lattice depth as a function of time for (a) BEC with no lattice, (b) modulated superfluid in a weak lattice, (c) loss of superfluidity in a deep lattice, (d) modulated superfluidity recovered after the deep lattice is ramped down, and (e) BEC with no lattice, recovered after the deep lattice is ramped down.

With the lattice depth carefully calibrated, we investigate the loss of well-to-well phase coherence of the BEC when the optical lattice is turned on slowly. We use the amplitude modulation of an acousto-optic modulator to control the power of the lattice beams. We ramp up the power of the lattice beam from zero to its final value over 10 ms, and then hold it there for 5 ms. Then, we simultaneously turn off the lattice and the magnetic trap, and take a TOF measurement. As can be seen in Fig. 4.2 (b), for small lattice depths the BEC is only slightly modulated by the lattice, corresponding to the appearance of only two weak side peaks, at $\pm 2\hbar k_{\mathrm{L}}$. Although the side peaks have the same momentum as the first-order peaks of KD scattering, this is an unrelated phenomenon: these momentum peaks appear during TOF and are due to the (approximately steady-state) spatial modulation of the BEC. As the depth of the lattice is increased, well-to-well phase coherence is lost. As a result, the side peaks disappear and the central peak broadens, reflecting the momentum distribution of the localized wavefunction in a single lattice well. We associate the loss of well-to-well phase coherence with a loss of superfluidity. Here, we find that the superfluidity is largely lost for lattices deeper than about 30 $E_{\mathrm{r}}$.

The loss of superfluidity in our system is fully reversible. To demonstrate this, we ramp the lattice to 31 $E_{\mathrm{r}}$ over 10 ms, hold it there for 5 ms, and then ramp back down over 10 ms. As can be seen in Figs. 4.2 (d) and (e), we obtain a modulated superfluid and BEC when we ramp down to a weak lattice and no lattice, respectively. The BEC does not appear to have residual momentum components at multiples of $2\hbar k_{\mathrm{L}}$ after the lattice is ramped down.

In lattices deeper than about 30 $E_{\mathrm{r}}$, the BEC can be thought of as a stack of phase-uncorrelated pancake BECs. As can be seen in Fig. 4.2 (c), the atoms expand much farther in the direction of the lattice than in the transverse direction. This is largely due to the momentum spread of the pancake BECs in the lattice-beam direction. Examining the TOF image in Fig. 4.2 (c), we find a velocity spread of $\Delta p/m_{\mathrm{Rb}} = 8$ mm/s. Using the Heisenberg uncertainty relation, $\Delta y \Delta p \geq \hbar/2$, this corresponds to a localization $\Delta y = 46$ nm, or 11% of the lattice period. Neglecting mean-field effects and using the fact that the lattice wells are approximately harmonic near their minima, we find an oscillation frequency of $2\pi \times 35$ kHz for a lattice with a depth of 30 $E_{\mathrm{r}}$, and velocity and position uncertainties of 8.9 mm/s and 41 nm, respectively, for the ground state. These numbers match the values derived from Fig. 4.2 (c) quite well, showing that the expansion in the lattice-beam direction is mostly driven by the kinetic energy of the pancake BECs in the optical-lattice wells.

A more subtle effect is that in the case of a deep lattice the expansion transverse to the lattice-beam direction is considerably slower than in the lattice-free BEC: about 1.5 mm/s and 2.5 mm/s, respectively. We attribute the difference to a variation in the manifestation of the repulsive mean-field potential (estimated to be $\lesssim 1$ kHz for our BECs in 200 Hz magnetic traps). Without the lattice, the BEC expansion is driven by a combination of the mean-field pressure and the kinetic energy of the BEC in the magnetic trap, leading to a final expansion speed of about 2.5 mm/s in all directions in Fig. 4.2 (a). After application of the deep lattice in Fig. 4.2 (c), the expansion is mostly driven by the comparatively high kinetic energy of the BEC pancakes in the optical-lattice wells, leading to a much faster expansion in the lattice direction. The faster expansion leads to a reduction of the time over which a substantial mean-field pressure exists, leading to a reduced final expansion speed transverse to the lattice, as observed.

To quantitatively characterize the loss of superfluidity, we examine TOF images as a function of lattice depth. We use the visibility of the side peaks, $v$, to map out

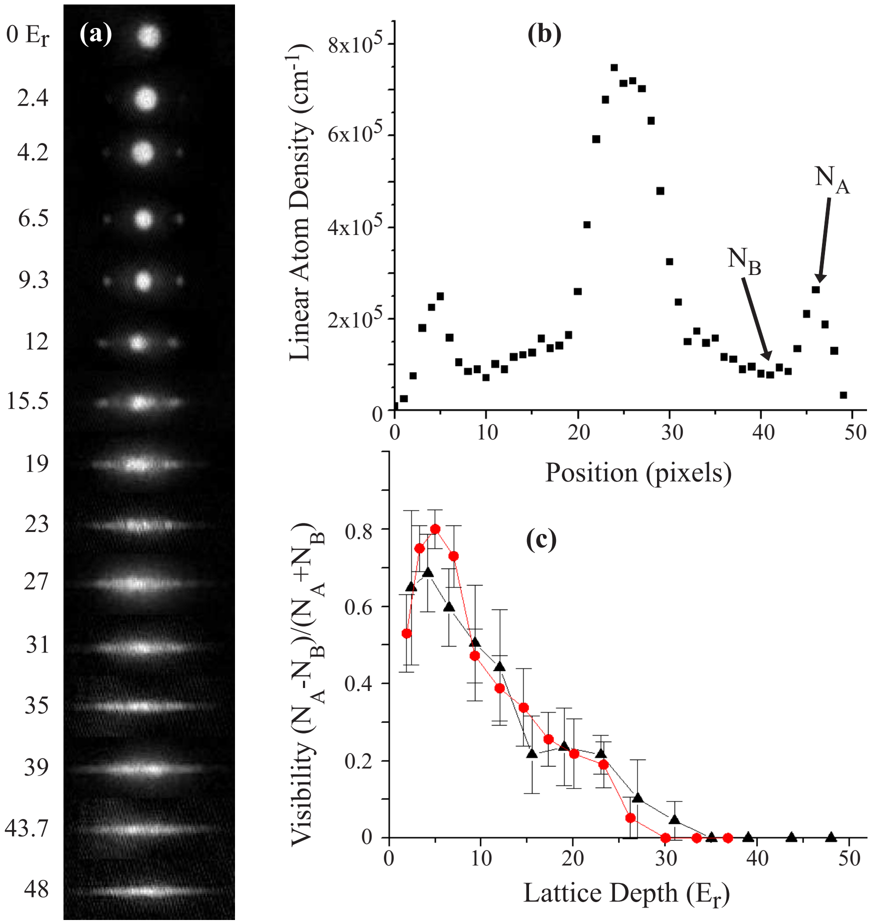

Figure 4.3: (a) TOF images as a function of lattice depth for a 200 Hz magnetic trap. (b) Linear atom density distribution for a BEC after 12 ms TOF, released from a lattice with a depth of 9.3 $E_\mathrm{r}$ and magnetic trap with 200 Hz frequency. $N_A$ is the height of the side peak and $N_B$ is the height of the valley. (c) Visibility as a function of lattice depth from a 80 Hz magnetic trap (circles) and a 200 Hz trap (triangles).

the transition:

$$v = \frac{N_\mathrm{A} - N_\mathrm{B}}{N_\mathrm{A} + N_\mathrm{B}} \tag{4.1}$$

where $N_\mathrm{A}$ is the linear atom density of one side peak, and $N_\mathrm{B}$ is the linear atom density at the minimum between the center peak and the side peak. The timing of the lattice application is as described above. Examining the resulting TOF images, shown in Fig. 4.3 (a), we take the linear atom density as a function of position in the lattice direction along the central strip of each image, integrating over three pixels in height (a pixel in the image corresponds to 6.7 $\mu$m). For $N_A$, we choose the local maximum at the side peak, if there is one, and for $N_B$ we choose the local minimum between the side peak and the central peak, as shown in the sample data in Fig. 4.3 (b). If there is no local side maximum, we designate $v = 0$. We calculate the visibility separately for the side peaks on the left and right, and repeat the calculation for five separate images at each lattice depth. We then average the ten resulting values to get the visibility plotted in Fig. 4.3 (c). As can be seen, the BEC starts to lose superfluidity around 10 $E_\mathrm{r}$, where $v$ first reaches a value lower than its initial value. The BEC has fully lost its superfluidity by 30 $E_\mathrm{r}$, where $v = 0$. The loss of superfluidity happens under the same lattice conditions in the 80 Hz trap and the 200 Hz trap, as can be seen by comparing the circles and triangles in Fig. 4.3 (c). This indicates that at both 80 Hz and 200 Hz the trap has no noticeable effect compared to the lattice.

Ideally, the visibility should be unity as long as the system is fully in a superfluid state [70]. In the experiment, however, even a minute thermal background will lower the visibility, and will disproportionately affect images with lower $N_A$. As $N_A$, $N_B \to 0$, this will prevent the visibility in Eq. 4.1 from reaching unity. For these reasons, the first few data points in Fig. 4.3 (c) not only fail to approach unity, but are even lower than visibilities seen for lattice depths $\sim 5$ $E_\mathrm{r}$. We are confident, however, that these issues do not affect our determination of where the loss of superfluidity occurs, because the transition happens at a lattice depth where both $N_A$ and $N_B$ are large.

The drop in visibility that is used as an indicator for the reversible loss of well-to-well phase coherence and superfluidity of the BEC (see Fig. 4.3) does not always appear instantaneously; it can sometimes take an observable amount of time to develop. To study the dynamics of the dephasing, we ramp the lattice to its final

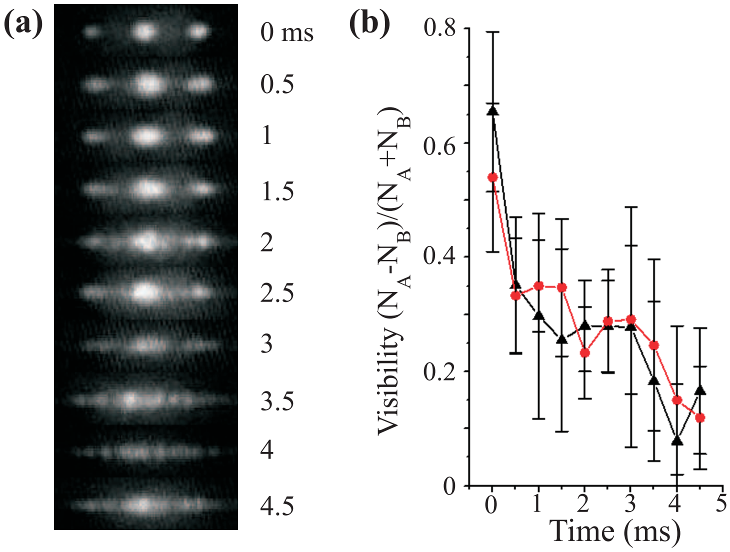

Figure 4.4: (a) TOF images as a function of holding time in a lattice of 23 $E_\mathrm{r}$ depth in a 200 Hz magnetic trap. (b) Visibility as a function of holding time of the lattice, for an 80 Hz magnetic trap (circles) and a 200 Hz trap (triangles).

depth over 10 ms, leave the lattice on for a variable hold time, and take TOF images as a function of the hold time, as shown in Fig. 4.4 (a) for the case of a final depth of 23 $E_\mathrm{r}$. The visibilities in Fig. 4.4 (b) are obtained as described earlier. When the lattice is ramped to final depths less than about 10 $E_\mathrm{r}$, the BEC simply remains superfluid, permanently maintaining a global phase across the individual lattice wells. If the final lattice depth is larger than about 30 $E_\mathrm{r}$, at the end of the lattice ramp the BEC immediately shows the signatures of a complete loss of superfluidity. Thus, in this case the breakup of the BEC into dephased pancake BECs in the individual lattice wells is already complete by the end of the ramp, and there are no detectable dynamics after completion of the ramp. In contrast, if the BEC is loaded into a moderately deep lattice (of order 20 $E_\mathrm{r}$), it takes a measurable amount of time for the pancake BECs to dephase with respect to each other and for the signatures of the loss of superfluidity to appear. For the parameters in Fig. 4.4 it is found that the dephasing takes of order three milliseconds.

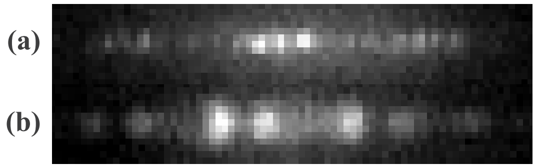

Figure 4.5: TOF images in a deep lattice and in magnetic traps with frequencies (a) 80 Hz and (b) 200 Hz. The speckles vary from shot to shot, and are due to interference during TOF of pancake BECs from different lattice wells.

In many of the images where the BEC is in a deep lattice, irregular bright and dark vertical stripes appear. These stripes can be seen in nearly all of the images after the loss of superfluidity from the 80 Hz trap, and in several, but not all, of those images from the 200 Hz trap. For example, in Fig. 4.3 (a), the stripes are visible in the images at 23 and 35 $E_{\mathrm{r}}$. The arrangement of the stripes appears random, with no repetition of the pattern from image to image, but the characteristic size of the stripes remains the same for a given magnetic trap frequency. We believe that these stripes represent interference between pancake BECs from different lattice wells during TOF. After the loss of superfluidity, each pancake BEC still has a definite, but random phase. During TOF, the pancakes all expand into each other, leading to a characteristic interference speckle size. In Fig. 4.5 we show interference patterns in TOF images for the two different magnetic trap depths. To find the characteristic speckle size, $\Delta s$, in these images, we take fast Fourier transforms (FFT) of five images and average them for each trap depth. The value of $\Delta s$ is given by the inverse spatial frequency where the FFT signal reaches the noise floor. We find $\Delta s = 17$ $\mu$m for the 80 Hz trap and 27 $\mu$m for the 200 Hz trap. Using a straightforward analysis, we estimate that the number of interfering pancakes, $P$, is related to $\Delta s$ and the time-of-flight, $T$, via $P = 2hT/(m\,\Delta s\,\lambda)$. From this we find $P = 20$ and 10 pancakes for the 80 Hz and 200 Hz traps, respectively. These numbers agree reasonably well with our measurements of the size of the BEC in the respective magnetic traps.

## 4.2 Discussion

The most obvious interpretation of the results presented above is that when the BEC loses its superfluidity it is undergoing a transition into a 1-D Mott insulator state. In the 3-D case, number squeezing can be directly measured by looking for discrete regions with different number states, as was done in Ref. [27]. In our case, however, number squeezing would be impossible to measure directly. This can be illustrated by imagining an ellipsoid cut into 10-20 slices of equal width. Each slice is guaranteed to have a different volume; even if, by luck, the ellipsoid is sliced perfectly such that two slices have the same volume, no more than two will be the same. The same is true with the BEC in the lattice: it is an ellipsoid cut into several pieces, and no two pieces are the same. Thus, it is impossible to measure ”regions” with the same number of atoms, because each lattice well is its own region. Furthermore, BEC experiments are not so precise as to produce BECs of exactly the same size in each run, rendering impossible any statistical experiments looking for exact consistency in atom number. Therefore, we look for indirect signatures of a Mott insulator transition. The typical signature of a Mott-insulator transition in 3-D is that the side peaks disappear and the central peak broadens, reflecting the momentum distribution of the localized wavefunction in a single lattice well [26]. Our system, as seen in Figs. 4.2 (a)-(c), follows this progression, with an appearance very similar to that of the 3-D Mott transition observed in Refs. [26] and [34]. Furthermore, the Mott insulator transition is a quantum phase transition, and thus is reversible. As seen in Figs. 4.2 (d) and (e), the loss of superfluidity in our system is also fully reversible. This indicates that the loss of superfluidity is not due to a lattice-induced heating effect, providing support to the Mott-insulator explanation of the observed phenomenon.

We observe a complete loss of superfluidity at 30 $E_\mathrm{r}$. Our system contrasts strongly with that of a 1-D Bose gas in a 1-D lattice, where the Mott transition is complete around 10 $E_\mathrm{r}$ [37]. For a 3-D Bose gas in a 3-D lattice, the Mott transition is complete around 20 $E_\mathrm{r}$ [26]. Our observations are in general accordance with the prediction in Ref. [68] that for a 3-D Bose gas in a 1-D lattice the Mott transition requires a deeper lattice than in the case of a 3-D Bose gas in a 3-D lattice. The specifics do not match, however, in that the lattice depth predicted in Ref. [68] necessary for the Mott transition is upwards of 50 $E_\mathrm{r}$ for a system like ours with about 3000 atoms per lattice well.

One concern in the interpretation of our results is adiabaticity. The transition from a superfluid to a Mott insulator should require an adiabatic ramp of the optical lattice, where adiabaticity is related to the time scale of the lattice ramp with respect to the tunneling time of the atoms in the lattice and the energy gap of the insulator. There does not seem to be a strict requirement, however; experiments demonstrating the transition to a 3-D Mott insulator have shown that the system only needs to be approximately adiabatic to achieve the transition. In Ref. [71] it is observed, for example, that full adiabaticity for a 3-D Mott transition requires a ramp time of 100 ms, while in Ref. [34] it is observed that the Mott transition is achievable for any ramp time larger than 1 ms. Since different lattice depths are required for the 1-D Mott transition than for the 3-D Mott transition, a direct comparsion of times cannot be made. Rather, we compare our experiment to superficially similar experiments done using 1-D lattices. Hadzibabic *et al.*, in Ref. [72], perform experiments on a BEC in a 1-D optical lattice where they ramp their lattice approximately forty times faster than we ramp ours (when measured on a time scale given by the tunneling time); after 10 ms, they have a tunneling time of 7 s, compared to ours of 160 ms. They observe regular interference between the pancake BECs in the different lattice wells. In contrast, we observe random speckle patterns. Furthermore, this random speckle pattern is consistent with the absence of definite phases in a Mott insulating state. Orzel *et al.*, in Ref. [73], meanwhile, find that if the lattice potential is turned on too quickly, the BEC permanently loses superfluidity, even if the lattice potential is slowly ramped back down. We observe a complete return of superfluidity in our system.

Reference [74] presents an alternate explanation for our results. McKagan *et al.* simulate a BEC in a 1-D optical lattice using the Gross-Pitaevskii equation. Thus, their analysis does not consider number-squeezing, which is a necessary part of the description of a Mott insulator. Nonetheless, they find that they can simulate a reversible loss of phase coherence. Their results, which they attribute to mean-field effects and a lack of complete adiabaticity, mimic the expected signatures of a 1-D Mott insulator. Interestingly, they observe in their simulations that the deepest lattices should produce TOF results resembling our random speckle pattern.

There is little that can be used to distinguish between the two possible interpretations. Qualitatively, the expected signatures of the Mott transition and a mean-field effect in a non-adiabatic lattice ramp are the same. Reference [74] observes, for the case of the mean-field effect, that the visibility of the side peaks should oscillate as a function of lattice depth, unlike the monotonic decrease to $v = 0$ expected for a Mott transition. We do not observe any such oscillations. However, Ref. [74] suggests that these oscillations might not be observable experimentally; rather, they might manifest as heating. We do observe some slight heating when the lattice is ramped up to $30E_{\text{rec}}$ and back down: the thermal halo around the BEC is larger in Fig. 4.2 (e), after the lattice ramp, than in Fig. 4.2 (a), before it. McKagan *et al.* further hypothesize that the presence of number squeezing (insufficient for a true Mott transition) could damp the oscillations. Thus, the observed lack of oscillations in the visibility function does not allow us to distinguish between a Mott transition and a mean-field effect in a non-adiabatic lattice ramp.

## 4.3 Conclusion

In conclusion, we have investigated the reversible loss of superfluidity of a BEC when a deep 1-D optical lattice is applied. We used Kapitza-Dirac scattering as an accurate way to calibrate our lattice depth. We examined time-of-flight images of the BEC as a function of lattice depth, and found that the BEC fully loses its superfluidity at about 30 $E_{\mathrm{r}}$, and may require a certain time to dephase. Furthermore, we observed random interference patterns in time-of-flight images. Our results are consistent with at least two explanations: most prominently a phase transition from a BEC to a 1-D Mott insulator, but also a mean-field effect in a deep lattice [67].

## CHAPTER V

# The Ion-BEC Apparatus

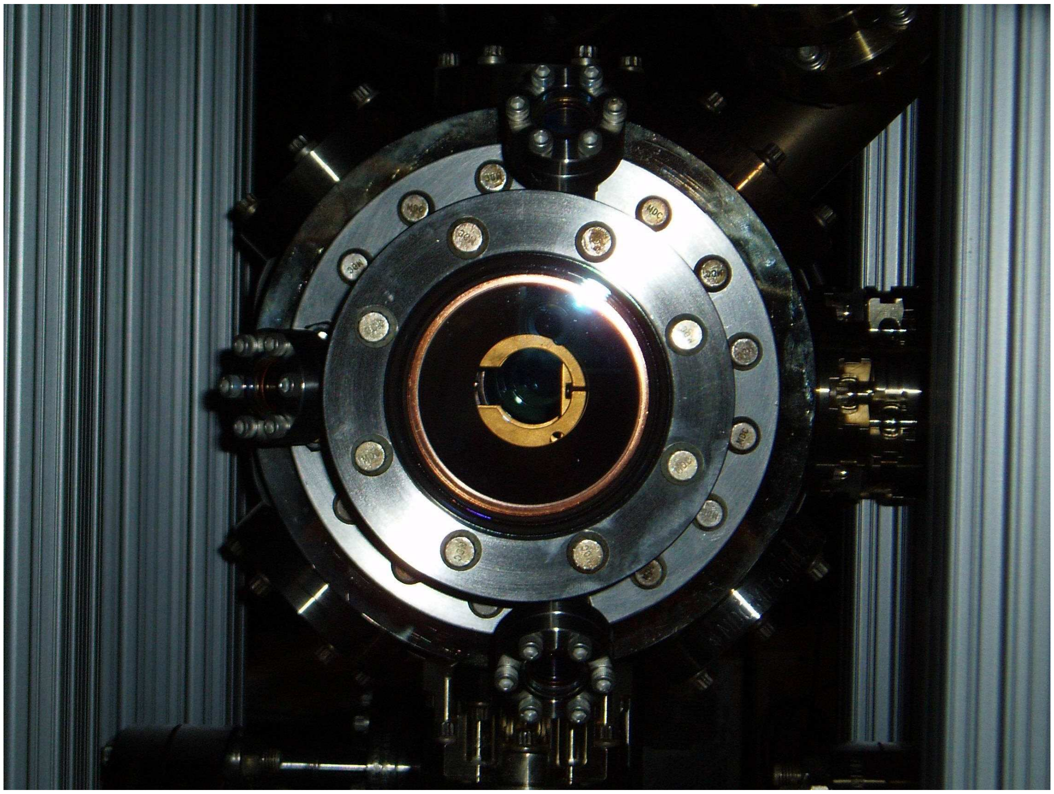

Figure 5.1: The new BEC vacuum chamber, with modifications to minimize stray electric fields (this photo was taken before the MCP was attached).

The vacuum chamber used in our earlier experiments was originally designed with only a BEC in mind. Modifying it to accommodate both a BEC and an ion (or multiple ions) opens up a whole range of new experiments to investigate unexplored phenomena. As of the writing of this thesis, there is no apparatus in the world other than this one that is built to accommodate both a BEC and an untrapped ion; there are two new setups at other universities made for a BEC and a trapped ion, but they are sufficiently recent as to have no published results. We have chosen to use untrapped ions in our experiment because the micro-motion of an ion in a conventional ion trap could conceivably stir up the BEC, heating it to a point where it would be destroyed. Additionally, if the ions are untrapped, we are not limited to species of ions that can easily be trapped. Instead, using 780 nm and 480 nm light, we can photoionize BEC atoms with a two-photon transition. If we tune the lasers to just beyond the ionization threshold, the ions should be only barely heated above BEC temperature. With weak enough photoionization pulses, on average only a single BEC atom should be ionized. In order to accommodate ions, extensive modifications must be made to a BEC chamber: an untrapped ion requires a Faraday cage to minimize the electric fields surrounding it and a means for detection. In this chapter, I will discuss these modifications of the BEC chamber.

## 5.1 Getting a bigger BEC

In the experiments described over the previous few chapters, the BEC tended to have ∼80,000 atoms. Even under optimal conditions, with a 15 s MOT loading time and a 16 s evaporative cooling ramp, we never created BECs with more than 125,000 atoms, and rarely created BECs with more than 100,000 atoms. Although these BECs were sufficient for all of the lattice experiments described in Chapters III and IV, there were situations where the experiment may have benefited from having more atoms. For example, in the small-separation interferometry experiment in Chapter III, if we had started with more atoms, we could have varied the number of atoms in the BECs by a larger amount and in doing so tested mean-field effects on the phase of the interferometric fringes. Since we were already dismantling the experiment to make modifications to accommodate ions, this provided a good opportunity to make improvements to the process of making a BEC.

### 5.1.1 A New Pyramidal MOT

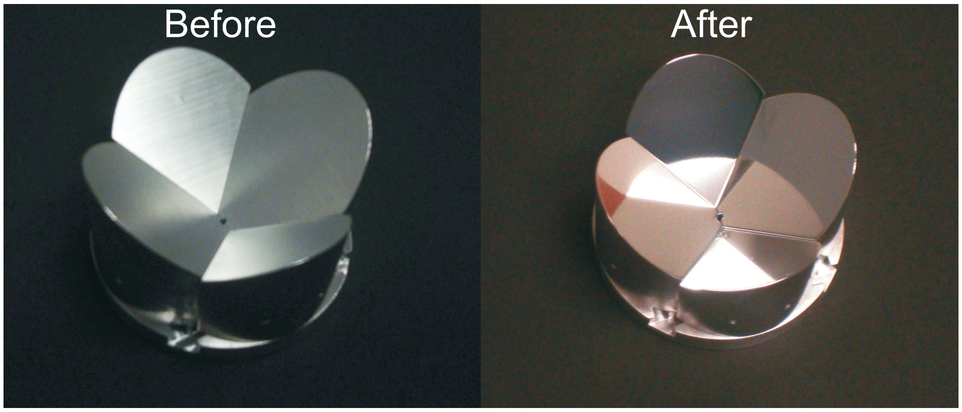

Figure 5.2: The new pyramid, made of solid blocks of aluminum, before and after being hand-polished to a mirror finish.

Starting from the very beginning of the process to make a BEC, I have improved upon the pyramidal MOT. The old pyramid was composed of four glass slides, carefully cut and shaped, and glued together, with a thin layer of aluminum (<100 nm thick) deposited on the inner surface using an evaporator. This construction process is prone to imperfections in the shape of the glass pieces and the angles at which they are glued together as well as in the shape and size of the exit hole at the apex of the pyramid; however, in the case of our pyramid these imperfections were probably minor and had little effect on the MOT. A more severe problem is that the aluminum evaporated onto the glass partially oxidized. This may have been due to impurities in the aluminum source, or insufficiently clean vacuum in the bell jar of the evaporator. Whatever the cause, the oxidation worsened with every exposure to air, each time the vacuum chamber was opened. By the time we made our first BEC, the aluminum was noticeably cloudy, and by the time we were ready to modify the chamber for ions the pyramid was a dull grayish-white.

The new pyramid fixes all of these problems. It is composed of four precision-machined aluminum blocks, which I designed to interlock with an aluminum base to form the pyramid, shown in Fig. 5.2. By using machined pieces, any imperfections in the angle of the mirror faces can be avoided, the gaps between the faces can be minimized, and there is no glue that might leak onto the mirror face. Furthermore, the exit hole, having been drilled through metal, is guaranteed to be circular. The exit hole has a diameter of 1.5 mm, which is smaller than the length but larger than the width of the hole in the old pyramid. I polished the aluminum blocks to an optical-quality mirror finish with 0.5 $\mu$m diamond grit. The metal blocks are considerably less likely to oxidize than the thin aluminum coating of the old pyramid.

Although it is difficult to directly measure the size of the pyramidal MOT, we can see improvement in the secondary MOT. Due to the shape of the new chamber, we are unable to wrap diagonal coils for the external MOT in the near-perfect anti-Helmholtz configuration described in Chapter II. While the old coils were 7 inches in diameter and 4 inches apart, the new coils are 2 inches in diameter and 8 inches apart. This is the only configuration that allows us to physically fit the coils in the new design. However, based on simulations, the primary change to the magnetic field is that in the new configuration it is more spherical, while in the old configuration it was flatter and more pancake-like; we can put sufficient current through the new coils for the gradient to remain approximately the same as it was with the old coils (although we must water cool the new coils to accommodate the increased heat load due to so much current in such a small coil package). It is not clear whether the new external MOT configuration is better or worse than the old one. The combined effect of the new pyramid and the new external MOT coils is a factor of at least 1.5 improvement in the number of atoms in the external MOT; the new external MOT has up to $2 \times 10^8$ atoms after 10 s of loading.

For reasons that will be explained later in this chapter, the upper chamber has been rotated 90° with respect to its old position, such that the $y$-axis is now the axis of gravity (the axes continue to be defined with respect to the U-Z wire, as in Fig. 2.7). Because the U-Z wire is not at the center of the chamber with respect to the $z$-axis, the atomic beam must be tilted slightly to reach the collection region of the secondary MOT (whether that happens to be the external MOT or the U-MOT). When the dividing tube was first installed to separate the primary chamber from the upper chamber, as described in Chapter II, it was misaligned by $\sim$3 mm. This did not matter in the old configuration, because the atomic beam could be tilted slightly so as not to be clipped by the dividing tube, while still reaching the secondary MOT capture region directly above. The misalignment was in the opposite direction from the one in which the beam must be tilted in the new setup, however, and consequently only a small part of the atomic beam could make it through the dividing tube and up to the capture region of the secondary MOT. Thus, in order to achieve a large secondary MOT, the dividing tube has been removed from the new setup. So far, the absence of the tube does not appear to adversely affect the vacuum pressure.

Finally, to eliminate the BEC hopping that plagued the experiments in Chapter III, which was caused by 60 Hz noise on the magnetic field coils, I have added the capability to have an optical dipole trap for the BEC. I have added small windows to the upper chamber, which are anti-reflection-coated for 1064 nm light, and have purchased a 1064 nm fiber laser capable of producing up to 10 W of light.

### 5.1.2 A Larger U-Z Wire

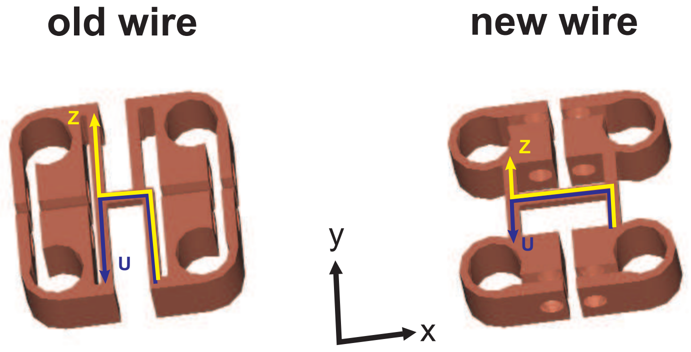

Figure 5.3: Drawings of the U-Z wires for the magnetic traps. On the left is the wire used in Chapters II-IV; on the right is the new, longer wire.

Another inefficiency in the design of the original BEC chamber is the loading between the U-MOT and the Z-trap. This is in part due to the small volume of the Z-trap. The length of the center bar of the wire is a limiting factor in the volume of the Z-trap; on the old Z-wire used in Chapters II-IV, shown in Fig. 5.3 (left), the center bar is 6 mm long. To remedy this problem, I have designed a new U-Z wire with a longer center bar. This new wire is designed to fit on the same feedthroughs used for the old wire, limiting its total size to 1 inch on a side. Additionally, since the legs of the Z-wire serve a function in the 3-D magnetic Z-trap, they could not be eliminated entirely or made too short. With these restrictions in mind, I have designed the new Z-wire with a center bar of 11 mm, shown in Fig. 5.3 (right).

Based on simulations, shown in Fig. 5.4, the Z-trap created by the new U-Z wire is twice as long as the one created by the old wire. Because the legs of the new U-Z wire are shorter than those of the old U-Z wire, smaller $x$-biases are necessary to achieve the same magnetic field magnitude at the minimum of the Z-trap. The simulations suggest that while an $x$-bias field strength of 6-8 G worked well for the old Z-trap (with 50 A of current running through the U-Z wire), a more reasonable

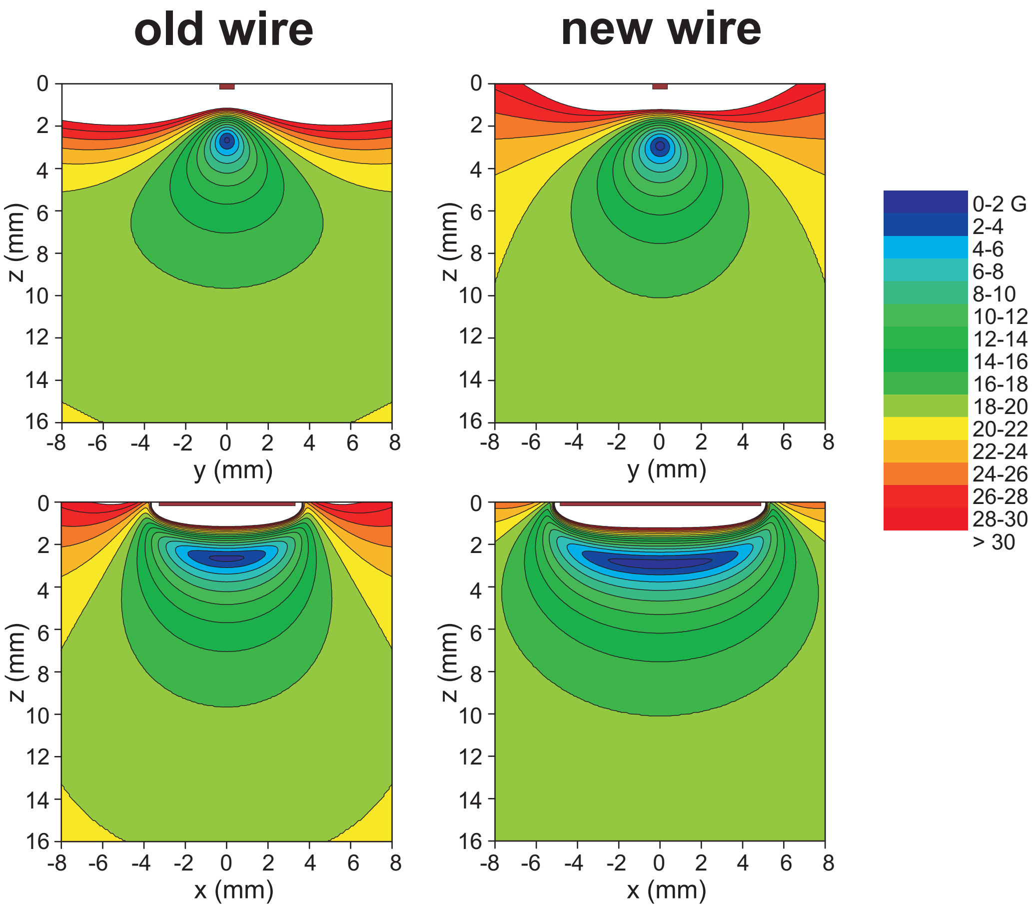

Figure 5.4: Plots of the magnetic fields of the Z-trap with the old and new Z wires at 50 A. The origin is defined to be the center of the wire. All parameters are the same except for the wire length and the $x$-bias; the $x$-biases are 8 G and 3 G, respectively, for the old and new wires, in order to match the magnetic fields at the bottoms of the respective traps.

$x$-bias for the new Z-trap would be 3 G. The effects of the $y$-bias depend primarily on the field due to the center bar and so should be unaffected by changing the U-Z wire. Additionally, because the center bar is longer, the legs tilt the Z-trap less with respect to the $x$-axis; this results in the trap having a more regular, circular shape in the center, as can be seen in the plots of the Z-trap in the $y$-$z$ plane (at $x = 0$) in Fig. 5.4.

The new U-Z wire also allows for a longer U-MOT, as can be seen in Fig. 5.5. Again, the trap is twice as long along the $x$-axis, doubling the capture volume of the MOT. With a larger capture volume, the U-MOT should be able to hold considerably

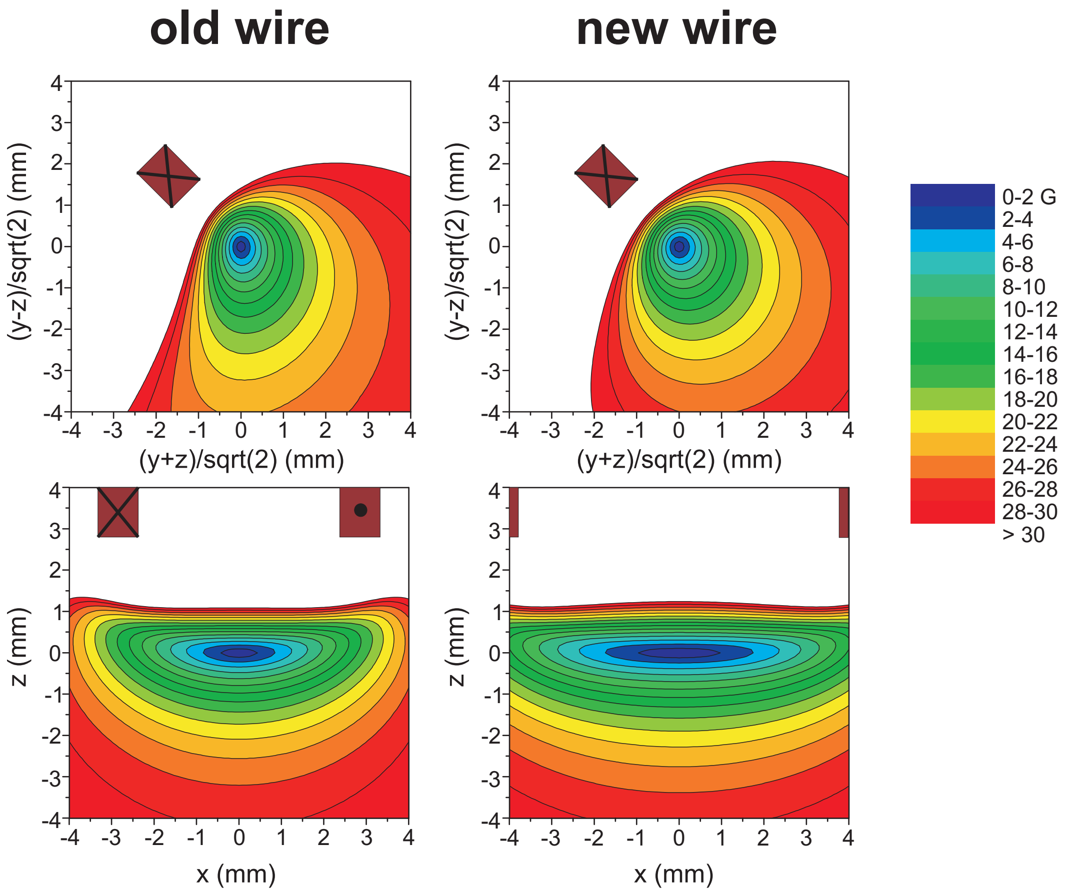

Figure 5.5: Plots of the magnetic fields of the U-MOT with the old and new U wires at 50 A. The origin is defined to be the center of the MOT.

more atoms. Since the external MOT has also been improved, the U-MOT's ability to hold more atoms is especially important. As an added benefit, the cross-section of the MOT in the $y$-$z$ plane becomes more circular at $x = 0$, again due to the legs being farther from the center. With this more regular shape, the new U-MOT magnetic field more closely resembles the ideal MOT quadrupole field; this should improve the efficiency of the U-MOT. Despite all of these improvements, it is still the case that the external MOT can collect more atoms than the U-MOT, so it is still necessary to transfer from the external MOT to the U-MOT rather than loading the U-MOT directly from the cold atomic beam.

## 5.2 Eliminating Stray Electric Fields: The War Between Optical Access and a Faraday Cage

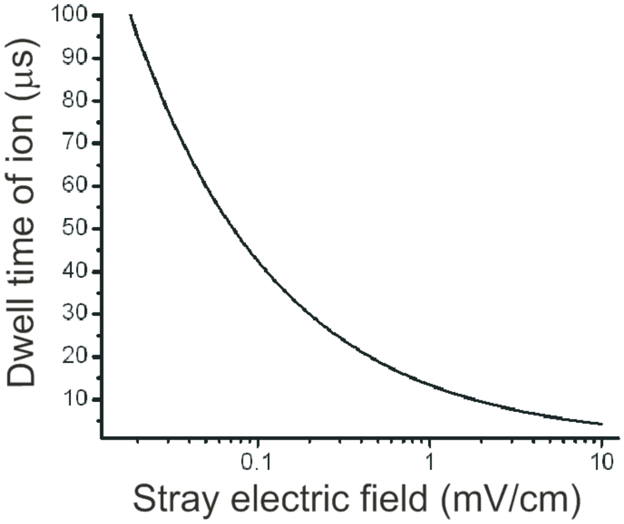

Figure 5.6: Maximum dwell time of an ion in a 10 $\mu$m BEC, as a function of electric field.

An ion is subject to the forces of the electric fields surrounding it. In our case, with no ion trap these electric fields would be uncontrolled, stray fields due to residual charge on any dielectric materials in or near the vacuum chamber. Since the BEC chamber is designed to have as much optical access as possible, to have plenty of room to shine in all of the lasers necessary for creation, manipulation, and imaging of the BEC, there are many glass windows which can accumulate a static charge. This is disastrous for an untrapped ion. Even a very small electric field is sufficient to expel an ion from the vicinity of the BEC in a matter of microseconds, as shown in Fig. 5.6. The plot in Fig. 5.6 shows the amount of time it would take for an ion to move 10 $\mu$m as a function of stray electric field. Since the BEC is 10-20 $\mu$m, this can be taken as the effective maximum dwell time of an ion in a BEC. In order to observe interactions between the ion and the BEC, we need dwell times of at least several tens of microseconds.

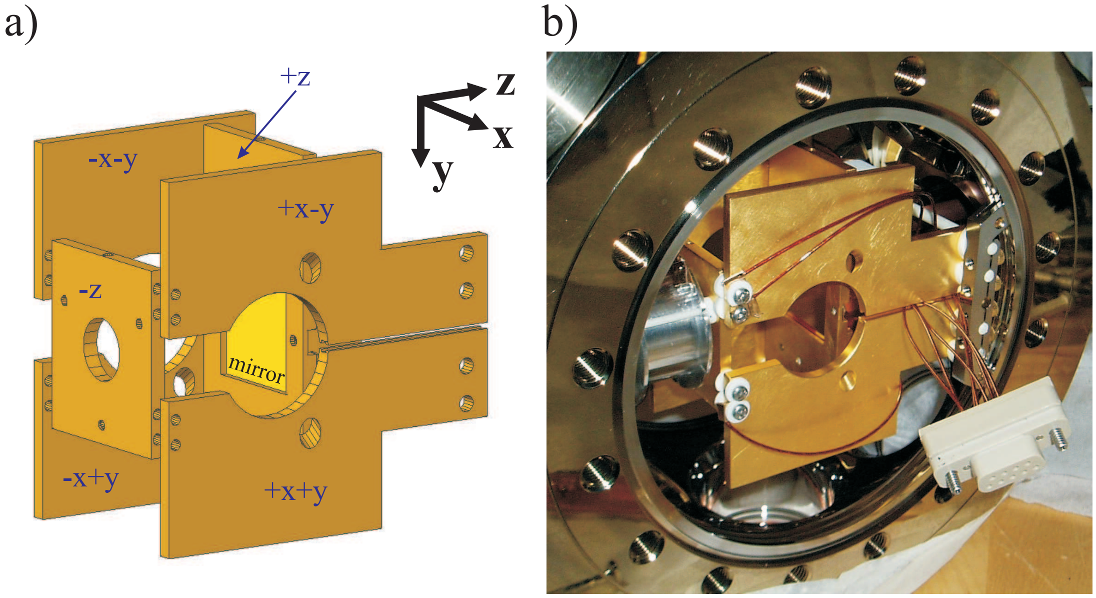

Figure 5.7: (a) The electrodes for controlling the electric field, labeled according to position. (b) The electrode package, assembled and in the vacuum chamber.

To ensure as long a dwell time as possible, we must minimize the electric fields in the vicinity of the BEC. The most reliable way to do this would be to build a Faraday cage around the ion. A true Faraday cage would consist of a solid electrically-conducting shell surrounding the ion. A solid shell would, however, block out all light in addition to shielding against electric fields. This is unacceptable, since a great deal of light is necessary to make the BEC in the first place; without the BEC we have no experiment, no matter how well localized the ion is. A shell made of mesh, rather than solid metal, could let some light through, but a lot of light would be lost to scatter. Since our MOT beams are so bright to begin with, making up for the lost light would stretch the capacity of the lasers, and the scattered light would be a danger to passersby. Additionally the BEC would be very difficult to image, because of both scattered light washing out the picture and shadow lines on the probe beam blocking the image.

I solve this problem by using a system of large plate electrodes rather than a full Faraday cage, as shown in Fig. 5.7. There are six electrodes to control the electric fields of each axis separately. These electrodes are drawn and labeled in Fig. 5.7 (a). To control the $z$ component of the electric field there is a $+z$ and a $-z$ electrode. Setting the voltage on the two $z$ electrodes to the same magnitude with opposite polarities, such that their voltages sum to zero, creates an electric field in the $z$-direction. The electrodes controlling the $x$- and $y$-components of the electric field are coupled so that there can be a large opening on the $y$-axis, as well be explained below. Thus, on the $x$-axis there are two electrodes on each side: $+x+y$ and $+x-y$ on the $+x$ side and $-x+y$ and $-x-y$ on the $-x$ side. The electric field on the $x$-axis is controlled by setting the voltage of the $+x+y$ and $+x-y$ together, and the $-x+y$ and $-x-y$ together, to equal magnitudes with opposite polarities. To control the $y$-component of the electric field, the $+x+y$ and $-x+y$ are set to the same amount, and the $+x-y$ and $-x-y$, again with the pairs having opposite polarities from each other. To simultaneously control the $x$- and $y$-components of the electric field, the situation is slightly more complicated, because the electrodes are coupled. If the electric field in the $i$ direction is given by $E_i = \Delta V_i/d_i$, where $\Delta V_i$ is the difference in voltage on the electrodes on opposite sides of an axis $i$, and $d_i$ is a constant of order of the distance between the electrodes on that axis, then we must set the voltages on the electrodes as follows:

| | |
|---|---|
| $+z = \Delta V_z/2$ | $-z = -\Delta V_z/2$ |
| $+x+y = \Delta V_x/2 + \Delta V_y/2$ | $+x-y = \Delta V_x/2 - \Delta V_y/2$ |
| $-x+y = -\Delta V_x/2 + \Delta V_y/2$ | $-x-y = -\Delta V_x/2 - \Delta V_y/2$ |

The electrodes are made from 1/8 inch thick rectangular copper plates, 1-3 inches on a side. The copper plates are plated with a 20 $\mu$m layer of gold to prevent oxidation (which would create a surface with random patch potentials and defeat the purpose of the electrodes) and due to the superior electrical properties of gold. The $+z$ electrode has a square hole for the gold mirror of the mirror-MOT; the mirror surface, itself consisting of a thin layer of gold, is electrically shorted to the electrode. The electrodes are attached together using screws in kapton sheathes and alumina washers to electrically isolate them from each other; eight alumina rods connect the electrode package to the vacuum chamber. Additionally, the $+z$ electrode has a groove cut to fit the U-Z wire and is braced against it using a macor bracket, centering the entire electrode package in the chamber. The electrode and mirror are electrically isolated from the U-Z wire using a kapton sheet. Each electrode has a kapton-insulated wire connected to it; the wires are attached to a 9-pin connector on one of the vacuum chamber flanges. The electrodes have holes cut in them for beams to pass through: large holes for MOT beams (and the probe beam) and small holes for optical lattice beams. The fully assembled electrode package, inside the vacuum chamber, can be seen in Fig. 5.7 (b).

The control electrodes are riddled with holes for optical access. Although this undermines their efficacy slightly, the holes are mostly small compared to the overall size of the electrodes. More problematically, there are large gaps: the electrodes create a cube around the BEC but only cover four sides, leaving the sides on the $y$-axis completely open. This makes room for the cold atomic beam from the pyramidal MOT from the bottom, as well as for 480 nm light from the top. Because of this configuration, the electrodes might have difficulty effectively compensating for large stray fields. As mentioned above, these stray fields would come primarily from dielectrics in the vacuum chamber, especially windows. Thus, while we make concessions in our electric field compensation for optical access, we must also make

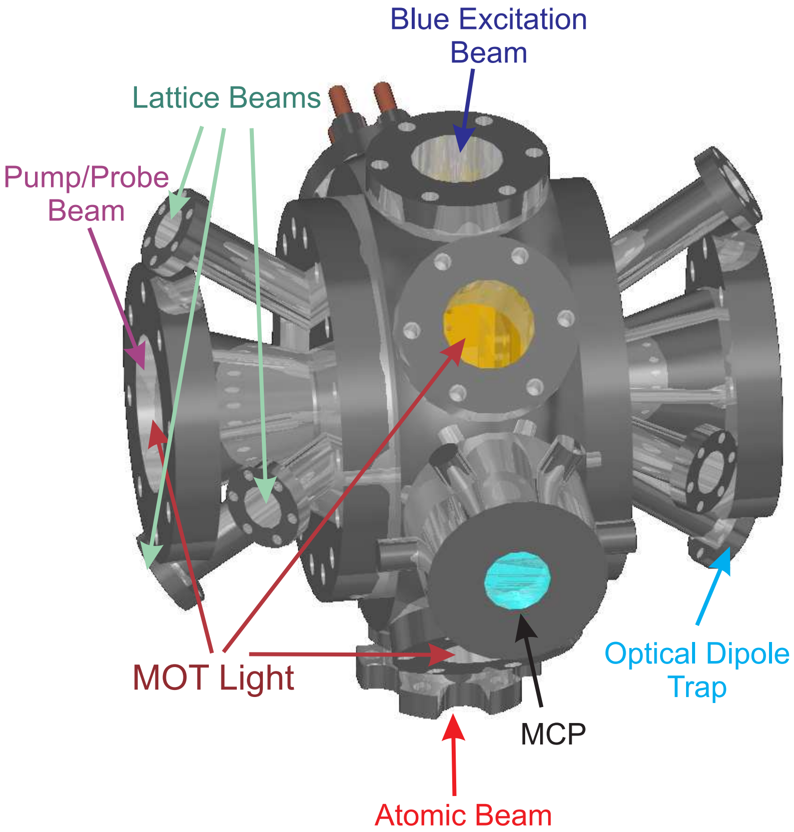

Figure 5.8: Optical access on the new chamber.

concessions in our optical access to shield against stray electric fields. To this end I designed new flanges for the vacuum chamber, shown in Fig. 5.8. In the old chamber, there were 4 inch windows as close to the BEC as possible to make it easy to get all of the MOT and probe beams into the chamber. In the new chamber we cannot have such a big window so close to the BEC (and thus the ion). Instead, we have 2.5 inch windows for the MOT and probe beams and 0.75 inch windows for lattice beams and an optical dipole trap, all shown in Fig. 5.8. The vacuum chamber walls themselves, being made of stainless steel and connected to electrical ground, pick up some of the slack from the electrodes in blocking stray fields. We use this to our advantage by having all of the windows as far out from the BEC region as possible, connected by steel tubes. These tubes help shield the central chamber from static charge on the windows. The largest, 2.5 inch, windows are connected by a conical tube ending in a 1.5 inch hole, to further shield against stray fields; since the tube is conical, the inner hole barely restricts optical access to the center of the chamber.

## 5.3 Ion Detection

Unlike neutral $^{87}$Rb atoms, $^{87}$Rb+ ions do not have a resonance at any wavelength for which we might easily acquire a laser. Thus, we cannot image them through fluorescence or shadow imaging. Instead, we use a microchannel plate (MCP) to detect the ions. The MCP consists of two plates and a phosphor screen. The front plate is held at $\sim -1$ kV. When an ion hits the front plate, it creates an avalanche of electrons. These electrons hit the back plate, held at $\sim +1$ kV, creating an even larger avalanche of electrons. This second avalanche hits a phosphor screen, held at $\sim +4$ kV, creating a blip on the screen as well as in the electrical signal coming off the screen. The high voltages ensure that the initial ion and the first set of electron avalanches have enough kinetic energy to create electron avalanches when they collide with the plates and to light up the phosphor screen when they reach it. The plates consist of an array of tubes; the electron avalanche does not spread transversely beyond the tube it starts in. This means that the position at which an ion hits the MCP is correlated with the position at which a blip appears on the phosphor screen, allowing spatial imaging of the ion distribution. The resolution of the imaging is theoretically limited by the size of the MCP tubes; the tube diameter is specified at 10 $\mu$m, but this is an overly optimistic estimate of the resolution of the entire system. In reality, the resolution at the phosphor screen is $\sim 50$ $\mu$m.

The BEC is $\sim 10$ $\mu$m across; an ion beyond that range is no longer interacting with the BEC. This is below the resolution limit of the MCP, so we must magnify the

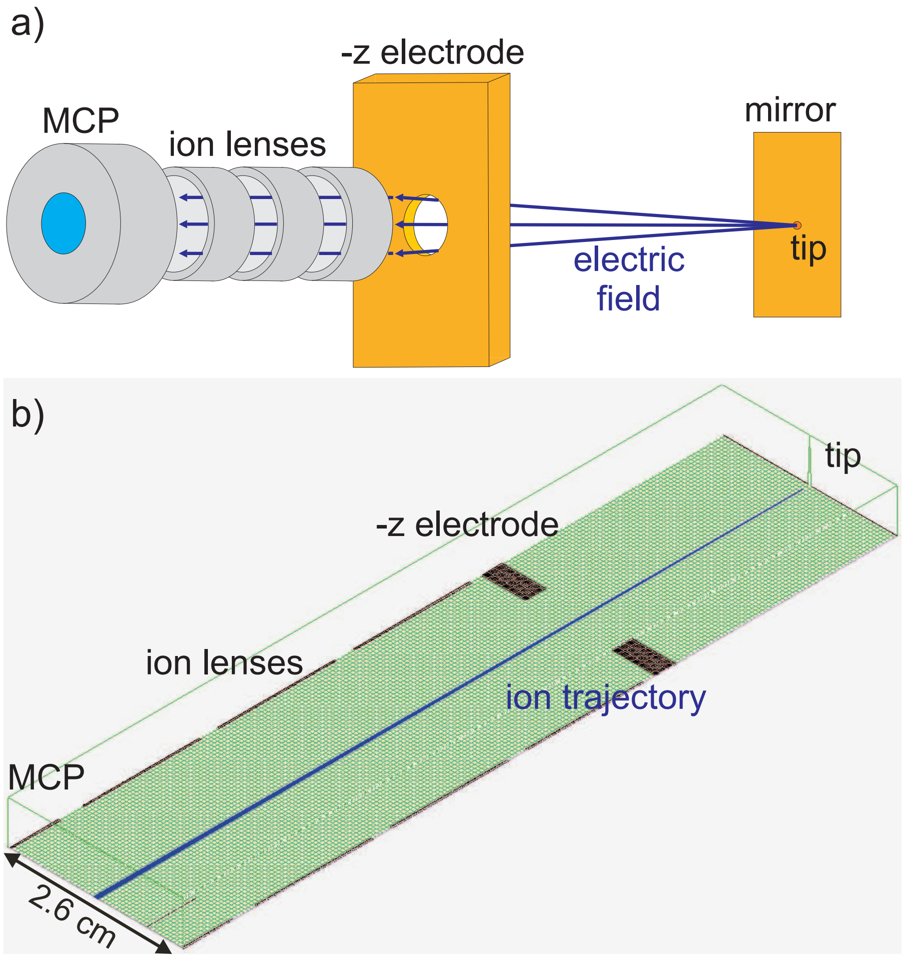

Figure 5.9: (a) Ion imaging setup: an ion-extraction tip at a positive voltage creates electric fields pointing radially outward. Ions follow the field lines, and the ion distribution is magnified on its way to the MCP. (b) A simulation, done in SIMION, of the magnification of the ion distribution in this setup.

ion distribution before it reaches the MCP. We do this by putting a positive voltage on a small electrode tip near the BEC. As depicted in Fig. 5.9 (a), this creates an electric field that points radially outward from the tip. An ion directly in front of the tip sees an electric field pointing directly in the $z$-direction toward the MCP; an ion slightly displaced from the center in $x$ or $y$ sees an electric field with a slight $x$ or $y$ component. The force due to this electric field causes the ion to follow the field lines. The result is that a spatial ion distribution in front of the ion-extraction tip is kept intact but is magnified as it travels toward the MCP. A simulation of this setup, done using the program SIMION, is shown in Fig. 5.9 (b). In this simulation, eleven ions are initially placed 3 mm from a 100 $\mu$m-diameter electrode patch. The ions are each spaced 2 $\mu$m apart, such that the initial distribution spans 20 $\mu$m. In the trajectory plot in Fig. 5.9 (b), this spacing is sufficiently small as to be unobservable. By the time the ions reach the plate at the end (representing the MCP), they are spaced macroscopically, with a visible width to their distribution in the figure; their distribution has been magnified by a factor of 35.

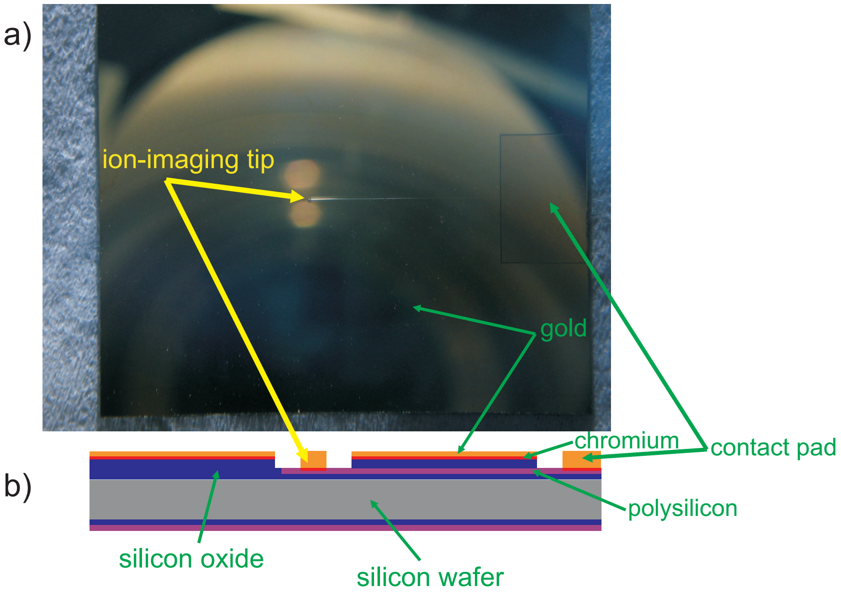

Figure 5.10: (a) Picture of the new mirror with electrode tip. (b) Cross section of the mirror.

The ion-extraction tip consists of an electrode patch on the mirror-MOT mirror, shown in Fig. 5.10. The tip is circular and is 100 $\mu$m in diameter. It is centered with respect to the U-Z wire. The mirror is not square, so the tip is not centered with respect to the mirror; the opening in the $+z$ electrode for the mirror is square, so the tip is centered with respect to that. The tip is connected to a contact pad on the edge of the mirror by a wire under the surface of the mirror; in this way, the surface of the mirror, electrically connected to the $+z$ electrode, shields the ions from the electric field of the wire, exposing the ions only to the electric field due to the tip. The contact pad is beyond the hole in the $+z$ electrode (not pictured in the figure), so the electrode itself shields the ions from the electric field due to the pad. The pad is connected to a wire by a beryllium-copper clip, sitting on top of a piece of kapton to isolate it from the $+z$ electrode. The tip and contact pad are each separated from the mirror by a 30 $\mu$m gulf; a layer of dielectric ($SiO_2$) separates the mirror surface from the wire underneath. It took me several months to fabricate the tip and mirror electrodes. For a detailed description of the fabrication of the mirror and tip, see Appendix B. In order for the ions to have a straight shot from the mirror to the MCP, the MCP must be placed at the far $-z$ end of the vacuum chamber. This necessitates rotating the vacuum chamber 90° from its orientation in Chapter II.

Figure 5.11: Ion lenses to control the ion path to the MCP.

There are two ways to adjust the magnification of the ion distribution. The first is to change the distance of the ions from the tip, since the magnification of the ion distribution is inversely proportional to the distance of the ions from the tip. This can be done by moving the Z-trap closer to the U-Z wire before photoionization. However, we are limited by the fact that the mirror is recessed into the $+z$ electrode by 1.3 mm; if we try to move the Z-trap closer to the mirror than the lip of the $+z$ electrode, we will not be able to reach it with our excitation lasers. The other option is a system of three ion lenses, shown in Fig. 5.11. The ion lenses consist of thin-walled aluminum tubes. These lenses are placed between the electrode package and the MCP, as depicted in Fig. 5.9 (a), with their axis aligned to the axis connecting the tip to the MCP. By varying the voltages on these three lenses, we should be able to enlarge or shrink the magnification of the ion distribution as it passes through them.

## 5.4 Conclusion

The upper portion of the BEC chamber has essentially been torn down and rebuilt from scratch. With these extensive modifications, we should be able to create larger BECs. More importantly, our system now supports the creation and imaging of unltracold ions. This is a major step toward experiments investigating the heretofore unexplored interactions between an ion and a BEC.

# CHAPTER VI

## Current Status and Future Directions

Although we have not yet reached the point where we can do experiments exploring the interactions between an ion and a BEC, we have made considerable progress toward that end. In this final chapter, I will describe the current state of the ion-BEC apparatus, and future experiments planned for this project.

### 6.1 Current Progress

#### 6.1.1 BEC

As of the writing of this thesis, we have not yet successfully created a BEC in the new chamber. In setting up the secondary MOT we encountered several setbacks. Ultimately, we replaced the pyramid, and removed the dividing tube. Since making these modifications, as mentioned in Chapter V, our new external MOT is larger than the one described in Chapter II. However, opening and closing the vacuum chamber always carries risks of ruining the vacuum. We most recently broke vacuum to remove the dividing tube; this required opening the upper chamber. Since all of the coils and optics for making a MOT have already been set up and attached to the chamber, we are reluctant to tear them all down and bake the chamber. In particular, we do not want to remove the coils. They are wound directly on the vacuum chamber, so removing them would mean cutting them down, and making new replacement coils. Instead, we are letting the chamber pump down slowly at room temperature. The vacuum pressure has been dropping slowly but steadily, and we expect that, even without the dividing tube or a bake-out, the chamber should reach the necessary level of vacuum, $< 5 \times 10^{-11}$ Torr.

Even without adequate vacuum pressures, we can make progress toward the BEC by optimizing all of the earlier steps. At this point, the external MOT is optimized, and loads into the U-MOT. We have also successfully found the optimal compensation magnetic fields for the optical molasses. We can transfer atoms from the optical molasses into the Z-trap. By including an optical pumping stage, we can markedly increase the number of atoms loaded into the Z-trap. Before we opened the chamber and removed the dividing tube, we saw a large fraction of the atoms loaded into the Z-trap remain trapped for 5 s. This means that the loading into the Z-trap is near-optimal. Finally, shadow imaging has been set up.

Two things remain to be done in order to make a BEC (other than wait for the vacuum pressure improve). The first is the optimization of the Z-trap. Although it is near-optimal now, in that many atoms that appear trapped after a short time remain trapped after a long time, there is still room for improvement. Our current transfer efficiency is $\sim 2\%$, which is considerably worse than the 10% transfer efficiency described in Chapter II. Furthermore, although many atoms remain trapped over several seconds, many atoms are lost within the first 1.5 s. Both the sub-optimal transfer efficiency and the trap losses are due to imperfect mode-matching between the Z-trap and the optical molasses. This needs to be improved before we can hope to create a BEC. The second thing that must be done to make a BEC is effective coupling of the rf for evaporative cooling into the chamber. Before we removed the dividing tube, we could not test the rf coupling because although we could load atoms from the secondary MOT into the Z-trap, we could not load very many atoms into the secondary MOT. Consequently, we had too few atoms in the Z-trap to easily observe the effects of an rf field. Now that the dividing tube is removed, the vacuum pressure is not yet low enough for atoms to remain in the Z-trap long enough to test the rf. However, we are optimistic that the vacuum pressure will soon reach a point where we can carry out these tests.

### 6.1.2 Ions

I have fully assembled the electrode package and ion lens system and rebuilt the vacuum chamber. We have successfully produced ions by shining a continuous blue 479 nm beam onto the U-MOT; the blue light combined with the 780 nm light of the MOT photoionizes atoms in the MOT through the two-photon transition $5S_{1/2} \rightarrow 5P_{3/2} \rightarrow$ continuum. By holding the tip at a constant potential of +12 V, we have extracted these ions from the U-MOT and detected them at the MCP. The signal on the MCP appears centered on a certain section of the phosphor screen; the location of that section depends on the exact alignment of the blue beam, indicating that we are already achieving some level of spatial imaging.

Before we can try to look at the interactions between an ion and a BEC, we must first minimize the electric field. This can be done by tuning the blue beam to a Rydberg transition rather than to the continuum. Rydberg atoms are very sensitive to electric fields. By simultaneously scanning the blue laser and changing the electric field on one axis in the vicinity of the Rydberg atoms, we can map the Stark spectrum of the Rydberg level. The turning point on the Stark spectrum is the point of minimum electric field magnitude. By iteratively finding the minimum electric field on each axis, we should be able to cancel stray electric fields. To increase the sensitivity of our electric field zeroing, we can map the Stark spectra of increasingly higher Rydberg levels. We have not yet started to zero the electric fields in our setup. However, other experiments in the lab have used this method previously to minimize stray electric fields, and we can draw upon their expertise.

## 6.2 Future Experiments

The theoretical literature on ion-BEC interactions is vast. However, no controlled experiments exploring these interactions have been published. This means that there are many years worth of experiments waiting to be done with our new apparatus. They can mostly be divided into two categories: experiments involving single (or a small number of) ions, and experiments involving many ions.

### 6.2.1 Single-Ion Experiments

Once we have a BEC and have minimized the electric field, the first phenomenon we will look for is self-trapping of an ion in the BEC. The electric field from an ion should polarize the BEC atoms; with the electrons attracted to the ion and the nuclei repelled by it, the ion should be surrounded by a small negative charge distribution. If the ion reaches the edge of the BEC, there will be a negative charge distribution on its side facing the BEC, but a neutral charge distribution (due to lack of atoms) on its side facing away from the BEC. This would result in a force pulling the ion toward the BEC. This system has not been sufficiently theoretically characterized to predict whether or not this force would be sufficient to prevent the ion from exiting the BEC. However, several theorists have addressed the topic of uncharged impurities in a BEC, predicting both trapping [41–44, 75] and expulsion [76], as well as crystalization of multiple impurities [75]

While the above experiment would examine the effect of the BEC on the ion, we could also look at the effect of the ion on the BEC. The ion might affect the density distribution of the BEC sufficiently that a particularly dense or dilute region of the BEC in the vicinity of the ion would be visible through shadow imaging [39].

Another planned experiment is to look for the ionic molecules described in Ref. [40]. In this case, the polarization potential due to the ion, combined with the density of the BEC, should attract neutral BEC atoms to the ion. Three-body recombination would occur between two neutral atoms and the ion, and one neutral atom would be expelled from the BEC while the second neutral atom would be bound to the ion in the highest bound state. The orbit of an ion in this bound state is sufficiently large that many atoms can simultaneously occupy the highest bound state without significant risk of collision. Côté *et al.* predict a recombination rate of a few hundred per second, so if we can achieve ion dwell times of over 100 $\mu$s (or, better yet, if we observe self-trapping of the ion) we should be able to see these molecules form on an observable fraction of the ions we produce.

In our new apparatus, we have included windows to allow for an optical lattice. This would allow us to study the effects of a charged impurity on BEC in an optical lattice [45, 46]. In particular, our ion imaging setup would allow us to observe clustering of ions in a BEC in an optical lattice [77].

Another possible future experiment involving single ions would be to excite ions in only a small region of the BEC, and use the spatial imaging capabilities of our apparatus to characterize charge hopping [78, 79]. We could also excite ions over only a small region, tuning the laser as close to the photoionization threshold as possible, and see if this leads to blockading of the excitation other ions nearby due to Coulomb energy shifts or the Pauli exclusion principle [38].

### 6.2.2 Many-Ion Experiments

If we increase the intensity of the blue laser, we can photoionize the entire BEC at once. Ultra-cold plasmas are typically formed by photoionizing a MOT; photoionizing a BEC would result in a plasma four or five orders of magnitude colder than the coldest ultra-cold plasmas ever created. Additionally, a BEC is typically at least three orders of magnitude more dense than a MOT. This means that an ultra-cold plasma made from a BEC has at least 12 orders of magnitude higher phase-space density than an ultra-cold plasma made from a MOT. This huge increase in phase space density could potentially lead to observations of new physics.

Incidentally, the ion-imaging system described in Chapter V could be used to image anything that can be ionized. If the entire BEC is photoionized and then sent to the MCP, we should be able to obtain sub-micron images of the BEC in position space. In this case, it would be important to immediately send the ions to the MCP so that they do not have time to repel each other and distort the resultant image. One way to do this might be to use a fairly weak, long duration photoionizing pulse, so that the ions are ejected from the BEC before ions next to them can be created. Since it only takes a few microseconds for the ions to traverse the entire distance to the MCP, the time scales for this long-duration pulse can still be quite short compared to the time scales of interactions within the BEC, such that the resultant image can still be considered a ”snapshot” not blurred over time. Typically, BECs undergo TOF before imaging, and so are imaged in momentum space rather than position space. However, some phenomena, such as solitons or localization due to an optical lattice, can only be indirectly observed in momentum space. With position-space imaging we would be able to observe these phenomena directly. Optical imaging systems are limited by the wavelength of the probe light, or, more practically, by the size of their lenses and camera apertures; optical imaging systems capable of sub-micron imaging are rare. The best existing imaging system consists of a scanning electron microscope near a BEC; it can achieve 150 nm resolution, but takes $\sim$100 ms to scan an entire BEC [80, 81], so any temporal variation of the system will be averaged over in the imaging process. Although we will probably not be able to surpass the electron microscope's 150 nm resolution, our imaging time will be on the order of microseconds, which should allow us to observe small transient phenomena such as vortices and solitons. This would be a major advancement in atom cloud imaging.

## 6.3 Conclusion

While the new ion-BEC apparatus is not yet fully operational, we are making progress toward the creation of both a BEC and an environment suitable to manipulate ultracold ions. Once we are ready to photoionize atoms in a BEC, a huge array of new experiments will be open to us in the entirely unexplored realm of ion-BEC interactions.

# APPENDICES

# APPENDIX A

## Funny Shapes in the Z-trap

The Z-trap, described in detail in Chapter II, appears as five different potentials to the five magnetic sublevels of the $F = 2$ state. By using a variety of rf fields to couple these magnetic sublevels, we can create a variety of potential shapes.

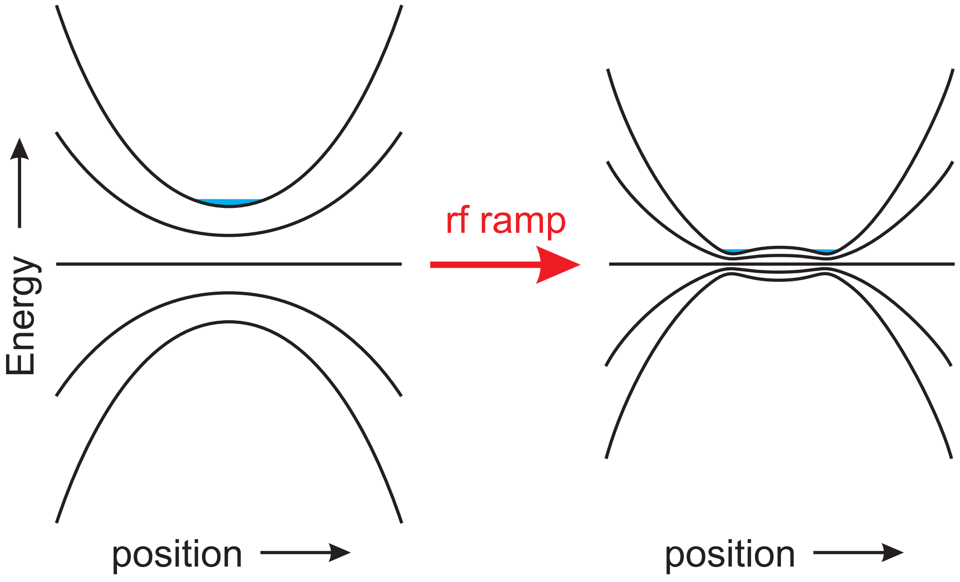

Figure A.1: Energy levels in a harmonic potential before and after an rf ramp.

We start with forced evaporative cooling, as described in Chapter II; however, we do not cool all the way to the BEC transition, because we would have too few atoms left to see anything. Then, as normal, we decompress the Z-trap. At this point we have several times $10^5$ atoms at temperatures of $\sim 1$ $\mu$K. The bottom of the Z-trap in the uncompressed state is at ~2.5 MHz. We start an rf ramp well below this value and ramp up to ~3.5 MHz over 100 ms (fast compared to the evaporative cooling ramp). The effect of this rf ramp on the potential is shown in Fig. A.1; the rf-free potentials of the harmonic Z-trap are shown on the left side of the figure and the dressed-state potentials at the end of the rf ramp are shown on the right. Atoms initially in the $m_F = 2$ low magnetic field seeking state see a bump form in the center of the trap which grows as the rf frequency increases.

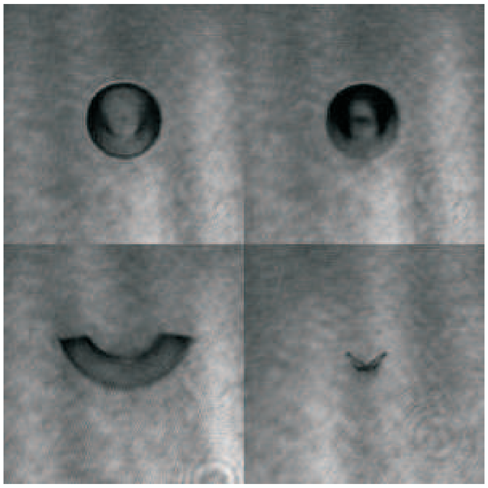

Figure A.2: Cyclops, Frowny Face, Upside-down Rainbow, Butterfly

The process is sufficiently diabatic that $m_F = 2$ atoms are mostly not coupled out of the trap. Instead, they are pushed aside by the potential bump in the center of the trap. Thus, at the end of the rf ramp, the atoms are in a shell-shaped potential. However, this is not a gentle process, and the atoms end up sloshing around in the shell potential. Examples of this sloshing motion are shown in Fig. A.2. As can be seen, the sloshing motion of the atoms can follow a variety of paths, creating many different patterns. The conditions leading to the four pictures in Fig. A.2 differ in the amplitude of the rf, the slope of the rf ramp, and the final frequency at the end of the ramp; small variations, even shot-to-shot noise, lead to drastic differences in the resulting pattern.

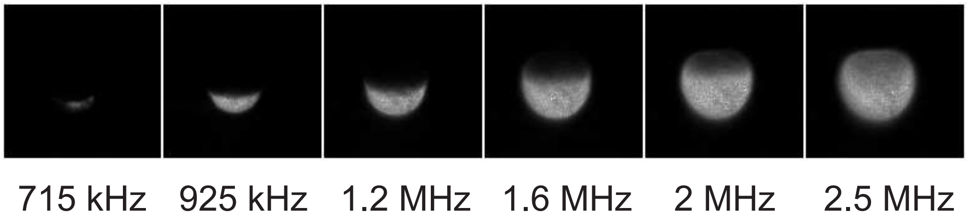

Figure A.3: A shell potential filled to different heights depending on the temperature of the atom cloud. The final frequency of the evaporative cooling ramp is indicated under the shadow image for each atom cloud.

If, after creating the shell potential, we sustain the rf at its final frequency and allow the atom cloud time to equilibrate we find that it falls due to gravity. The atom cloud, having been evaporatively cooled, has too high a phase-space density to effectively fill the large shell potential. The result is that the potential is preferentially filled from the bottom (with respect to gravity). This can be seen in Fig. A.3, where the overall shape of the atom cloud is clearly that of a shell, in that its 2-D projection in the shadow image appears denser on the edges and more dilute in the middle. However, the atom clouds on the left of the figure only form a partial shell, tending toward the direction of gravity. In Fig. A.3, different temperature atom clouds are shown filling different fractions of the shell potential. We vary the temperature by changing the final frequency of the evaporative cooling ramp; the final evaporative cooling frequency for each atom cloud is indicated under its respective image. Hotter atom clouds contain atoms with higher kinetic energies which can reach higher regions of the shell potential. The filling height cannot be used as a direct measure of temperature, however, because the atom clouds with higher final evaporative cooling frequencies, in addition to being hotter, also have more atoms, which could artificially cause them to appear to fill more of the shell potential.

# APPENDIX B

## Fabricating the Tip and Mirror Electrode

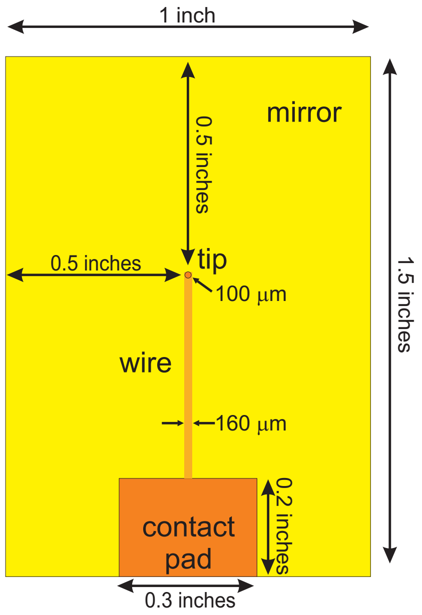

Figure B.1: Mirror with ion-extraction tip.

The mirror with the ion extraction tip electrode, described in Chapter V is a silicon chip that I fabricated over the course of several months in the Lurie Nanofabrication Facility at the University of Michigan. The chip is 1 inch × 1.5 inches. The electrode tip is centered 0.5 inches from each side, except for the side with the connector pad; the center of the tip is 1 inches from the side with the connector pad. The tip is 100 $\mu$m in diameter, and is a 16-sided regular polygon (the corners of a 16-sided polygon should be sufficiently obtuse to not create edge sharp edge effects when an electric potential is applied). It is separated from the mirror surface by a gap 30 $\mu$m wide. The tip is connected to the connector pad with a polysilicon (polySi) wire, 160 $\mu$m wide and and 1 $\mu$m thick, and with a resistance of 1.6 k$\Omega$; the wire is separated from the mirror surface by a 3.5 $\mu$m layer of $SiO_2$. The resistance between the mirror surface and the tip is $> 2$ M$\Omega$ based on measurements (this is the maximum reading on the multimeter used to measure the resistance). In theory, the resistance is 2 T$\Omega$ between the tip and mirror and 800 G$\Omega$ between the tip and silicon wafer, but there may be flaws. The tip should be able to withstand a voltage of at least 150 V before the insulation breaks down.

The process for making the chip starting from standard 4-inch wafers is as follows:

1) Deposit a layer of $SiO_2$ on the wafer, 1.5 $\mu$m thick, to insulate the chip from the semiconducting base wafer, using low-pressure chemical vapor deposition.

2) Deposit a layer of polySi, 1 $\mu$m thick.

3) Dope the polySi with phosphorous to increase the conductivity. Strip the passive layer of phosphorous that forms on top using buffered hydrofluoric acid (BHF).

4) Spin photoresist onto the wafer. Line up the mask and expose to UV, and then develop the resist. Etch the polySi into the shape of the contact pad, wire, and tip using a plasma etch.

5) Deposit a layer of $SiO_2$, 3.5 $\mu$m thick, to insulate the wire from the mirror surface.

6) Photoresist, mask, develop. Etch away all of the $SiO_2$ directly covering the tip and contact pad, using BHF.

7) Evaporate a seed layer of chromium, and a layer of gold 300 nm thick for the mirror.

8) Photoresist, mask, develop. Plate the tip and connector pad with 2 $\mu$m of gold.

9) Photoresist, mask, develop. Etch the gold layer around the tip and the contact pad, forming a 30 $\mu$m gap between them and the mirror. Etch the seed layer of chromium in the gap.

10) Dice the wafer along the edges of the useful region of the chip.

# BIBLIOGRAPHY

# BIBLIOGRAPHY

[1] G. Gabrielse, X. Fei, L. A. Orozco, R. L. Tjoelker, J. Haas, H. Kalinowsky, T. A. Trainor, and W. Kells. Thousandfold improvement in the measured antiproton mass. *Phys. Rev. Lett.*, 65 (11):1317, September 1990.

[2] Daniel Adam Steck. Rubidium 87 d line data. May 2008. URL `http://steck.us/alkalidata`.

[3] M.H. Anderson, J.R. Ensher, M.R. Matthews, C.E. Wieman, and E.A. Cornell. Observation of bose-einstein condensation in a dilute atomic vapor. *Science*, 269:198, July 1995.

[4] K.B. Davis, M.-O. Mewes, M.R. Andrews, N.J. van Druten, D.S. Durfee, D.M. Kurn, and W. Ketterle. Bose-einstein condensation in a gas of sodium atoms. *Phys. Rev. Lett.*, 75(22): 3969, November 1995.

[5] Harold J. Metcalf and Peter van der Straten. *Laser Cooling and Trapping.* Springer, 1999.

[6] James R. Anglin and Wolfgang Ketterle. Bose-einstein condensation of atomic gases. *Nature*, 416:211, March 2002.

[7] Vanderlei Bagnato, David E. Prtichard, and Daniel Kleppner. Bose-einstein condensation in an external potential. *Phys. Rev. A*, 35(10):4354, May 1987.

[8] Anthony J. Leggett. Bose-einstein condensation in the alkali gases: Some fundamental concepts. *Rev. Mod. Phys.*, 73(2):307, April 2001.

[9] E. P. Gross. Structure of quantized vortex. *I1 Nuovo Cimento*, 20(3):454, May 1961.

[10] L. P. Pitaevskii. Vortex lines in an imperfect bose gas. *I1 Nuovo Cimento*, 13(2):451, 1961.

[11] O. Morsch and M. Oberthaler. Dynamics of bose-einstein condensates in optical lattices. *Rev. Mod. Phys.*, 78(1):179, January 2006.

[12] M. Kozuma, L. Deng, E. W. Hagley, J. Wen, R. Lutwak, K. Helmerson, S. L. Rolston, and W. D. Phillips. Coherent splitting of bose-einstein condensed atoms with optically induced bragg diffraction. *Phys. Rev. Lett.*, 82(5):871, February 1986.

[13] Jakob Reichel, Yvan Castin, Maxime Ben Dahan, Ekkehard Peik, and Christophe Salomon. Bloch oscillations of atoms in an optical potential. *Phys. Rev. Lett.*, 76(24):4508, June 1996.

[14] O. Morsch, J.H. Muller, M. Cristiani, D. Ciampini, and E. Arimondo. Bloch oscillations and mean-field effects of bose-einstein condensates in 1d optical lattices. *Phys. Rev. Lett.*, 87: 140402, September 2001.

[15] Yu. B. Ovchinnikov, J. H. Müller, M. R. Doery, E. J. D. Vredenbregt, K. Helmerson, S. L. Rolston, and W. D. Phillips. Diffraction of a released bose-einstein condensate by a pulsed standing light wave. *Phys. Rev. Lett.*, 83(2):284, July 1999.

[16] Arthur Bramley. The index of refraction and dielectric constant of water vapor. *Journal of the Franklin Institute*, 203(5):701, May 1927.

[17] E. J. Post. Sagnac effect. *Rev. Mod. Phys.*, 39(2):475, April 1967.

[18] B. Culshaw. The optical fibre sagnac interferometer: an overview of its principles and applications. *Measurement Science and Technology*, 17(1):R1, January 2006.

[19] Leo Stodolsky. Matter and light wave interferometry in gravitational fields. *General Relativity and Gravitation*, 11(6).

[20] B. Abbott, R. Abbott, R. Adhikari, and *et al.* Mean-field effects may mimic number squeezing in bose-einstein condensates in optical lattices. 76(8):082003, October 2007.

[21] John D. Perreault and Alexander D. Cronin. Observation of atom wave phase shifts induced by van der waals atom-surface interactions. *Phys. Rev. Lett.*, 95:133201, September 2005.

[22] Christopher R. Ekstrom, Jörg Schmiedmayer, Michael S. Chapman, Troy D. Hammond, and David E. Pritchard. Measurement of the electric polarizability of sodium with an atom interferometer. *Phys. Rev. A*, 51(5):3883, May 1995.

[23] A. Miffre, M. Jacquey, M. Büchner, G. Trénec, and J. Viguét. Measurement of the electric polarizability of lithium by atom interferometry. *Phys. Rev. A*, 73:011603(R), January 2006.

[24] Asimina Arvanitaki, Savas Dimopoulos, Andrew A. Geraci, Jason Hogan, and Mark Kasevich. How to test atom and neutron neutrality with atom interferometry. *Phys. Rev. Lett.*, 100: 120407, March 2008.

[25] A. Gangat, P. Pradhan, G. Pati, and M. S. Shahriar. Two-dimensional nanolithography using atom interferometry. *Phys. Rev. A*, 71(4):043606, April 2005.

[26] M. Greiner, O. Mandel, T. Esslinger, T. W. Hänsch, and I. Bloch. Quantum phase transition from a superfluid to a mott insulator in a gas of ultracold atoms. *Nature*, 415:39, January 2002.

[27] Gretchen K. Campbell, Jongchul Mun, Micah Boyd, Patrick Medley, Aaron E. Leanhardt, Luis G. Marcassa, David E. Pritchard, and Wolfgang Ketterle. Imaging the mott insulator shells by using atomic clock shifts. *Science*, 313:649, August 2006.

[28] K. Góral, L. Santos, and M. Lewenstein. Quantum phases of dipolar bosons in optical lattices. *Phys. Rev. Lett.*, 88(17):170406, April 2002.

[29] S. Ospelkaus, C. Ospelkaus, O. Wille, M. Succo, P.Ernst, K. Sengstock, and K. Bongs. Localization of bosonic atoms by fermionic impurities in a three-dimensional optical lattice. *Phys. Rev. Lett.*, 96:180403, May 2006.

[30] Tim Rom, Thorsten Best, Olaf Mandel, Artur Widera, Markus Greiner, Theodor W. Hänsch, and Immanuel Bloch. State selective production of molecules in optical lattices. *Phys. Rev. Lett.*, 93(7):073002, August 2004.

[31] D. Jaksch, V. Venturi, J. L. Cirac, C. J. Williams, and P. Zoller. Creation of a molecular condensate by dynamically melting a mott insulator. *Phys. Rev. Lett.*, 89(4):040402, July 2002.

[32] M. G. Moore and H. R. Sadeghpour. Controlling two-species mott-insulator phases in an optical lattice to form an array of dipolar molecules. *Phys. Rev. A*, 67:041603(R), April 2003.

[33] D. Jaksch. Optical lattices, ultracold atoms and quantum information processing. *Contemporary Physics*, 45(5):367, September 2004.

[34] K. Xu, Y. Liu, J. R. Abo-Shaeer, T. Mukaiyama, J. K. Chin, D. E. Miller, W. Ketterle, Kevin M. Jones, and Eite Tiesinga. Sodium bose-einstein condensates in an optical lattice. *Phys. Rev. A*, 72:043604, October 2005.

[35] I. B. Spielman, W.D. Phillips, and J.V. Porto. Mott-insulator transition in a two-dimensional atomic bose gas. *Phys. Rev. Lett.*, 98:080404, February 2007.

[36] M. Köhl, H. Moritz, T. Stöferle, C. Schori, and T. Esslinger. Superfluid to mott insulator transition in one, two, and three dimensions. *J. Low Temp. Phys.*, 138(3,4):635, February 2005.

[37] T. Stöferle, H. Moritz, C. Schori, M. Köhl, and T. Esslinger. Transition from a strongly interacting 1d superfluid to a mott insulator. *Phys. Rev. Lett.*, 92(13):130403, April 2004.

[38] I. E. Mazets. Photoionization of neutral atoms in a boseeinstein condensate. *Quantum Semiclass. Opt.*, 10:675, June 1998.

[39] P. Massignan, C. J. Pethick, and H. Smith. Static properties of positive ions in atomic bose-einstein condensates. *Phys. Rev. A*, 71(2):023606, February 2005.

[40] R. Côté, V. Kharchenko, and M. D. Lukin. Mesoscopic molecular ions in bose-einstein condensates. *Phys. Rev. Lett.*, 89(9):093001, August 2002.

[41] R. M. Kalas and D. Blume. Interaction-induced localization of an impurity in a trapped bose-einstein condensate. *Phys. Rev. A*, 73(4):043608, April 2006.

[42] Krzysztof Sacha and Eddy Timmermans. Atom interferometry using kapitza-dirac scattering in a magnetic trap. *Phys. Rev. A*, 73:063604, June 2006.

[43] M. Bruderer, W. Bao, and D. Jaksch. Self-trapping of impurities in bose-einstein condensates: Strong attractive and repulsive coupling. *Europhys. Lett.*, 82(3):30004, 2008.

[44] F. M. Cucchietti and E. Timmermans. Strong-coupling polarons in dilute gas bose-einstein condensates. *Phys. Rev. Lett.*, 96(21):210401, June 2006.

[45] Hao Fu and A. G. Rojo. Tonks-girardeau gas in an optical lattice: Effects of a local potential. *Phys. Rev. A*, 74(1):013620, July 2006.

[46] Valeriy A. Brazhnyi, Vladimir V. Konotop, and Víctor M. Pérez-García. Defect modes of a bose-einstein condensate in an optical lattice with a localized impurity. *Phys. Rev. A*, 74(2): 023614, August 2006.

[47] D. Ciampini, M. Anderlini, J. H. Müller, F. Fuso, O. Morsch, J. W. Thomsen, and E. Arimondo. Photoionization of ultracold and bose-einstein-condensed rb atoms. *Phys. Rev. A*, 66 (4):043409, October 2002.

[48] T. W. Hänsch, I. S. Shahin, and A. L. Schawlow. High-resolution saturation spectroscopy of the sodium d lines with a pulsed tunable dye laser. *Phys. Rev. Lett.*, 27(11):707, September 1971.

[49] R. A. Nyman, G. Varoquaux, B. Villier, D. Sacchet, F. Moron, Y. Le Coq, A. Aspect, and P. Bouyer. Tapered-amplified antireflection-coated laser diodes for potassium and rubidium atomic-physics experiments. *Rev. Sci. Inst.*, 77:033105, March 2006.

[50] R. S. Williamson III, P. A. Voytas, R. T. Newell, and T. Walker. A magneto-optical trap loaded from a pyramidal funnel. *Opt. Exp.*, 3(3):111, August 1998.

[51] A. Kasper, S. Schneider, Ch. vom Hagen, M. Bartenstein, B. Engeser, T. Schumm, I. Bar-Joseph, R. Folman, L. Feenstra, and J. Schmiedmayer and. A boseeinstein condensate in a microtrap. *J. Opt. B*, 5:S143, April 2003.

[52] S. Schneider, A. Kasper, Ch. vom Hagen, M. Bartenstein, B. Engeser, T. Schumm, I. Bar-Joseph, R. Folman, L. Feenstra, and J. Schmiedmayer. Bose-einstein condensation in a simple microtrap. *Phys. Rev. A*, 67:023612, February 2003.

[53] Maxime Ben Dahan, Ekkehard Peik, Jakob Reichel, Yvan Castin, and Christophe Salomon. Bloch oscillations of atoms in an optical potential. *Phys. Rev. Lett.*, 76(24):4508, June 1996.

[54] M. Gustavsson, E. Haller, M. J. Mark, J. G. Danzl, G. Rojas-Kopeinig, and H.-C. Nägerl. Control of interaction-induced dephasing of bloch oscillations. *Phys. Rev. Lett.*, 100:080404, February 2008.

[55] M. Fattori, C. DErrico, G. Roati, M. Zaccanti, M. Jona-Lasinio, M. Modugno, M. Inguscio, , and G. Modugno. Atom interferometry with aweakly interacting bose-einstein condensate. *Phys. Rev. Lett.*, 100:080405, February 2008.

[56] R. Zhang, R. E. Sapiro, R. R. Mhaskar, and G. Raithel. Role of the mean field in bloch oscillations of a bose-einstein condensate in an optical lattice and harmonic trap. *Phys. Rev. A*, 78:053607, November 2008.

[57] L. S. Bartell, R. R. Roskos, and H. Bradford Thompson. Reflection of electrons by standing light waves: Experimental study. *Physical Review*, 166(5):1494, February 1968.

[58] Phillip L. Gould, George A. Ruff, and David. E. Pritchard. Diffraction of atoms by light: The near-resonant kapitza-dirac effect. *Phys. Rev. Lett.*, 56(8):827, February 1986.

[59] G. Behinaein, V. Ramareddy, P. Ahmadi, and G. S. Summy. Exploring the phase space of the quantum $\delta$-kicked accelerator. *Phys. Rev. Lett.*, 97:244101, December 2006.

[60] D. E. Miller, J.R. Anglin, J. R. Abo-Shaeer, K. Xu, J. K. Chin, and W. Ketterle. High-contrast interference in a thermal cloud of atoms. *Phys. Rev. A*, 71:043615, April 2005.

[61] O. Garcia, B. Deissler, K. J. Hughes, J. M. Reeves, and C. A. Sackett. Bose-einstein-condensate interferometer with macroscopic arm separation. *Phys. Rev. A*, 74(3):031601(R), September 2006.

[62] G.-B. Jo, Y. Shin, S. Will, T. A. Pasquini, M. Saba, W. Ketterle, D. E. Pritchard, M. Vengalattore, and M. Prentiss. Long phase coherence time and number squeezing of two bose-einstein condensates on an atom chip. *Phys. Rev. Lett.*, 98(3):030407, January 2007.

[63] Ying-Ju Wang, Dana Z. Anderson, Victor M. Bright, Eric A. Cornell, Quentin Diot, Tetsuo Kishimoto, Mara Prentiss, R. A. Saravanan, Stephen R. Segal, and Saijun Wu. Atom michelson interferometer on a chip using a bose-einstein condensate. *Phys. Rev. Lett.*, 94:090405, March 2005.

[64] Ernst M. Rasel, Markus K. Oberthaler, Herman Batelaan, Jörg Schmiedmayer, and Anton Zeilinger. Atom wave interferometry with diffraction gratings of light. *Phys. Rev. Lett.*, 75 (14):2633, October 1995.

[65] R. Zhang, R. E. Sapiro, N. V. Morrow, R. R. Mhaskar, and G. Raithel. Bose-einstein condensate inside a bragg-reflecting atom cavity. *Phys. Rev. A*, 77:063615, June 2008.

[66] R. E. Sapiro, R. Zhang, and G. Raithel. Atom interferometry using kapitza-dirac scattering in a magnetic trap. *Phys. Rev. A*, 79:043630, April 2009.

[67] R. E. Sapiro, R. Zhang, and G. Raithel. Reversible loss of superfluidity of a bose-einstein condensate in a 1d optical lattice. *New Journal of Physics*, 11:013013, January 2009.

[68] Jinbin Li, Yue Yu, Artem M. Dudarev, and Qian Niu. Interaction broadening of wannier functions and mott transitions in atomic bec. *New Journal of Physics*, 8:154, August 2006.

[69] D. van Oosten, P. van der Straten, and H.T.C. Stoof. Mott insulators in an optical lattice with high filling factors. *Phys. Rev. A*, 67:033606, March 2003.

[70] Roberto B. Diener, Qi Zhou, Hui Zhai, and Tin-Lun Ho. Criterion for bosonic superfluidity in an optical lattice. *Phys. Rev. Lett.*, 98:180404, May 2007.

[71] T. Gericke, F. Gerbier, A. Widera, S. Fölling, O. Mandel, and I. Bloch. Adiabatic loading of a bose-einstein condensate in a 3d optical lattice. *J. Mod. Opt.*, 54(5):735, March 2007.

[72] Zoran Hadzibabic, Sabine Stock, Baptiste Battelier, Vincent Bretin, and Jean Dalibard. Interference of an array of independent bose-einstein condensates. *Phys. Rev. Lett.*, 93(18):180403, October 2004.

[73] C. Orzel, A. K. Tuchman, M. L. Fenselau, M. Yasuda, and M. A. Kasevich. Squeezed states in a bose-einstein condensate. *Science*, 291:2386, March 2001.

[74] S. B. McKagan, P. L. Feder, and W. P. Reinhardt. Mean-field effects may mimic number squeezing in bose-einstein condensates in optical lattices. *Phys. Rev. A*, 74:013612, July 2006.

[75] David C. Roberts and Sergio Rica. Impurity crystal in a bose-einstein condensate. *Phys. Rev. Lett.*, 102(2):025301, January 2009.

[76] Siu A. Chin and Harald A. Forbert. Quantum expulsion of impurities from a boseeinstein condensate. *Phys. Lett. A*, 272:402, August 2000.

[77] Alexander Klein, Martin Bruderer, Stephen R Clark, and Dieter Jaksch. Dynamics, dephasing and clustering of impurity atoms in boseeinstein condensates. *New Journal of Physics*, 9:411, November 2007.

[78] Robin Côté. From classical mobility to hopping conductivity: Charge hopping in an ultracold gas. *Phys. Rev. Lett.*, 85(25):5316, December 2000.

[79] R. Côté and A. Dalgarno. Ultracold atom-ion collisions. *Phys. Rev. Lett.*, 62(1):012709, June 2000.

[80] Tatjana Gericke, Peter Würtz, Daniel Reitz, Tim Langen, and Herwig Ott. High-resolution scanning electron microscopy of an ultracold quantum gas. *Nature Physics*, 4:949, December 2008.

[81] Peter Würtz, Tim Langen, Tatjana Gericke, Andreas Koglbauer, and Herwig Ott. Experimental demonstration of single-site addressability in a two-dimensional optical lattice. *Phys. Rev. Lett.*, 103:080404, August 2009.